



Universiteit
Leiden
The Netherlands

Star-forming galaxies at the Cosmic Dawn

Smit, R.

Citation

Smit, R. (2015, April 28). *Star-forming galaxies at the Cosmic Dawn*. *PhD Thesis*. Retrieved from <https://hdl.handle.net/1887/32843>

Version: Not Applicable (or Unknown)

License: [Leiden University Non-exclusive license](#)

Downloaded from: <https://hdl.handle.net/1887/32843>

Note: To cite this publication please use the final published version (if applicable).

Cover Page



Universiteit Leiden



The handle <http://hdl.handle.net/1887/32843> holds various files of this Leiden University dissertation

Author: Smit, Renske

Title: Star-forming galaxies at the cosmic dawn = Stervormende sterrenstelsels tijdens het kosmische ochtendgloren

Issue Date: 2015-04-28

Star-Forming Galaxies at the Cosmic Dawn

Renske Smit

Cover: River Lek Sunrise, *credit: Sara Winter*, and MACS J0416.1-2403, *credit: NASA, ESA, and M. Postman (STScI), and the CLASH team.*

ISBN: 978-94-6108-9632

Star-Forming Galaxies at the Cosmic Dawn

Stervormende sterrenstelsels tijdens het kosmische ochtendgloren

Proefschrift

ter verkrijging van
de graad van Doctor aan de Universiteit Leiden,
op gezag van Rector Magnificus prof. mr. C.J.J.M. Stolker,
volgens besluit van het College voor Promoties
te verdedigen op dinsdag 28 April 2015
klokke 16:15 uur

door

Renske Smit
geboren te Los Angeles
in 1985

Promotiecommissie

Promotor: Prof. dr. Marijn Franx

Co-Promotor: Dr. Rychard Bouwens

Overige leden: Prof. dr. Daniel Schaerer (Université de Geneve)

Prof. dr. Huub Röttgering

Prof. dr. Joop Schaye

dr. Jarle Brinchman

dr. Ivo Labbé

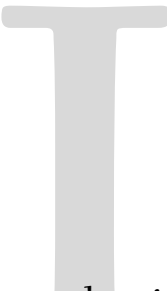
*Hoe kón ik dat niet eerder weten,
niet beter zien in vroeger tijd?
Hoe moet ik het weer ooit vergeten?
– M. Vasalis¹*

¹**Tijd** uit Parken en Woestijnen

Contents

1	Introduction	11
1.1	Early galaxy formation	12
1.2	Observational challenges	13
1.3	Recent results on high-redshift galaxies	15
1.3.1	UV luminosity functions and the cosmic star formation rate density	16
1.3.2	Stellar masses and specific star formation rates	18
1.4	Thesis summary	20
2	The Star Formation Rate Function for Redshift $z \sim 4 - 7$ Galaxies	23
2.1	Introduction	24
2.2	SFR functions	24
2.2.1	Dust-corrected luminosity functions	25
2.2.2	Analytical SFR functions	27
2.3	Results	29
2.3.1	High-SFR end: linear build-up of $\log \text{SFR}^*$ from $z \sim 8$ to $z \sim 2$	29
2.3.2	Low-SFR end: flatter slopes and large uncertainties	31
2.4	Summary	31
3	High-EW Nebular Emission in $z \sim 7$ Galaxies	39
3.1	Introduction	40
3.2	Observations	41
3.2.1	Data	41
3.2.2	Photometry and Selection	42
3.2.3	IRAC Photometry	43
3.3	Results	44
3.3.1	[3.6]–[4.5] color distribution and nebular emission lines	44
3.3.2	Inferred [OIII]+H β EWs of $z \sim 7$ galaxies from the mean SED	46
3.3.3	Specific star formation rates	48
3.4	Summary and discussion	51
4	High-precision Photometric Redshifts from Spitzer/IRAC	55
4.1	Introduction	56
4.2	Observations, photometry and $z \sim 5 - 8$ sample	57
4.2.1	<i>HST</i> data and photometry	57
4.2.2	<i>Spitzer</i> /IRAC data and photometry	58
4.2.3	Base sample of $z \sim 5 - 8$ galaxies	59
4.3	[3.6]–[4.5] color vs. redshift	60
4.4	Ultra-blue [3.6]–[4.5] galaxies	61
4.4.1	Blue [3.6]–[4.5] sources at $z \sim 6.8$	63
4.4.2	Blue [3.6]–[4.5] sources at $z \sim 6.0$	65
4.5	A fiducial sample of $z \sim 6.8$ emission line galaxies	67
4.5.1	Selection of our fiducial $z \sim 6.8$ sample	67

4.5.2	Ascertaining the mean redshift and contamination fraction of the $z \sim 6.8$ sample	68
4.5.3	Quantifying the rest-frame EWs of [OIII]+H β in our $z \sim 6.8$ IRAC ultra-blue sample	70
4.6	Summary and discussion	71
5	On the Systematic Use of Hα to Measure Star Formation Rates	77
5.1	Introduction	78
5.2	Data and Samples	79
5.2.1	Spectroscopic sample	79
5.2.2	Photometric sample	81
5.3	Derived properties of $z = 3.8 - 5.0$ galaxies	82
5.3.1	SED fitting	82
5.3.2	H α + [NII] equivalent widths and line strengths	82
5.3.3	Composite SEDs	83
5.4	Inferred H α as star formation rate indicator	84
5.4.1	Star formation rate indicators	84
5.4.2	Origin of high H α star formation rates	85
5.5	SFR-mass sequence	89
5.6	Star formation rate functions	90
5.7	Summary	91
	Nederlandse samenvatting	97
	Curriculum Vitae	103
	Nawoord	105



Introduction

The question of how the first stars formed and assembled into galaxies lies at the frontier of modern astrophysics. The study of these first sources of cosmic illumination was transformed by the installation of new instrumentation aboard the *Hubble Space Telescope* during one of the final *Space Shuttle* missions in 2009. *Hubble* has since unveiled a population of ultra-faint galaxies seen just a few hundred million years after the Big Bang, an epoch often termed the *Cosmic Dawn*. This thesis presents pioneering observational studies of the first generations of galaxies, enabling an examination of their properties and the physics that governed the illumination of the early cosmos.

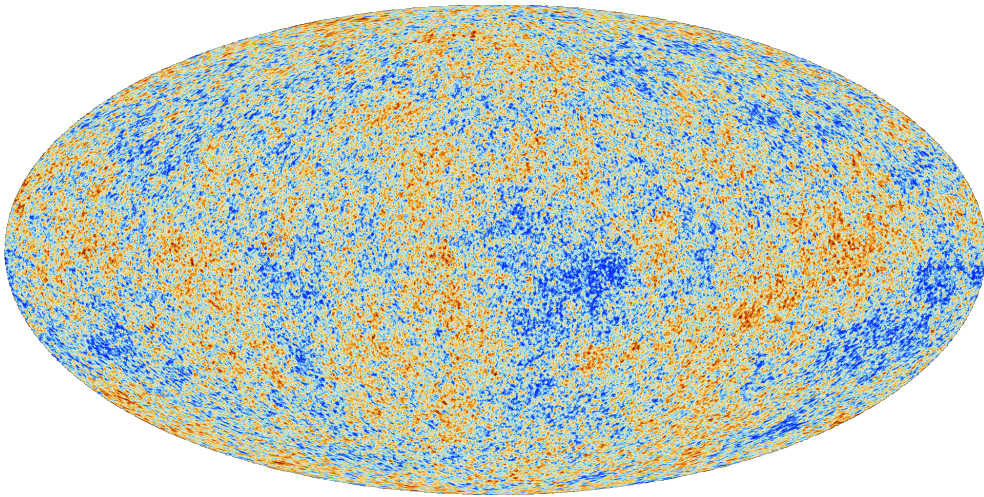


Figure 1.1: The anisotropies of the CMB as observed by Planck. The CMB is a snapshot of the oldest light in our Universe, imprinted on the sky when the Universe was just 380 000 years old. It shows tiny temperature fluctuations that correspond to regions of slightly different densities, representing the seeds of all future structure: the stars and galaxies of today. *Credit: ESA and the Planck Collaboration*

1.1 Early galaxy formation

In the current concordance model of cosmology, known as Λ cold dark matter (Λ CDM), our observable Universe was formed in the Big Bang roughly 13.8 billion years ago. Within the Λ CDM parametrization the energy density of the Universe consists of $\sim 27\%$ collisionless cold dark matter particles, $\sim 69\%$ dark energy (Riess et al., 1998; Perlmutter et al., 1999) and only $\sim 4\%$ baryonic matter, the material that comprises all forms of matter we observe around us such as atoms, molecules, gas, rocks, stars, planets and lifeforms (Planck Collaboration et al., 2014).

In the first 4 hundred thousand years after the Big Bang the Universe expands and cools down from nearly infinite temperatures to just a few thousand degrees Kelvin, which enables the formation of neutral hydrogen and the cosmic microwave background (CMB) radiation, the first observable light of the Universe (Penzias & Wilson, 1965). The small anisotropies in the temperature of the CMB (see Figure 1.1) indicate density perturbations in the distribution of baryonic and cold dark matter in the primordial Universe (Smoot et al., 1992). In the time period between 4 hundred thousand to 400 million years after the Big Bang, often called the *Dark Ages*, these perturbations in the density distribution grow under the influence of gravity and eventually form dense clumps of both dark matter (*dark matter halos*) and baryonic matter that comprise the birth places of the first stars and galaxies.

From measurements of the Thomson scattering optical depth in the CMB (Planck Collaboration et al., 2015) we know that roughly 400 million years after the Big Bang, the first galaxies in the Universe produce enough radiation to start re-ionizing the neutral hydrogen gas surrounding galaxies. This era of reionization is completed roughly 1 billion years (Gyr) after the Big Bang, as measured from the Gunn-Peterson trough (Gunn & Peterson, 1965) in early Quasar spectra

(Becker et al., 2001; Fan et al., 2006). These measurements constrain the total ionizing photon budget produced by the first galaxies over a time period of only 600 million years.

Detailed mapping of the star formation density of the universe as a function of cosmic time (Madau et al., 1998) indicates that the peak era of star forming activity in the history of the Universe occurred between 8 to 10 billion years ago, just a few billion years after the Big Bang. In this era we observe a large variety of galaxy types: from massive dead elliptical galaxies (Cimatti et al., 2004; Kriek et al., 2006) to large rotating star-forming disks (Genzel et al., 2006) to highly star-bursting dust-obscured galaxies (Rowan-Robinson et al., 1991). The discovery of these strongly evolved systems are evidence for a remarkable rapid evolution of the first generations of galaxies in the 2 billion years after the era of reionization.

These collected constraints motivate observational studies of galaxies in the first few billion years of cosmic time. Though the technological challenges are significant, we aim to observe the light of galaxies more than ten billion light years away in order to find the answers to questions such as; how were the very first stars formed? how do the earliest galaxies produce enough radiation to ionize the bulk of the hydrogen gas in the universe? and how do the first generations of galaxies evolve to form the diverse and advanced Universe we observe during the peak of cosmic history?

1.2 Observational challenges

Observational studies of the cosmic history of the Universe are possible due to the fact that light travels at a large but finite speed. When we observe a galaxy at large cosmological distances, we inevitably look back in time to the moment the light was emitted from the galaxy. To study galaxies during the first few billion years after the Big Bang, we need to identify the extremely faint light emitted by galaxies more than 10 billion light years away. The large scale detection of distant galaxies was enabled by the rapid progress in charge-coupled-device (CCD) technology and the emergence of a new class of 8-10 meter telescopes and space observatories in the 1980s and 1990s. In particular, the launch of the *Hubble Space Telescope (HST)* in 1990 and the subsequent servicing missions to the telescope in 1993, 1997, 2002 and 2009 have been a driving force for scientific progress in the study of the early Universe.

While the enormous distances needed to observe nascent galaxies provide a considerable challenge for scientific studies, further difficulties arise from the continuous expansion of the Universe (Hubble, 1926). This causes light emitted by distant sources to be observed at longer wavelengths, a phenomenon called *redshift* (indicated with the symbol z). The more distant a galaxy, and therefore the further we look back in time, the redder the light observed at our telescopes. For example, galaxies within the era of reionization have a typical redshift of $z \sim 7$ or greater, indicating that we observe the wavelength of their light at least 8 times longer than it was originally radiated from the source. As a result, essential information contained in the light spectrum of distant galaxies can shift out of the observable wavelength range of our most sensitive telescopes.

The measured flux density as a function wavelength, or the spectral energy distribution (SED), of a galaxy is used to measure the number of massive, newly-formed stars (0.1-0.4 μm), the number of low-mass, long-lived stars (0.4-5 μm) and the properties of the interstellar dust-particles that absorb and reradiate the stellar light (5-10³ μm). Figure 1.2 shows the SED of a young galaxy placed at different distances from the observer. The top panel indicates the light observed from a

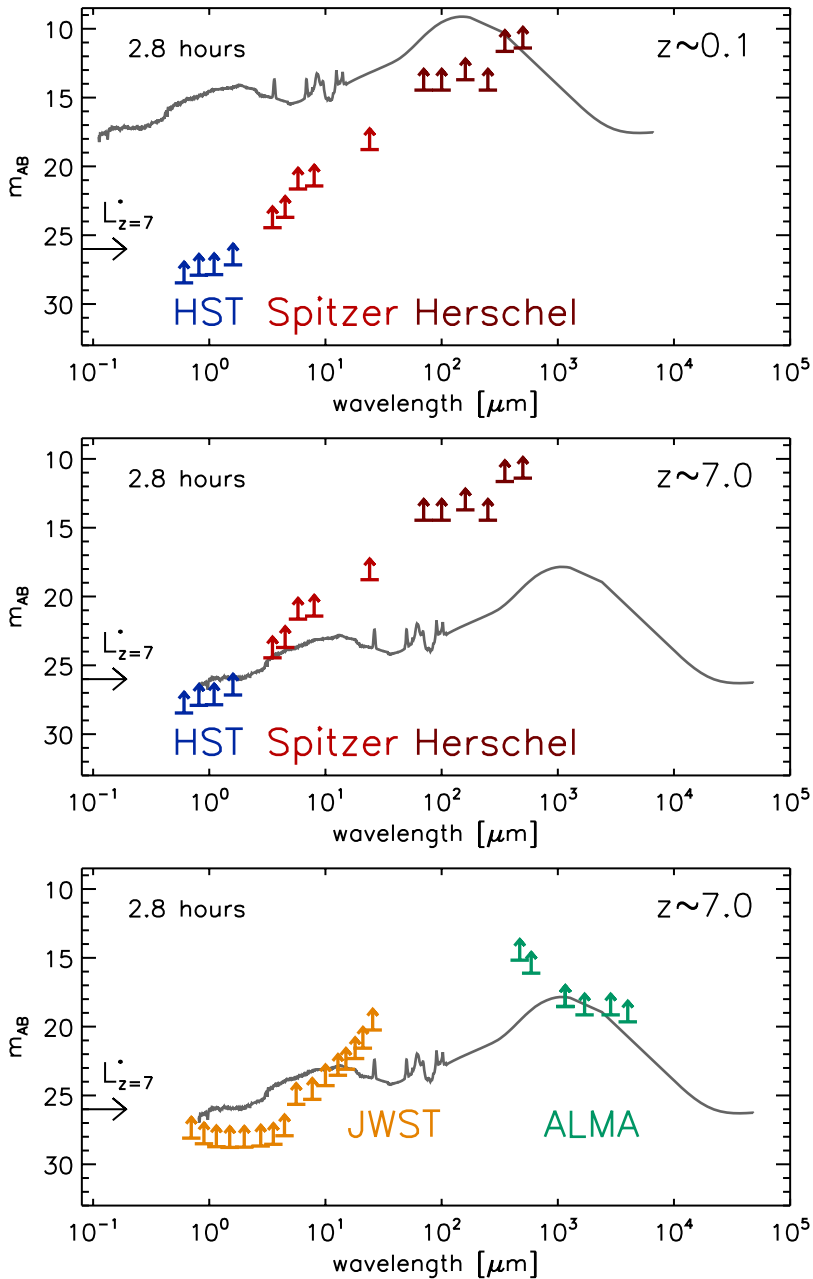


Figure 1.2: The SED (grey lines) of a young galaxy observed locally (*top panel*) and at redshift $z \sim 7$ (*middle and bottom panel*). Upward arrows indicate the limiting magnitude of a 2.8 hour broadband observation with HST (blue arrows), the Spitzer Space Telescope (red arrows), the Herschel Space Observatory (brown arrows), JWST (yellow arrows) and ALMA (green arrows). While current state of the art observatories such as HST, Spitzer and Herschel are capable of observing local galaxies over a wide range in wavelength (*top panel*), the faint, redshifted light from redshift $z \sim 7$ galaxies is particularly challenging to observe (*middle panel*). Future facilities such as JWST and ALMA will open up a new window onto the properties of the earliest stars and galaxies (*bottom panel*).

galaxy in the local Universe, while the middle and bottom panels show the light observed from a galaxy at redshift $z \sim 7$, roughly 800 million years after the Big Bang. The upward arrows in the top and middle panel indicate the sensitivity of current state of the art space observatories in different photometric bands across the spectrum for a typical ~ 3 hour observation. While local galaxies can easily be observed over a wide range in wavelength (top panel of Figure 1.2), the lower observed brightness and redder observed wavelengths of redshift $z \sim 7$ galaxies only allow for easy detections in a few of the reddest *HST* bands (middle panel of Figure 1.2).

In addition to the challenge of detecting galaxies in many photometric broadbands, the possibilities for obtaining information on atomic lines in galaxy spectra is very limited at high redshifts. Not only can atomic absorption and emission lines be used for the determination of the exact redshift of galaxies, and therefore the precise measurement of the distance and look-back time, recombination lines at $>0.4 \mu\text{m}$ can provide important information on the heavy elements in galaxies and the instantaneous star formation rate (SFR) of galaxies. Current state of the art spectroscopic observations, performed by 8-10 meter ground-based telescopes, reach out to $2.2 \mu\text{m}$, which only allows for the detection of the most common recombination lines out to redshift $z \sim 3 - 5$.

Despite the current limitations on observations of high-redshift galaxies, the study of the early Universe continues to be a growing scientific field due to impressive progress in telescope and detector technology. The bottom panel of Figure 1.2 indicates the sensitivities of two future facilities; the *James Webb Space Telescope (JWST)* will be launched in 2018, while the *Atacama Large Millimeter Array (ALMA)* will reach full capacity in 2015. These new telescopes will not only allow for revolutionary sensitive broadband photometry, but will also provide the first constraints on the spectra and emission lines of high-redshift galaxies. As these facilities illustrate, future studies of high-redshift galaxies will continue to expand our knowledge of the early Universe and the processes underpinning the formation of the first stars and galaxies.

1.3 Recent results on high-redshift galaxies

The identification of large samples of high-redshift galaxies in astronomical images took off in the 1990s with the development and widespread use of the Lyman-break technique (e.g. Steidel et al., 1996). This selection technique is based on a well-known sharp feature in the spectrum of star-forming galaxies, due to the absorption of $\lesssim 0.1 \mu\text{m}$ photons by hydrogen atoms within interstellar and intergalactic gas clouds. This feature can be identified in broadband photometry by a sudden drop in flux in the bluest bands, as illustrated in Figure 1.3. Using the reddest available wavelength band to initially detect candidate high-redshift galaxies, we look for sources that are undetected in the bluer wavelength bands. The wavelength where the galaxy drops out provides us with a modestly accurate estimate of the redshift of the galaxy light. This simple yet powerful selection technique can be exploited to obtain statistically significant samples of galaxies at different epochs of cosmic time. The development of this technique and the availability of increasingly sensitive detectors in the optical and near-infrared wavelengths, such as the Wide Fields Camera 3 (WFC3) that was installed on *HST* in 2009, has resulted in large photometric surveys that identify consecutive generations of Lyman-break galaxies in the first few billion years after the Big Bang.

In order to detect these faint Lyman-break galaxies, surveys are typically designed to either

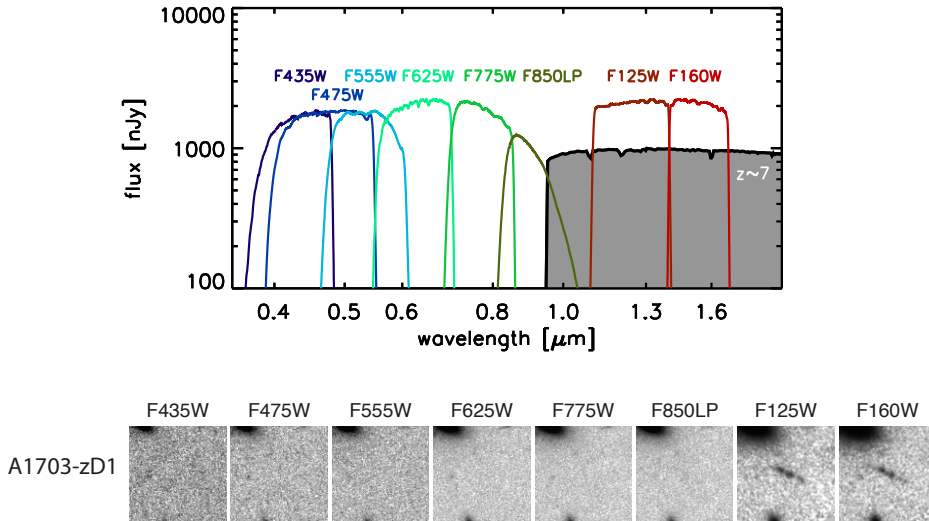


Figure 1.3: Broadband photometry of a Lyman-break galaxy at redshift $z \sim 7$ behind the massive galaxy cluster Abell 1703 by Bradley et al. (2012). *Top:* Schematic overview of the response curves from 8 *HST* broadband filters with the typical SED of a redshift $z \sim 7$ galaxy. The sharp Lyman-break feature at $\sim 0.1 \mu\text{m}$ is redshifted into near-infrared. *Bottom:* Postage stamp images from left to right show broadband observations at wavelengths of $\sim 0.4, 0.5, 0.55, 0.6, 0.8, 0.9, 1.3$ and $1.6 \mu\text{m}$. The sharp drop in flux between the ~ 0.9 and $1.3 \mu\text{m}$ band images is used to place the lookback time of this galaxy at an epoch just 800 million years after the Big Bang.

focus on blank or lensed fields. Blank fields are selected as regions of the sky with no bright foreground stars or galaxies, which are ideal for long integration times to bring down the background noise. Lensed fields, on the other hand, are centered on rare, massive clusters of galaxies. Due to the deflection of light by mass these clusters act as cosmic lenses, magnifying the images of the distant galaxies behind them. Advantages of lensed fields include the shorter integration times needed to detect distant galaxies and the improved resolution on the magnified galaxy images, while important disadvantages include the limited number of suitable cluster fields available and the uncertainty in the magnification factor derived from the modeled mass structure of the foreground galaxy clusters. Though the last decade has primarily seen an investment of telescope time towards blank field surveys, the recent discovery of the most distant galaxy known (Coe et al., 2013) in the Cluster Lensing And Supernova survey with Hubble (CLASH, see Figure 1.4) and the allocation of 840 *HST* orbits in 2013 to the Frontier Fields cluster program signify the increasing importance of lensing surveys for high redshift studies.

1.3.1 UV luminosity functions and the cosmic star formation rate density

The Lyman-break technique described in the last section predominantly selects galaxies with bright ultraviolet (UV) radiation ($\lesssim 0.4 \mu\text{m}$), redshifted towards the observed optical and infrared wavelength range. Consequently one of the most important diagnostics of early galaxy formation is the UV luminosity function (LF), or the number density of galaxies as a function of their total radiated UV luminosity at a fixed redshift, shown in Figure 1.5. The UV LF shows

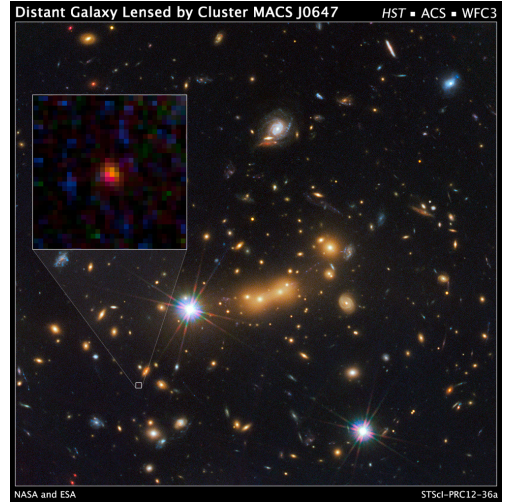


Figure 1.4: Image of what is widely considered the most distant galaxy observed to date by Coe et al. (2013). This extremely distant galaxy is observed 420 million years after the Big Bang (redshift $z \sim 11$) and was discovered behind the massive galaxy cluster MACS0647 in the CLASH survey. Credit: NASA, ESA, and M. Postman and D. Coe (STScI) and CLASH Team

a characteristic shape of a power-law slope for faint galaxies (high UV magnitudes) and an exponential cut-off for bright galaxies (low UV magnitudes). The turn-over point in the UV LF changes rapidly with redshift, quantifying the evolution of the galaxy population as a function of time.

The UV luminosity measured from high-redshift galaxies, is dominated by the light from O and B stars. These stars are among the shortest-lived stars in the Universe and have a typical lifetime of ~ 100 million years. The measured light from O and B stars therefore gives a reasonable estimate of the star formation rate in a galaxy, assuming the galaxy has experienced a smooth star formation history over the last ~ 100 Myr. The integrated UV LF is thus often used as a proxy for the global star formation rate density of the Universe at any given redshift, as indicated by the blue points in Figure 1.6.

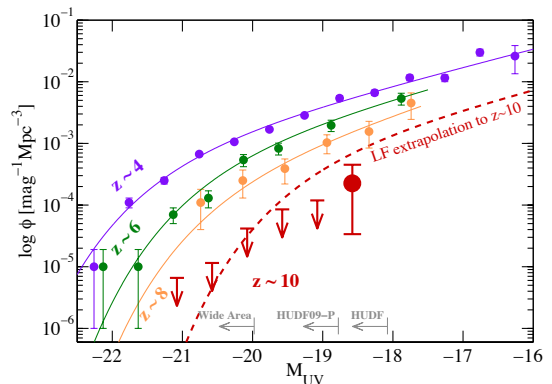


Figure 1.5: The UV luminosity function of redshift $z \sim 4, 6, 8$ and 10 galaxies by Oesch et al. (2012). Solid points indicate the number density of galaxies as a function of their UV magnitude (M_{UV}), with bright galaxies at low magnitudes (left) and faint galaxies at the highest magnitudes (right). The evolution of the UV LF as a function of decreasing redshift indicates more luminous galaxies are formed during later epochs after the Big Bang.

Perhaps the most important uncertainty in measuring the star formation rate from the observed UV light is the unknown fraction of the flux that is absorbed by dust particles in interstellar clouds. Cosmic dust consists of small particles of solid material ranging from a few molecules to

~ 0.1 mm in size and is particularly efficient in absorbing stellar radiation at the bluest wavelengths and reradiating this light in the mid- and far-infrared wavelength range ($5\text{-}10^3 \mu\text{m}$).

Section 1.2 describes the limitations of even the most sensitive space observatories operating in the far-infrared wavelength range to observe the light from distant Lyman-break galaxies (see also Figure 1.2), which results in a lack of direct dust measurements at any redshift above $z \sim 2$. However, using the reddening effect of dust particles on the color of a galaxy due to the preferential absorption of blue light we can make an estimate of the amount of dust in a galaxy and consequently the total extinguished UV light.

Bouwens et al. (2012) measured the intrinsic UV colors of 2500 galaxies between $z \sim 4 - 7$ and subsequently derived the dust-corrected global star formation rate density in the early Universe indicated with the red points in Figure 1.6. The shape of the global SFR density with its rise from redshift $z \sim 10$ to $z \sim 2$ and decline from redshift $z \sim 1$ to $z \sim 0$ constitutes an important observational test bed that any model or simulation must match, if it is to capture the physical processes that govern galaxy formation and evolution.

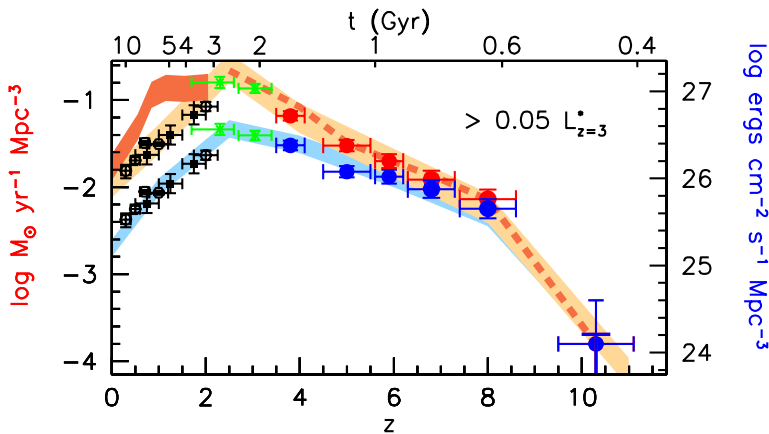


Figure 1.6: The global star formation rate density of the Universe over the last 13 billion years of cosmic history by Bouwens et al. (2012). Blue points are obtained by integrating the measured UV LF at different redshifts and converting this to an estimate of the global SFR, while no correction is taken into account for the absorbed light by cosmic dust in galaxies. Red points indicate dust-corrected measurements based on the UV colors of high-redshift galaxies.

1.3.2 Stellar masses and specific star formation rates

The previous section describes the usefulness of accurate knowledge of the UV properties of high-redshift galaxies for determining the global SFR density of the Universe. However, these measurements provide only one particular constraint on theories and models of early galaxy formation. Another important parameter in galaxy formation studies is the total mass in stars within a galaxy or the *stellar mass*. The measurement of stellar mass is useful since it provides us with an integrated measure of the total number of stars formed over the history of a galaxy. The stellar masses of star-forming galaxies are correlated with their SFRs through the so-called *main-sequence* of star-forming galaxies, dictating that galaxies with larger stellar masses on average have higher SFRs. This fundamental relation follows a power-law-like shape with a slope close to unity and

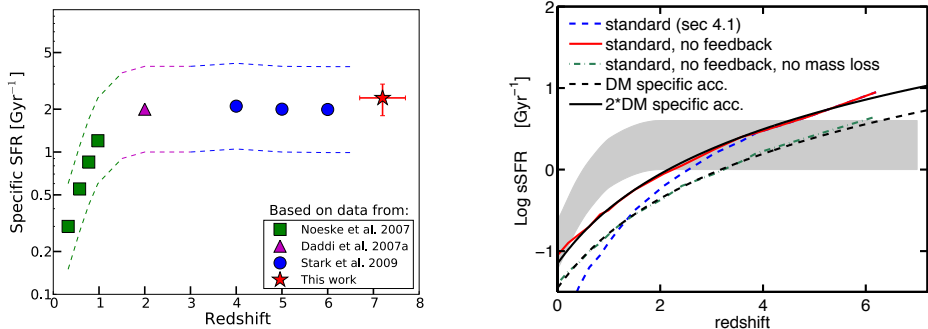


Figure 1.7: The average sSFR (SFR/stellar mass) of galaxies with a stellar mass of $5 \cdot 10^9 M_{\odot}$ as a function of redshift as observed by González et al. (2010, *left panel*) and derived from various models of galaxy formation by Weinmann et al. (2011, *right panel*). The discrepancy in the evolution of the sSFR between theory and observations either indicates a systematic bias in the observed properties of galaxies or an incomplete understanding of the physical mechanisms driving early galaxy formation.

remarkably small scatter (0.3 dex) out to redshift $z \sim 2$ (e.g. Wuyts et al., 2011). However, the normalization of this relation changes significantly over the same redshift range, indicating a rapid change in the efficiency of star formation. Star-formation efficiency is often measured in the context of the *specific* star formation rate (sSFR), defined as the SFR divided by the total stellar mass of a galaxy.

Figure 1.7 shows the observed evolution of the average sSFR of galaxies with a stellar mass of $5 \cdot 10^9 M_{\odot}$ as a function of redshift by González et al. (2010). González et al. (2010) found a non-evolution of the sSFR between $z \sim 2$ and $z \sim 7$ in contrast to the steep rise of the sSFR from redshift $z \sim 0$ to $z \sim 2$. The rate at which a galaxy forms new stars strongly depends on the supply of fresh gas from the intergalactic medium. In a Λ CDM Universe where dark matter is many times more abundant than baryonic matter the infall of fresh gas onto a galaxy scales with the infall rate of dark matter onto the dark matter halo surrounding the galaxy. Consequently, any model or simulation of galaxy formation predicts a sSFR that closely follows the evolution of the specific accretion rate of dark matter, a well-determined quantity that follows a smooth rise with redshift over the history of the Universe (see the solid black line on the right panel of Figure 1.7). The comparison on the right panel of Figure 1.7 clearly shows a strong discrepancy between our theoretical understanding of star formation efficiency over cosmic time and the results found by González et al. (2010) and other observational studies before 2010.

Possible explanations for the discrepancy in the sSFR between observations and simulations in Figure 1.7 include an incomplete understanding of the impact of supernovae on the interstellar medium within simulations of galaxy formation, but also a potential systematic bias in the measured properties of very high-redshift galaxies that is unaccounted for in the derivation of the sSFR. Measurements of the stellar masses of high-redshift galaxies are particularly challenging, since they require an estimate of the number of low-mass, long-lived stars within a galaxy, whose light has redshifted out of the observable wavelength range of *HST* into the regime of *Spitzer* (see Figure 1.2). Schaerer & de Barros (2009) first noted the potential influence of strong emission lines originating from oxygen and hydrogen atoms in the nebular gas around galaxies on the ob-

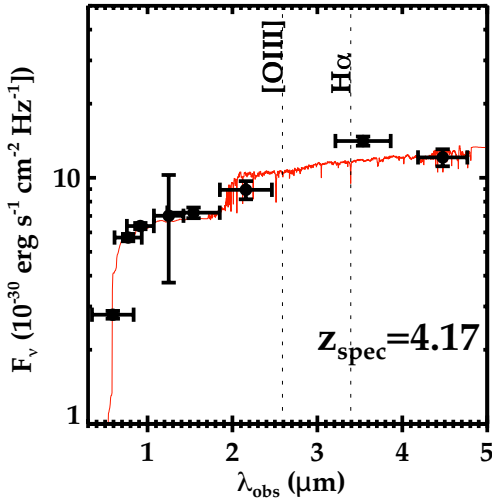


Figure 1.8: Example of the broadband photometry (*black points*) of a galaxy at redshift $z = 4.17$ by Stark et al. (2013). The red line indicates the estimated stellar contribution to the SED of this galaxy. The *Spitzer* flux measurement at $4.5 \mu\text{m}$ is free of line contamination from the nebular gas surrounding stars, while the $3.6 \mu\text{m}$ flux measurement is contaminated by the nebular hydrogen line $\text{H}\alpha$. Taking advantage of galaxies with nebular line contamination in only one *Spitzer* broadband, allows for an measurement of the emission line strength from the offset in the contaminated band with respect to the expected stellar flux.

served flux from *Spitzer*. These emission lines cannot be directly measured through spectroscopy (see §1.2) and therefore we face a degeneracy in the interpretation of the observed *Spitzer* light of high-redshift galaxies. We either measure radiation from numerous low-mass, long-lived stars, indicating a large stellar mass, or we measure the flux from strong nebular lines, a typical signature of galaxies that are undergoing a short and intense burst of star formation. While the sSFRs in Figure 1.7 are derived assuming the former interpretation, the latter interpretation would result in lower stellar masses and therefore higher sSFRs at redshifts $z \gtrsim 4$.

The first studies that attempted to measure the strength of nebular emission lines in high-redshift galaxies were focussed on redshift $z \sim 4$. Using the clean measurement of the stellar continuum light provided by the *Spitzer* $4.5 \mu\text{m}$ broadband flux at $z \sim 4$, Shim et al. (2011) and Stark et al. (2013) showed a significant offset in the $3.6 \mu\text{m}$ band flux, suggesting that the spectra of high-redshift galaxies selected with the Lyman-break technique contain strong emission line features in the $3.6 \mu\text{m}$ band (see the example in Figure 1.8). In order to establish whether this mechanism can systematically change the sSFRs over the redshift range $z \sim 4 - 7$, similar studies at higher redshifts are required. At redshifts $z > 4$ however the contamination of the *Spitzer* bands by emission lines increases, while the observed brightness from galaxies decreases due to the longer lookback times, inhibiting the robust determination of the influence of nebular lines on the derived sSFRs out to the highest redshifts.

1.4 Thesis summary

This thesis presents studies on the properties of galaxies over the redshift range $z \sim 4 - 7$. Chapters 2 and 5 discuss the SFR properties of high-redshift galaxies, how well we can determine SFRs for large samples of galaxies and what we can learn about the star formation histories of these galaxies. Chapters 3 and 4 focus on emission line properties of redshift $z \sim 7$ galaxies, how they influence the estimates of stellar mass and sSFR at the highest redshifts and how we can use our knowledge of strong emission lines to significantly improve the redshift determinations of these galaxies.

Chapter 2 presents the first derivation of the SFR function over the redshift range $z \sim 4 - 7$. Capitalizing on the technique developed by Bouwens et al. (2012) to correct UV light for dust using the measurements of the UV colors of large samples of Lyman-break galaxies, we correct the UV LF at redshift $z \sim 4 - 7$ for dust. Our stepwise determinations of the number density of galaxies as a function of their SFR provides an important constraint that models and simulations of galaxy formation must attempt to match. We derive flatter faint-end slopes, when compared to the UV LF over the same redshift range, which is important to estimate the total number of star-forming galaxies during the era of reionization. Furthermore, we compare our SFR functions at $z \sim 4 - 7$ with other SFR indicators at lower redshift. Importantly, we find a uniform build-up of the abundance of star-forming galaxies over the first 3 billion years of cosmic time.

Chapter 3 derives the first estimates of the strength of the double-ionized oxygen lines in individual $z \sim 7$ galaxies. We take advantage of distant gravitationally lensed galaxies behind the massive clusters in the CLASH survey to obtain high signal-to-noise *Spitzer* observations. We select galaxies in a narrow redshift range where the flux from the $4.5 \mu\text{m}$ *Spitzer* band is free of emission line contamination and from the offset in the $3.6 \mu\text{m}$ flux we estimate that extremely strong nebular lines are ubiquitous within $z \sim 7$ galaxies. Our results suggest that the average sSFR of $z \sim 7$ galaxies is significantly higher than previously measured, in good agreement with theoretical predictions.

Chapter 4 presents a new technique to obtain high-precision photometric redshifts of $z \sim 7$ galaxies. Taking advantage of the knowledge that strong oxygen lines are ubiquitous in high-redshift sources, we select galaxies with strong flux offsets in the $3.6 \mu\text{m}$ *Spitzer* band and use the information of the inferred emission lines in the galaxy to place tight constraints on the redshifts of the selected sources. These constraints are particularly useful for studies with the new generation sub-mm telescopes such as *ALMA*; since the wavelength range that *ALMA* can observe in one exposure is limited, inexact knowledge of the redshifts of Lyman-break galaxies inhibits the efficient search for far-infrared emission lines. We apply our technique to 5 fields from the blank-field Cosmic Assembly Near-infrared Deep Extragalactic Legacy Survey (CANDELS) and we select a sample of 20 galaxies. In addition to our selection of sources with well-defined redshifts, our analysis further refines our knowledge of the strength of oxygen lines within high-redshift galaxies.

Chapter 5 investigates two different SFR indicators in a large sample of $z \sim 4$ galaxies. The intrinsic UV properties of high-redshift galaxies provide us with a SFR estimate based on the stars that formed in the last 100 Myr, while we derive estimates of the instantaneous SFR from the strength of the hydrogen lines measured from the *Spitzer* fluxes. We find a strong correlation between the two SFR probes, but with a small yet consistent offset in the normalization. We discuss the possible impact of dust and star formation history on the normalization of the two SFR indicators. Based on the small observed scatter in the UV-based and instantaneous SFRs we argue for relatively smooth star formation histories and rule out short bursts of star formation as the origin of the strong emission lines found in Chapter 3 and 4.

References

- Becker, R. H., Fan, X., White, R. L., et al. 2001, *AJ*, 122, 2850
- Bouwens, R. J., Illingworth, G. D., Oesch, P. A., et al. 2012, *ApJ*, 754, 83
- Bradley, L. D., Bouwens, R. J., Zitrin, A., et al. 2012, *ApJ*, 747, 3
- Cimatti, A., Daddi, E., Renzini, A., et al. 2004, *Nature*, 430, 184
- Coe, D., Zitrin, A., Carrasco, M., et al. 2013, *ApJ*, 762, 32
- Fan, X., Strauss, M. A., Becker, R. H., et al. 2006, *AJ*, 132, 117
- Genzel, R., Tacconi, L. J., Eisenhauer, F., et al. 2006, *Nature*, 442, 786
- González, V., Labbé, I., Bouwens, R. J., et al. 2010, *ApJ*, 713, 115
- Gunn, J. E., & Peterson, B. A. 1965, *ApJ*, 142, 1633
- Hubble, E. P. 1926, *ApJ*, 64, 321
- Kriek, M., van Dokkum, P. G., Franx, M., et al. 2006, *ApJ*, 649, L71
- Madau, P., Pozzetti, L., & Dickinson, M. 1998, *ApJ*, 498, 106
- Oesch, P. A., Bouwens, R. J., Illingworth, G. D., et al. 2012, *ApJ*, 745, 110
- Penzias, A. A., & Wilson, R. W. 1965, *ApJ*, 142, 419
- Perlmutter, S., Aldering, G., Goldhaber, G., et al. 1999, *ApJ*, 517, 565
- Planck Collaboration, Ade, P. A. R., Aghanim, N., et al. 2014, *A&A*, 571, AA16
- Planck Collaboration, Ade, P. A. R., Aghanim, N., et al. 2015, arXiv:1502.01589
- Riess, A. G., Filippenko, A. V., Challis, P., et al. 1998, *AJ*, 116, 1009
- Rowan-Robinson, M., Broadhurst, T., Oliver, S. J., et al. 1991, *Nature*, 351, 719
- Schaerer, D., & de Barros, S. 2009, *A&A*, 502, 423
- Smoot, G. F., Bennett, C. L., Kogut, A., et al. 1992, *ApJ*, 396, L1
- Shim, H., Chary, R.-R., Dickinson, M., et al. 2011, *ApJ*, 738, 69
- Stark, D. P., Schenker, M. A., Ellis, R., et al. 2013, *ApJ*, 763, 129
- Steidel, C. C., Giavalisco, M., Pettini, M., Dickinson, M., & Adelberger, K. L. 1996, *ApJ*, 462, L17
- Weinmann, S. M., Neistein, E., & Dekel, A. 2011, *MNRAS*, 417, 2737
- Wuyts, S., Förster Schreiber, N. M., van der Wel, A., et al. 2011, *ApJ*, 742, 96

2

The Star Formation Rate Function for Redshift $z \sim 4 - 7$ Galaxies: Evidence for a Uniform Build-up of Star-Forming Galaxies during the First 3 Gyr of Cosmic Time.

We combine recent estimates of dust extinction at $z \sim 4 - 7$ with UV luminosity function (LF) determinations to derive star formation rate (SFR) functions at $z \sim 4, 5, 6$ and 7 . SFR functions provide a more physical description of galaxy build-up at high redshift and allow for direct comparisons to SFRs at lower redshifts determined by a variety of techniques. Our SFR functions are derived from well-established $z \sim 4 - 7$ UV LFs, UV-continuum slope trends with redshift and luminosity, and IRX- β relations. They are well-described by Schechter relations. We extend the comparison baseline for SFR functions to $z \sim 2$ by considering recent determinations of the H α and mid-IR luminosity functions. The low-end slopes of the SFR functions are flatter than for the UV LFs, $\Delta\alpha \sim +0.13$, and show no clear evolution with cosmic time ($z \sim 0 - 7$). In addition, we find that the characteristic value SFR* from the Schechter fit to SFR function exhibits consistent, and substantial, linear growth as a function of redshift from $\sim 5 M_{\odot}\text{yr}^{-1}$ at $z \sim 8$, 650 Myr after the Big Bang, to $\sim 100 M_{\odot}\text{yr}^{-1}$ at $z \sim 2$, ~ 2.5 Gyr later. Recent results at $z \sim 10$, close to the onset of galaxy formation, are consistent with this trend. The uniformity of this evolution is even greater than seen in the UV LF over the redshift range $z \sim 2 - 8$, providing validation for our dust corrections. These results provide strong evidence that galaxies build up uniformly over the first 3 Gyr of cosmic time.

2.1 Introduction

In recent years great progress has been made in determining the UV luminosity function (LF) at early times (e.g., Steidel et al., 1999; Wyder et al., 2005; Arnouts et al., 2005; Reddy & Steidel, 2009; Bouwens et al., 2007, 2011b; Oesch et al., 2010, 2012b). Recent results on the UV LF indicate a bright end that builds up substantially with time, with the characteristic luminosity increasing from the highest redshifts to $z \sim 3 - 4$ (e.g. Bouwens et al., 2007). Furthermore, the faint-end slope of the UV LF is found to be very steep at redshifts $z \gtrsim 3$ (e.g. Bouwens et al., 2011b). This brightening of L_{UV}^* and steep faint-end slope α are consistent with a general picture where galaxies build up hierarchically and where lower luminosity galaxies play a major role in the reionization of the universe.

Despite the general usefulness of the UV LF for probing early galaxy formation, one significant limitation of the UV LF in this regard is the sensitivity of rest-frame UV light to dust extinction. Inferring this attenuation directly at $z > 3$ is challenging since only the most bolometrically luminous systems at these redshifts can be detected in far-IR. Also, for these very high redshifts, tracers of star formation such as X-ray, radio, $24\mu\text{m}$ and $\text{H}\alpha$ are either too faint to observe or redshifted out of the observable wavelength range of the most sensitive telescopes.

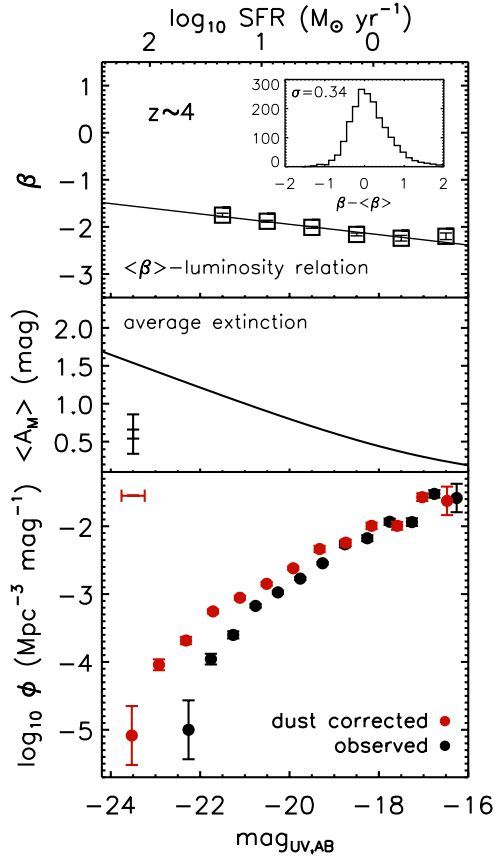
Fortunately, we can take advantage of a relation between the UV-continuum slope β , with $f_\lambda \propto \lambda^\beta$ (Meurer et al., 1999), and the likely dust extinction to convert the observed UV-luminosities into SFRs (see e.g. Bouwens et al., 2009). It has only now been possible to accurately establish the distribution of the UV-continuum slope distribution over a wide range in luminosity and redshift (e.g. Bouwens et al., 2009, 2011; Wilkins et al., 2011; Finkelstein et al., 2011; Castellano et al., 2012; Dunlop et al., 2012). This is the result of the installation of the WFC3/IR camera on the Hubble Space Telescope and the recent acquisition of deep wide-area data over the HUDF09+CANDELS fields (Bouwens et al., 2011; Grogin et al., 2011; Koekemoer et al., 2011).

In this chapter, we utilize these new UV-continuum slope determinations to derive SFR functions at $z \sim 4, 5, 6$ and 7 . SFR functions can better connect the growth of galaxies at the highest redshifts to galaxies found at later epochs, as well as give insight into the manner in which star formation lights up dark matter halos. Previously, such functions were presented at $z \sim 0 - 1$ based on UV+IR data (Martin et al., 2005; Bell et al., 2007; Bothwell et al., 2011). We begin this chapter by describing how we use β to produce dust-corrected UV LFs and SFR functions (§2). In §3 we compare our SFR functions with the literature over a range of redshifts ($z \sim 0 - 8$). For ease of comparison with previous studies we adopt $H_0 = 70 \text{ km s}^{-1} \text{ Mpc}^{-1}$, $\Omega_m = 0.3$ and $\Omega_\Lambda = 0.7$. We adopt a Salpeter (1955) IMF with limits $0.1\text{-}125 M_\odot$ throughout this chapter.

2.2 SFR functions

This section describes how we compute SFR functions from published UV LFs and UV-continuum slopes β . We begin by deriving the SFR functions in a fully stepwise fashion, applying our luminosity-dependent dust corrections to binned UV LFs (Section 2.1). We then derive analytical formulae for these SFR functions based on the UV LFs we use as inputs (Section 2.2).

Figure 2.1: *Top:* The relation between the UV-continuum slope β and UV luminosity at $z \sim 4$ from Bouwens et al. (2011) with the binned points and linear fit $\langle \beta \rangle = -0.11 (M_{\text{UV,AB}} + 19.5) - 2.00$. The inset panel shows the luminosity de-trended distribution of UV-continuum slopes around the mean relation. *Middle:* The average dust extinction from the β -distribution in the upper panel as a function of luminosity, assuming a Meurer et al. (1999) dust correction, as described in §2.2.1. The errorbar in the bottom left corner shows both the random and systematic uncertainties in the relation. *Bottom:* The black and red points show the $z \sim 4$ UV LF from Bouwens et al. (2007) before and after correction for dust (see §2.2.1). The errorbar in the top left corner shows the fiducial error in the average dust correction. The dust-corrected UV LF has a flatter faint-end slope α and brighter M_{UV}^* .



2.2.1 Dust-corrected luminosity functions

We correct UV LFs for the effects of dust attenuation using the well-known correlation of extinction with the UV-continuum slope β . We take the IRX- β relation established by Meurer et al. (1999),

$$A_{1600} = 4.43 + 1.99 \beta. \quad (2.1)$$

Meurer et al. (1999) estimated the relation based on starburst galaxies in the local universe. Similar relations have been found at $z \sim 0$ by other groups (Burgarella et al., 2005; Overzier et al., 2011). Though there is some evidence that the Meurer et al. (1999) relation does not work well for all sources, e.g. very young galaxies (< 100 Myr) and ULIRGs (e.g. Reddy et al., 2006), this relation has been found to be accurate in the mean out to $z \sim 2$, despite considerable scatter (e.g. Daddi et al., 2007; Reddy et al., 2006, 2010, 2012; Magdis et al., 2010a; Magdis et al., 2010). There is even evidence in the new Herschel observations that the Meurer et al. (1999) relation is reasonably accurate in estimating the dust extinction for $z \sim 2$ Lyman-Break Galaxies (Reddy et al., 2012). We therefore quite reasonably utilize this relation in interpreting higher redshift samples.

Recently there have been a number of studies examining β in high-redshift samples (e.g. Bouwens et al., 2009; Wilkins et al., 2011; Bouwens et al., 2011; Finkelstein et al., 2011; Dunlop et al., 2012). Perhaps the most definitive of these studies is Bouwens et al. (2011), who using the CANDELS+HUDF09 datasets find that β correlates with both redshift and luminosity, with higher redshift and lower luminosity galaxies being bluer. The results by Bouwens et al. (2011) are in excellent agreement with other results in the literature (e.g. Ouchi et al., 2004; Labbé et al., 2007; Overzier et al., 2008; Wilkins et al., 2011).

For our dust corrections we assume a linear relation between the UV-continuum slope β and luminosity, such as that given in Bouwens et al. (2011). This is shown in the top panel of Figure 2.1 for $z \sim 4$,

$$\langle \beta \rangle = \frac{d\beta}{dM_{UV}}(M_{UV,AB} + 19.5) + \beta_{M_{UV}=-19.5}, \quad (2.2)$$

where $\frac{d\beta}{dM_{UV}}$ and $\beta_{M_{UV}=-19.5}$ are from Table 5 of Bouwens et al. (2011). Note that for $z \sim 7$ we use a fit with a fixed slope $\frac{d\beta}{dM_{UV}} = -0.13$ obtained from our $z \sim 4 - 6$ samples, given the large uncertainties in this slope at $z \sim 7$ and the lack of evidence for evolution in the β -luminosity relation over the redshift range $z \sim 2 - 6$. The distribution of UV-continuum slope β shows substantial scatter about relation 2, that can be approximated by a normal distribution (Figure 2.1; but remark there is a fatter tail toward redder β).

The steps for computing an average dust correction are as follows. We use Eq. 2.1 to calculate the UV absorption A_{1600} for each source in our adopted β -distribution. Then to obtain the extinction correction at a given M_{UV} we integrate over the β -distribution (normal distribution with mean $\langle \beta \rangle$, Eq. 2.2, and $\sigma_{\beta}=0.34$), setting $A_{1600} = 0$ when $A_{1600} < 0$. The middle panel of Figure 2.1 shows the resulting $\langle A_{M_{UV}} \rangle$ as a function of luminosity at $z \sim 4$. We then apply this dust correction to the UV luminosities of individual bins of the LF. We shift each point in the LF toward brighter magnitudes and correct for the fact that the luminosity-dependent dust correction increases the width of the bins.

The bottom panel of Figure 2.1 shows the effect of our luminosity-dependent dust correction on the stepwise UV LF at $z \sim 4$ from Bouwens et al. (2007). The dust correction shifts the LF to higher luminosities, particularly at the bright end, causing M_{UV}^* to brighten, and also flattens the faint-end slope. There is also a small shift to lower volume densities due to the renormalisation of the magnitude bins.

Now that we have dust-corrected UV fluxes we can use well-established relations to compute the SFR as a function of luminosity, giving us our desired SFR functions. We use the following relation from Kennicutt (1998),

$$\frac{\text{SFR}}{M_{\odot}\text{yr}^{-1}} = 1.25 \cdot 10^{-28} \frac{L_{UV,corr}}{\text{erg s}^{-1}\text{Hz}^{-1}}. \quad (2.3)$$

Since this relation gives the time-averaged SFR over a ~ 100 Myr time window, it will underestimate the SFR (typically by $\lesssim 2\times$) in galaxies substantially younger than this (e.g. Verma et al., 2007; Bouwens et al., 2011; Reddy et al., 2012). However, Eq. 2.3 should work on average for the extended SF histories expected in LBGs.

The left panel of Figure 2.2 shows the stepwise SFR functions at $z \sim 4, 5, 6$ and 7 , based on stepwise UV LFs derived from Bouwens et al. (2007) and Bouwens et al. (2011b). For convenience, we include our stepwise SFR functions in Table 2.1.

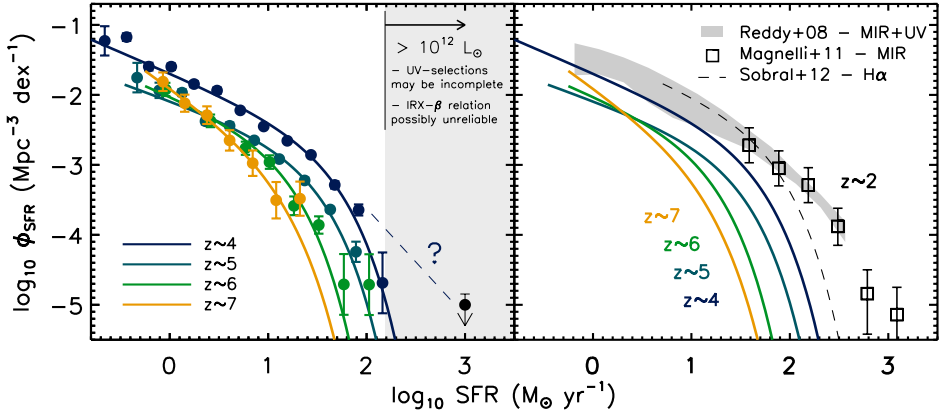


Figure 2.2: *Left:* Both the analytical and stepwise SFR functions derived in this study from dust-corrected UV LFs. The stepwise SFR functions (individual points) were derived using the UV LF results from Bouwens et al. (2007, 2011b), as described in §2.2.1. The solid lines are the SFR functions derived in Schechter form as described in §2.2.2 with parameters listed in Table 2.2. The lines are *not* fits to the points. The excellent agreement between the two approaches provides a useful cross-check. We have indicated the SFRs ($> \sim 150 M_{\odot} \text{yr}^{-1}$: equivalent to a bolometric luminosity $> 10^{12} L_{\odot}$) where we expect our SFR functions to be more uncertain due to incompleteness in the UV selections and possible unreliability of the IRX- β relation (e.g. Reddy et al., 2006). The best estimates at high SFRs may come from searches in the mid-IR/far-IR (black point from Daddi et al., 2009, see also Marchesini et al., 2010). The SFR function therefore may fall off more slowly than we infer (dashed line). *Right:* A comparison of the SFR functions with similar functions derived from the bolometric LF of Reddy et al. (2008, *grey region*), the IR LF of Magnelli et al. (2011, *black open squares*) and the H α LF from Sobral et al. (2012, *black dashed line*) at $z \sim 2$. The trend in the SFR function, derived from our dust-corrected UV LFs at $z \sim 4 - 7$, clearly extends to $z \sim 2$. The smooth evolution in the SFR function provides some corroboration for the dust corrections we apply.

2.2.2 Analytical SFR functions

In this section, we use an analytical Schechter-like approximation to represent SFR functions at $z \sim 4 - 7$.

We assume that the IRX- β relation for individual galaxies is described by $A_{\text{UV}} = C_0 + C_1 \beta$ and the distribution of galaxies at a certain M_{UV} is given by a Gaussian with $\mu_{\beta} = \langle \beta \rangle$ (Eq. 2.2) and width σ_{β} , which gives

$$\langle A_{M_{\text{UV}}} \rangle = C_0 + 0.2 \ln 10 C_1^2 \sigma_{\beta}^2 + C_1 \langle \beta \rangle. \quad (2.4)$$

This expression is only valid in the limit that the distribution of UV-continuum slopes β does not extend to $\beta \lesssim -2.3$ since such blue β 's formally give negative dust corrections (a clearly non-physical result) using the Meurer et al. (1999) relation. For the Meurer et al. (1999) relation Eq. 2.4 simplifies to $\langle A_{M_{\text{UV}}} \rangle = 4.43 + 1.82 \sigma_{\beta}^2 + 1.99 \langle \beta \rangle$.

To compute SFR functions we start with the UV LF, described in Schechter form (Schechter, 1976):

$$\phi(L) dL = \phi^* \left(\frac{L}{L^*} \right)^{\alpha} \exp \left(-\frac{L}{L^*} \right) \frac{dL}{L^*}. \quad (2.5)$$

Substituting SFR for L (and SFR* for L*), using Eq. 2.2, 2.3 and 2.4 yields

$$\phi(\text{SFR}) d\text{SFR} = \frac{\phi^*}{1 - C_1 \frac{d\beta}{dM}} \left(\frac{\text{SFR}}{\text{SFR}^*} \right)^{\frac{\alpha + C_1 \frac{d\beta}{dM}}{1 - C_1 \frac{d\beta}{dM}}} \times \exp\left(-\frac{\text{SFR}}{\text{SFR}^*}\right) \frac{d\text{SFR}}{\text{SFR}^*}. \quad (2.6)$$

where we have made the simplifying assumption that the cut-off in the Schechter function is exponential and not some slightly shallower high-end cut-off (the modified functional form is consistent with the observations). This gives the conversions

$$\alpha_{\text{SFR}} = \frac{\alpha_{\text{UV,uncorr}} + C_1 \frac{d\beta}{dM}}{1 - C_1 \frac{d\beta}{dM}} \quad (2.7)$$

$$\phi_{\text{SFR}}^* = \frac{\phi_{\text{UV,uncorr}}^*}{1 - C_1 \frac{d\beta}{dM}}. \quad (2.8)$$

We calculate SFR^* using Eq. 2.2, 2.3 and 2.4, i.e. we use $\log_{10} \text{SFR}^* = -0.4 (M_{\text{UV,uncorr}}^* - < A_{M_{\text{UV}}}^* >) - 7.25$. Though Eq. 2.4 is a reasonable approximation for $< A_{M_{\text{UV}}}^* >$, our estimate of SFR^* is slightly more accurate when we estimate $< A_{M_{\text{UV}}}^* >$ as described in §2.2.1, by setting $A_{1600} = 0$ when $A_{1600} < 0$. Therefore we will use this more accurate estimate of SFR^* quoted in Table 2.2.

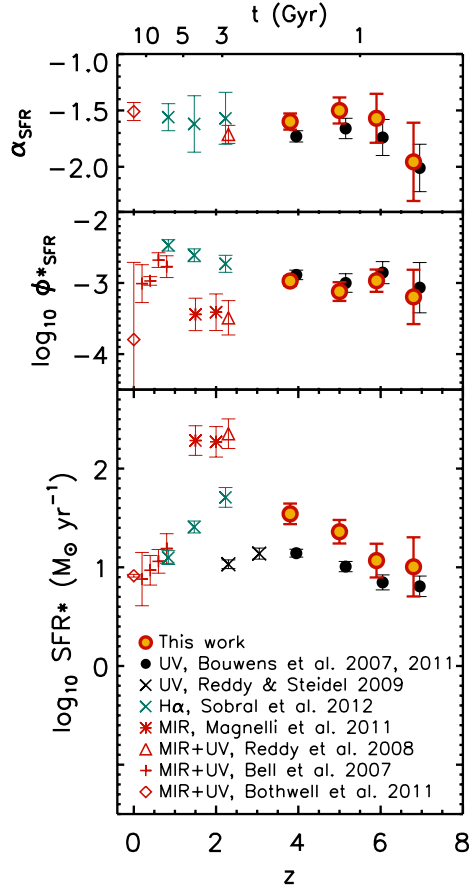
The left panel of Figure 2.2 compares the analytical SFR functions (solid lines) with the corrected stepwise UV LFs described in §2.2.1. They are in excellent agreement, providing a useful check on the analytic description used here. We would expect our derived SFR functions to be more uncertain at high bolometric luminosities ($L_{\text{bol}} > 10^{12} L_{\odot}$; indicated on Figure 2.2) where dust corrections are likely less reliable (e.g. Reddy et al., 2006) and our Lyman-break selections may be more incomplete to dusty star-forming galaxies (e.g. Daddi et al., 2009; Michałowski et al., 2010). While this should not affect the turnover in the SFR function, the SFR function may fall off less steeply than the exponential form adopted here.

The analytical Schechter parameters are presented in Table 2.2. The SFR^* , ϕ_{SFR}^* and α_{SFR} are calculated assuming the $z \sim 4 - 7$ UV LF parameters from Bouwens et al. (2007) and Bouwens et al. (2011b), the $\frac{d\beta}{dM}$, $\beta_{M_{\text{UV}}=-19.5}$ and $\sigma_{\beta} = 0.34$ from Bouwens et al. (2011) and the Meurer et al. (1999) relation (Eq. 2.1). For the $z \sim 7$ LF parameters, we modify our procedure somewhat due to the fact that Eq. 2.4 is not especially accurate for the very blue β 's found at $z \sim 7$ (see discussion following Eq. 2.4). Specifically, we keep the SFR^* fixed to the value described above and then fit the low-end slope and the normalisation of the Schechter function to the stepwise UV LF.

We have verified through Monte-Carlo simulations that we can successfully recover ($\Delta M^* \lesssim 0.13$ mag, $\Delta \alpha \lesssim 0.03$) the observed UV LFs and β -luminosity relation using the derived SFR functions and a β -SFR relation (e.g. Castellano et al., 2012), so our approach can be inverted. We describe these simulations in detail in Appendix A.

We remark that if β shows a weaker dependence on luminosity than Bouwens et al. (2011) find (e.g. Castellano et al., 2012; Dunlop et al., 2012) it would result in a steeper α_{SFR} ($\Delta \alpha \sim 0.1$) and higher ϕ_{SFR}^* ($\Delta \phi_{\text{SFR}}^* \sim 0.05$ dex). Uncertainties in both the incompleteness and contamination

Figure 2.3: Derived Schechter parameters α_{SFR} (*top*), ϕ_{SFR}^* (*middle*) and SFR^* (*bottom*) as a function of redshift. The red points show the derived dust-corrected SFR function parameters, while the black points and crosses show equivalent parameters for the UV LFs from Bouwens et al. (2007, 2011b) and Reddy & Steidel (2009), respectively, before dust correction (black points are shifted +0.15 on the x-axis for clarity). The error bars for our parameters include both the random and systematic uncertainties in $\frac{d\beta}{dM}$ and $\beta_{M_{\text{UV}}} = -19.5$. We compare to SFR parameters obtained from Bothwell et al. (2011, *red diamonds*), Bell et al. (2007, *red plus signs*), Reddy et al. (2008, *red triangles*), Magnelli et al. (2011, *red asterisks*) and Sobral et al. (2012, *red crosses*), as described in §2.3. Our dust corrections result in flatter faint-end slopes α ($\Delta\alpha \sim +0.13$) relative to the UV LF (§2.3.2). Our dust correction also doubles the rate at which $\log_{10} \text{SFR}^*$ grows with cosmic time over the redshift range $z \sim 4 - 7$ (§2.3.1). Clearly, dust corrections can have a significant impact on the apparent evolution of SF galaxies with time.



corrections used for the UV LFs, of course, also affect our SFR functions (e.g. Bouwens et al., 2007; Grazian et al., 2011).

2.3 Results

One of the main results of this chapter is our determination of the approximate Schechter parameters for the SFR function. These parameters allow for an intuitive and quantitative look at how this function evolves with cosmic time, as well as allowing for a comparison with lower redshift determinations. We discuss both the high-SFR and low-SFR end of the SFR function.

2.3.1 High-SFR end: linear build-up of $\log \text{SFR}^*$ from $z \sim 8$ to $z \sim 2$

The high-SFR end of the SFR function is interesting since it provides us with a direct measure of the rate at which luminous galaxies are building up at early times. We compare our parameters with various studies that combine UV and IR observations to obtain complete SFR functions at

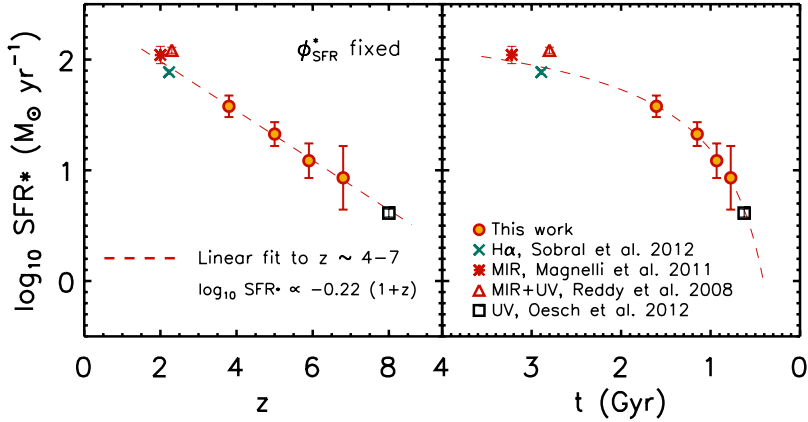


Figure 2.4: The turnover SFR^* at fixed ϕ_{SFR}^* as a function of redshift (*left*) and cosmic time (*right*). The SFR^* from Magnelli et al. (2011), Sobral et al. (2012), Reddy et al. (2008) and Oesch et al. (2012) are indicated with a red asterisk, cross, triangle and square, respectively. The dashed line gives a linear fit to our derived $\log_{10} \text{SFR}^*$ at $z \sim 4 - 7$, with $\log_{10} \text{SFR}^* \propto -0.22(1+z)$ (§2.3.1). The fit at $z \sim 4 - 7$ is in broad agreement with the literature over the entire range $z \sim 8$ to $z \sim 2$. The extrapolated fit also agrees with the current estimate for SFR^* at $z \sim 10$ (Bouwens et al., 2011a; Oesch et al., 2012b), but the uncertainties in this estimate are still quite large. This provides strong evidence that galaxies build up consistently with time, from $z \sim 8$ to $z \sim 2$.

$z \lesssim 2$, i.e. Bothwell et al. (2011), Bell et al. (2007) and Reddy et al. (2008) and also with $\text{H}\alpha$ and IR LFs at $z \sim 2$ from Sobral et al. (2012) and Magnelli et al. (2011) respectively. We expect the IR LFs to probe the SFRs in the dominant population of dusty galaxies (ULIRG+LIRGs) at $z \sim 2$. We use the relations from Kennicutt (1998) to convert the $\text{H}\alpha$ and bolometric luminosities to SFRs. The SFR functions at $z \sim 2$ are shown in the right panel of Figure 2.2; these SFR functions are in reasonable agreement with each other, except at the high-SFR end where the $\text{H}\alpha$ LF is low. This may result from an incomplete sampling (or inadequate dust corrections) of dusty galaxies by the $\text{H}\alpha$ study. The $z \sim 2$ SFR functions are consistent with the evolution observed between $z \sim 4 - 7$.

The bottom panel of Figure 2.3 (see also Table 2.3) shows SFR^* for our results at $z \sim 4 - 7$ with the SFR^* from published studies mentioned above. The black symbols (Bouwens et al., 2007, 2011b; Reddy & Steidel, 2009) represent the equivalent SFR^* one would derive without applying a dust correction. There is a significant difference in the evolution of the high-SFR end of the SFR function taking dust attenuation into account: SFR^* (without a dust correction) peaks at $\sim 20 M_{\odot} \text{yr}^{-1}$ for $z \sim 3 - 4$, while SFR^* derived from dust-corrected UV or MIR LFs continues to increase from $\sim 10 M_{\odot} \text{yr}^{-1}$ at $z \sim 7$ to $\sim 100 M_{\odot} \text{yr}^{-1}$ at $z \sim 2$.

In Figure 2.4 we show the evolution of SFR^* at fixed ϕ_{SFR}^* (with $\log_{10} \phi_{\text{SFR}}^* = -3.05$: see also Table 2.4). This is interesting since it allows us to examine the evolution in the high-end of the SFR function without introducing additional "noise" from the $\text{SFR}^* - \phi_{\text{SFR}}^*$ degeneracy. We extend our comparison of SFR^* to $z \sim 8$ using the Oesch et al. (2012) UV LF (see also Trenti et al., 2011; Bradley et al., 2012). The effect of the dust correction on SFR^* decreases strongly with redshift for $z \gtrsim 4$ and we expect the contribution at $z \sim 8$ to be nearly negligible. We fit a linear slope to our own estimates of $\log_{10} \text{SFR}^*$ at $z \sim 4 - 7$ and find $\log_{10} \text{SFR}^* = 2.43 - 0.22(1+z)$

(Figure 2.4). The SFR functions without a dust correction follow $\log_{10} \text{SFR}^* \propto -0.11(1+z)$. Comparing the two, we see that our dust corrections double the rate at which the high-SFR end of the SFR function grows with cosmic time (see also the discussion in §6.2 of Bouwens et al. 2006).

Extrapolating the best fit SFR*-redshift relation to higher and lower redshift we find good agreement with $z \sim 2$ and $z \sim 8$ determinations of SFR* (Figure 2.4). The estimate for $z \sim 10$ from Oesch et al. (2012b) is also consistent with the trend, but the uncertainty in SFR* at that redshift is still quite large. The evolution of SFR* with redshift at fixed ϕ^* suggests that galaxies build up in a consistent way during the first 3 Gyr of cosmic time. Moreover, the excellent agreement between different probes of star formation across cosmic time, provides a valuable cross-check on the validity of the dust corrections we use.

Papovich et al. (2011) also consider an evolving SFR vs. redshift relation based on an abundance-matched selection. Not surprisingly, given that Papovich et al. (2011) use essentially the same UV LFs (from Bouwens et al., 2007, 2011b) and similar dust corrections at $z \gtrsim 4$ as we use here (from Bouwens et al. 2009 instead of Bouwens et al. 2011), they find similar SFRs over the range $z \sim 4-8$ (at constant number density $n(> \text{SFR}) = 2 \times 10^{-4} \text{Mpc}^{-3}$, see Table 2.4). However, the present analysis suggests much more clearly that the build-up in the SFRs of galaxies extends not simply from $z \sim 8$ to $z \sim 4$, but continues all the way to $z \sim 2$.

2.3.2 Low-SFR end: flatter slopes and large uncertainties

The low-end slope of the SFR function is interesting, since it provides us with insight into the physics and feedback effects in the lowest luminosity galaxies when compared to the dark matter halo mass function. The top panel of Figure 2.3 shows how the low-end slope α of the SFR function evolves as a function of redshift. The evolution of dust-corrected α_{SFR} contrasts with the original slope of the UV LF. α_{SFR} is typically $\Delta\alpha \sim +0.13$ flatter on average. Comparing α_{SFR} with similar determinations at lower redshift (Bothwell et al., 2011; Reddy et al., 2008; Sobral et al., 2012), we find no evidence for evolution with cosmic time.

2.4 Summary

In this chapter we combine UV LFs with dust corrections based on the UV-continuum slope β and the IRX- β relation, to produce star formation rate functions between $z \sim 4-7$. The dust correction results in a flatter faint-end slope and brighter M_{UV}^* .

We find SFR functions that, at fixed ϕ^* , show a steady build-up in their value of SFR* with cosmic time, from $\sim 5 M_{\odot} \text{yr}^{-1}$ at $z \sim 8$ to $\sim 100 M_{\odot} \text{yr}^{-1}$ at $z \sim 2$, providing evidence that galaxies build up in a very uniform fashion in the first 3 Gyr (to $z \sim 2$). Use of the SFR function allows us to naturally link the evolution of normal star-forming galaxies at $z \gtrsim 4$ with the population of dusty star-forming galaxies seen at $z \sim 2-3$.

Acknowledgements

We thank Naveen Reddy, David Sobral and Marcel van Daalen for useful discussions. We are thankful to Naveen Reddy for sending us the information necessary to make a comparison with

the bright $z \sim 2$ spectroscopic sample from Reddy et al. (2010). Feedback from the referee significantly improved this chapter. We acknowledge the support of a NWO vrije competitie grant, ERC grant HIGHZ #227749, and NASA grant HST-GO-11563.01. PO acknowledges support from NASA through a Hubble Fellowship grant #51278.01 awarded by STScI.

Appendix

A. Monte-Carlo simulation to recover the UV LF and β -luminosity relation

In this study we derive SFR functions by transforming the UV LF using a luminosity dependent dust correction. However, one might suppose that the dust correction may be better parametrized in terms of the SFR instead of the UV luminosity – given that the SFR is the more physical quantity and dust extinction is known to be well-correlated with the SFR (e.g. Reddy et al., 2006). It is therefore worthwhile investigating whether we can start with our derived SFR functions and then recover the two inputs to the SFR function, i.e., the rest-frame UV LF and the observed β -UV luminosity relationship. This will allow us to test whether the SFR functions we derive are sensitive to our parametrizing the mean β as a function of observed UV luminosity (instead of parametrizing it in terms of the SFR). We perform this test at $z \sim 4$, where both the observed UV-luminosity function and the observed β -UV luminosity relation are best determined.

The steps in the simulation are as follows. We start with our $z \sim 4$ SFR function and we produce a mock data set with each galaxy in the data set having a SFR and β . The initial β distribution is drawn from a normal distribution with a mean value equal to $\langle \beta \rangle = \frac{d\beta}{dM_{\text{bol}}}(M_{\text{bol}} + 19.5) + \beta_{M_{\text{bol}}=-19.5}$ and a scatter equal to σ_{int} . This is shown with the grey area in the top left panel of Figure 2.5 as β versus bolometric luminosity and the simulated bolometric luminosity function is shown on the bottom left panel of Figure 2.5.

Assuming the Meurer et al. (1999) relation to calculate dust attenuation, we obtain the observed UV luminosities for each galaxy in this mock data set from the SFRs, as shown in the top right panel of Figure 2.5. We derive the β versus SFR distribution in an iterative process so as to best reproduce the observed β -UV luminosity relationship with $\langle \beta \rangle = -0.11 (M_{\text{UV,AB}} + 19.5) - 2.00$ and observed scatter $\sigma_{\text{obs}} = 0.34$ (Bouwens et al., 2011). The best-fit β vs. M_{bol} distribution has the form: $\langle \beta \rangle = -0.17 (M_{\text{bol}} + 19.5) - 1.91$ and $\sigma_{\text{int}} = 0.30$.

As a check on our derived β vs. SFR distribution we have plotted the measurements from Reddy et al. (2010) in the top left panel of Figure 2.5. Reddy et al. (2010) use rest-frame UV and $24\mu\text{m}$ observations of $z \sim 2$ galaxies to study the properties of star-forming galaxies as a function of their bolometric luminosities. The agreement between the bright end of our simulated dataset and the Reddy et al. (2010) measurements is encouraging, though we note that at fixed bolometric luminosity one might expect $z \sim 2$ galaxies to have somewhat higher dust content and therefore redder β values than our $z \sim 4$ galaxies due to evolution in dust extinction vs. SFR relation (e.g. Reddy et al., 2006; Buat et al., 2007). The Reddy et al. (2010) measurements therefore provide a rough upper limit to the steepness of the β -SFR relation at $z \sim 4$.

We convert the simulated observed distribution to a luminosity function and compare this simulated observed UV LF with the UV LF of Bouwens et al. (2007, see the bottom right panel

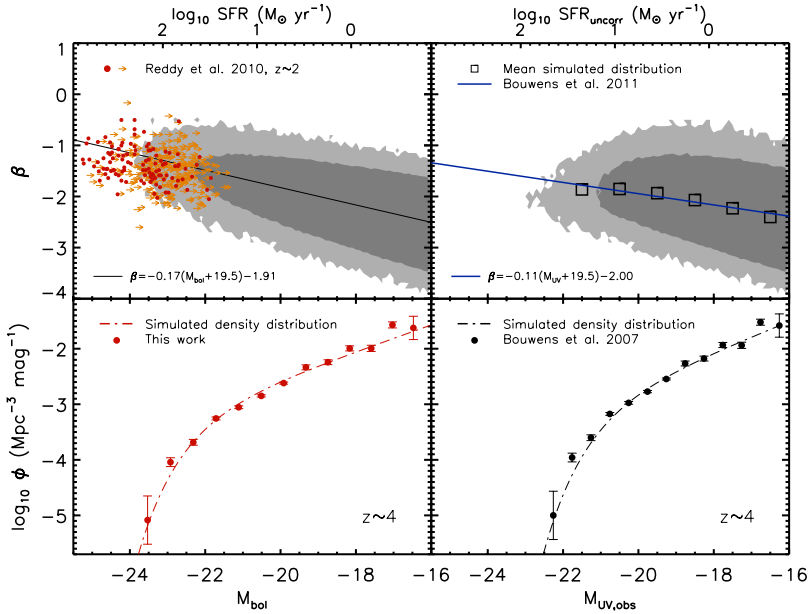


Figure 2.5: Demonstration that we can use the SFR function to recover the two inputs to the SFR function as described in Appendix A. We show the bolometric luminosity function at $z \sim 4$ (equivalent to the SFR function with parameters in Table 2.2) in the lower left panel and a β vs. bolometric luminosity relation (equivalent to a β vs. SFR relation) in the upper left panel. The upper right panel shows the β vs. observed UV luminosity relation we are attempting to reproduce with our simulations, and the lower right panel shows the UV LF. The gray area in the top left panel indicates our initial mock dataset, with each mock galaxy having a β drawn from a normal distribution with a mean $\langle \beta \rangle = -0.17 (M_{\text{bol}} + 19.5) - 1.91$ and a L_{bol} from the bolometric LF in the bottom left panel. Also plotted are the bolometric luminosities (red dots) and upper limits (orange arrows) of Reddy et al. (2010) based on their rest-frame UV-luminosities and *Spitzer* MIPS $24\mu\text{m}$ flux measurements. The top right panel shows the simulated distribution as a function of UV luminosity, which we derive by dust correcting the bolometric luminosities based on the intrinsic β values for the individual mock galaxies. The black squares indicate the mean β 's we recover as a function of luminosity in these simulations, while the blue line gives the observed relation found in Bouwens et al. (2011). The bottom right panel shows that the UV LF we recover from these simulations (dot dashed lines) matches up well with the observed UV LF from Bouwens et al. (2007) at $z \sim 4$ (black circles and error bars).

of Figure 2.5). The two LFs are in quite reasonable agreement. The characteristic luminosity M^* we find is within 0.13 mag of the derived LF of Bouwens et al. (2007) and the faint-end slope α we find is within 0.03 of the slope Bouwens et al. (2007) find. These differences are smaller than our current error bars for our SFR function parameters at $z \sim 4$.

This simulation gives us confidence that our derived SFRs are not subject to large biases due to incompleteness at the faint end of the distribution. Furthermore, these simulations suggest that dust extinction is not so large at the bright end of the LF that we are unable to approximately recover the SFR function. Overall, these test results provide some validation for our methodology for performing the dust corrections.

Table 2.1: Stepwise determinations of the SFR function at $z \sim 4$, $z \sim 5$, $z \sim 6$ and $z \sim 7$ (see §2.2.1)

$\log_{10} \text{SFR} (M_{\odot} \text{yr}^{-1})$	$\phi_{\text{SFR}} (Mpc^{-3} \text{dex}^{-1})$
$z \sim 4$	
-0.66	0.05920±0.02855
-0.44	0.06703±0.00838
-0.21	0.02537±0.00326
0.02	0.02534±0.00268
0.25	0.01430±0.00144
0.48	0.01153±0.00117
0.72	0.00601±0.00025
0.95	0.00354±0.00017
1.19	0.00221±0.00012
1.44	0.00139±0.00008
1.68	0.00052±0.00006
1.92	0.00023±0.00004
2.16	0.00002±0.00002
$z \sim 5$	
-0.33	0.01766±0.00858
-0.11	0.01161±0.00294
0.12	0.01076±0.00121
0.36	0.00420±0.00046
0.61	0.00362±0.00040
0.86	0.00224±0.00014
1.11	0.00121±0.00008
1.37	0.00060±0.00006
1.63	0.00023±0.00002
1.89	0.00006±0.00002
$z \sim 6$	
-0.04	0.01197±0.00262
0.41	0.00426±0.00089
0.77	0.00173±0.00037
1.01	0.00110±0.00024
1.26	0.00026±0.00008
1.51	0.00014±0.00004
1.77	0.00002±0.00002
2.03	0.00002±0.00002
$z \sim 7$	
-0.07	0.01543±0.00473
0.15	0.00761±0.00215
0.38	0.00513±0.00149
0.61	0.00224±0.00075
0.84	0.00106±0.00044
1.08	0.00031±0.00019
1.32	0.00033±0.00018

Table 2.2: Schechter parameters determined for the present SFR functions

$\langle z \rangle$	$\log_{10} \frac{\text{SFR}^*}{M_{\odot} \text{ yr}^{-1}}$	$\phi_{\text{SFR}}^* (10^{-3} \text{ Mpc}^{-3})$	α_{SFR}
3.8	1.54 ± 0.10	1.07 ± 0.17	-1.60 ± 0.07
5.0	1.36 ± 0.12	0.76 ± 0.23	-1.50 ± 0.12
5.9	1.07 ± 0.17	1.08 ± 0.39	-1.57 ± 0.22
6.8	1.00 ± 0.30	0.64 ± 0.56	-1.96 ± 0.35

Notes. These Schechter parameters are obtained by dust correcting the UV LF using the Meurer et al. (1999) IRX- β relationship. We adopt the linear relation between the UV-continuum slope β and UV luminosity (Eq. 2.2) found by Bouwens et al. (2011). See §2.2.2.

Table 2.3: Schechter parameters for SFR functions in the literature (see also Figure 2.3)

$\langle z \rangle$	$\log_{10} \frac{\text{SFR}^*}{M_{\odot} \text{ yr}^{-1}}$	$\log_{10} \frac{\phi_{\text{SFR}}^*}{\text{Mpc}^{-3}}$	α_{SFR}	probe	reference
0.0	0.91 ± 0.01	-3.80 ± 1.09	-1.51 ± 0.08	MIR+UV	Bothwell et al. 2011 ^a
0.2	0.88 ± 0.27	-3.01 ± 0.27	-1.45 (fixed)	MIR+UV	Bell et al. 2007
0.4	0.97 ± 0.15	-2.97 ± 0.06	-1.45 (fixed)	MIR+UV	Bell et al. 2007
0.6	1.06 ± 0.12	-2.68 ± 0.10	-1.45 (fixed)	MIR+UV	Bell et al. 2007
0.8	1.19 ± 0.15	-2.77 ± 0.15	-1.45 (fixed)	MIR+UV	Bell et al. 2007
0.8	1.10 ± 0.07	-2.47 ± 0.08	-1.56 ± 0.12	H α	Sobral et al. 2012
1.5	1.41 ± 0.06	-2.61 ± 0.09	-1.62 ± 0.25	H α	Sobral et al. 2012
2.2	1.71 ± 0.10	-2.73 ± 0.12	-1.57 ± 0.23	H α	Sobral et al. 2012
1.5	2.28 ± 0.15	-3.44 ± 0.23	-1.60 (fixed)	MIR	Magnelli et al. 2011
2.0	2.27 ± 0.15	-3.41 ± 0.26	-1.60 (fixed)	MIR	Magnelli et al. 2011
2.3	2.35 ± 0.15	-3.49 ± 0.24	-1.71 ± 0.08	MIR+UV	Reddy et al. 2008
3.8	1.54 ± 0.10	-2.97 ± 0.07	-1.60 ± 0.07	UV+ β	This work
5.0	1.36 ± 0.12	-3.12 ± 0.13	-1.50 ± 0.12	UV+ β	This work
5.9	1.07 ± 0.17	-2.97 ± 0.16	-1.57 ± 0.22	UV+ β	This work
6.8	1.00 ± 0.30	-3.20 ± 0.38	-1.96 ± 0.35	UV+ β	This work

Notes. These Schechter parameters are derived from the published H α , bolometric, and UV LFs in the literature using the Kennicutt (1998) relations. ^a It is unclear if there is a typographical error in the Schechter parameters provided by Bothwell et al. (2011). A simple integration of Bothwell et al. (2011) SFR function does not yield the quoted SFR density. However we quote the numbers as they are presented in Bothwell et al. (2011), converted to a Salpeter IMF with limits 0.1-125 M_{\odot} .

Table 2.4: Indicative SFRs over the redshift range $z \sim 2$ to $z \sim 8$

$\langle z \rangle$	$\log_{10} \frac{\text{SFR}^*}{M_{\odot} \text{ yr}^{-1}}$ (fixed ϕ^*) ^a	$\log_{10} \frac{\text{SFR}}{M_{\odot} \text{ yr}^{-1}}$ (fixed $n(> \text{SFR})$) ^b	probe	reference
2.0	2.04 ± 0.08	2.01 ± 0.30^c	MIR	Magnelli et al. 2011
2.2	1.89 ± 0.02	1.80 ± 0.30^c	H α	Sobral et al. 2012
2.3	2.08 ± 0.03	2.05 ± 0.30^c	MIR+UV	Reddy et al. 2008
3.8	1.58 ± 0.10	1.52 ± 0.30^c	UV+ β	This work
5.0	1.33 ± 0.11	1.27 ± 0.30^c	UV+ β	This work
5.9	1.09 ± 0.16	1.05 ± 0.30^c	UV+ β	This work
6.8	0.93 ± 0.29	0.86 ± 0.30^c	UV+ β	This work
8.0	0.61 ± 0.04	0.49 ± 0.30^c	UV	Oesch et al. 2012a

Notes. These Schechter parameters are derived from the published H α , bolometric luminosity and UV luminosity functions in the literature using the Kennicutt (1998) relations. ^a Fixed $\log_{10} \phi_{\text{SFR}}^* = -3.05$. See also Figure 2.4. ^b Fixed number density $n(> \text{SFR}) = 2 \cdot 10^{-4} \text{Mpc}^{-3}$ (Papovich et al., 2011). ^c Indicative errors from Papovich et al. (2011). If we use a Chabrier (2003) IMF as in Papovich et al. (2011) (instead of a Salpeter 1955 IMF with limits 0.1-125 M_{\odot}) the SFRs given here would be 0.2 dex lower.

References

- Arnouts, S., Schiminovich, D., Ilbert, O., et al. 2005, ApJ, 619, L43
- Bell, E. F., Zheng, X. Z., Papovich, C., Borch, A., Wolf, C., & Meisenheimer, K. 2007, ApJ, 663, 834
- Bothwell, M. S., Kenicutt, R. C., Johnson, B. D., Wu, Y., Lee, J. C., Dale, D., Engelbracht, C., Calzetti, D., & Skillman, E. 2011, MNRAS, 415, 1815
- Bouwens, R. J., Illingworth, G. D., Blakeslee, J. P., & Franx, M. 2006, ApJ, 653, 53
- Bouwens, R. J., Illingworth, G. D., Franx, M., & Ford, H. 2007, ApJ, 670, 928
- Bouwens, R. J., Illingworth, G. D., Franx, M., Chary, R.-R., Meurer, G. R., Conselice, C. J., Ford, H., Gialalisco, M., & van Dokkum, P. 2009, ApJ, 705, 936
- Bouwens, R. J., Illingworth, G. D., Labbe, I., Oesch, P. A., Trenti, M., Carollo, C. M., van Dokkum, P. G., Franx, M., Stiavelli, M., González, V., Magee, D., & Bradley, L. 2011a, Nature, 469, 504
- Bouwens, R. J., Illingworth, G. D., Oesch, P. A., Labbé, I., Trenti, M., van Dokkum, P., Franx, M., Stiavelli, M., Carollo, C. M., Magee, D., & Gonzalez, V. 2011b, ApJ, 737, 90
- Bouwens, R. J., Illingworth, G. D., Oesch, P. A., Franx, M., Labbe, I., Trenti, M., van Dokkum, P., Carollo, C. M., Gonzalez, V., & Magee, D. 2012, ApJ, 754, 83
- Bradley, L. D., Trenti, M., Oesch, P. A., et al. 2012, ApJ, submitted, arXiv:1204.3641
- Buat, V., Marcillac, D., Burgarella, D., et al. 2007, A&A, 469, 19
- Burgarella, D., Buat, V., & Iglesias-Páramo, J. 2005, MNRAS, 360, 1413
- Chabrier, G. 2003, PASP, 115, 763
- Castellano, M., Fontana, A., Grazian, A., et al. 2012, A&A, 540, A39
- Daddi, E., Dickinson, M., Morrison, G., Chary, R., Cimatti, A., Elbaz, D., Frayer, D., Renzini, A., Pope, A., Alexander, D. M., Bauer, F. E., Gialalisco, M., Huynh, M., Kurk, J., & Mignoli, M. 2007, ApJ, 670, 156
- Daddi, E., Dannerbauer, H., Stern, D., et al. 2009, ApJ, 694, 1517

- Dunlop, J. S., McLure, R. J., Robertson, B. E., et al. 2012, *MNRAS*, 420, 901
- Finkelstein, S. L., Papovich, C., Salmon, B., et al. 2011, *ApJ*, submitted, arXiv:1110.3785
- Grazian, A., Castellano, M., Koekemoer, A. M., et al. 2011, *A&A*, 532, A33
- Grogin, N. A., Kocevski, D. D., Faber, S. M., et al. 2011, *ApJS*, 197, 35
- Kennicutt, Jr., R. C. 1998, *ARA&A*, 36, 189
- Koekemoer, A. M., Faber, S. M., Ferguson, H. C., et al. 2011, *ApJS*, 197, 36
- Labbé, I., Franx, M., Rudnick, G., Schreiber, N. M. F., van Dokkum, P. G., Moorwood, A., Rix, H.-W., Röttgering, H., Trujillo, I., & van der Werf, P. 2007, *ApJ*, 665, 944
- Martin, D. C., Seibert, M., Buat, V., et al. 2005, *ApJ*, 619, L59
- Magdis, G. E., Elbaz, D., Daddi, E., Morrison, G. E., Dickinson, M., Rigopoulou, D., Gobat, R., & Hwang, H. S. 2010a, *ApJ*, 714, 1740
- Magdis, G. E., Elbaz, D., Hwang, H. S., et al. 2010, *MNRAS*, 409, 22
- Magnelli, B., Elbaz, D., Chary, R. R., Dickinson, M., Le Borgne, D., Frayer, D. T., & Willmer, C. N. A. 2011, *A&A*, 528, A35+
- Marchesini, D., Whitaker, K. E., Brammer, G., et al. 2010, *ApJ*, 725, 1277
- Meurer, G. R., Heckman, T. M., & Calzetti, D. 1999, *ApJ*, 521, 64
- Michałowski, M., Hjorth, J., & Watson, D. 2010, *A&A*, 514, A67
- Oesch, P. A., Bouwens, R. J., Carollo, C. M., Illingworth, G. D., Magee, D., Trenti, M., Stiavelli, M., Franx, M., Labbé, I., & van Dokkum, P. G. 2010, *ApJ*, 725, L150
- Oesch, P. A., Bouwens, R. J., Illingworth, G. D., et al. 2012a, *ApJ*, submitted, arXiv:1201.0755
- Oesch, P. A., Bouwens, R. J., Illingworth, G. D., Labbé, I., Trenti, M., Gonzalez, V., Carollo, C. M., Franx, M., van Dokkum, P. G., & Magee, D. 2012b, *ApJ*, 745, 110
- Ouchi, M., Shimasaku, K., Okamura, S., Furusawa, H., Kashikawa, N., Ota, K., Doi, M., Hamabe, M., Kimura, M., Komiyama, Y., Miyazaki, M., Miyazaki, S., Nakata, F., Sekiguchi, M., Yagi, M., & Yasuda, N. 2004, *ApJ*, 611, 660
- Overzier, R. A., Bouwens, R. J., Cross, N. J. G., Venemans, B. P., Miley, G. K., Zirm, A. W., Benítez, N., Blakeslee, J. P., Coe, D., Demarco, R., Ford, H. C., Homeier, N. L., Illingworth, G. D., Kurk, J. D., Martel, A. R., Mei, S., Oliveira, I., Röttgering, H. J. A., Tsvetanov, Z. I., & Zheng, W. 2008, *ApJ*, 673, 143
- Overzier, R. A., Heckman, T. M., Wang, J., Armus, L., Buat, V., Howell, J., Meurer, G., Seibert, M., Siana, B., Basu-Zych, A., Charlot, S., Gonçalves, T. S., Martin, D. C., Neill, J. D., Rich, R. M., Salim, S., & Schiminovich, D. 2011, *ApJ*, 726, L7+
- Papovich, C., Finkelstein, S. L., Ferguson, H. C., Lotz, J. M., & Giavalisco, M. 2011, *MNRAS*, 412, 1123
- Reddy, N., Dickinson, M., Elbaz, D., et al. 2012, *ApJ*, 744, 154
- Reddy, N. A., Erb, D. K., Pettini, M., Steidel, C. C., & Shapley, A. E. 2010, *ApJ*, 712, 1070
- Reddy, N. A. & Steidel, C. C. 2009, *ApJ*, 692, 778
- Reddy, N. A., Steidel, C. C., Pettini, M., et al. 2008, *ApJS*, 175, 48
- Reddy, N. A., Steidel, C. C., Fadda, D., Yan, L., Pettini, M., Shapley, A. E., Erb, D. K., & Adelberger, K. L. 2006, *ApJ*, 644, 792
- Salpeter, E. E. 1955, *ApJ*, 121, 161
- Schechter, P. 1976, *ApJ*, 203, 297
- Sobral, D., Smail, I., Best, P. N., et al. 2012, *MNRAS*, submitted, arXiv:1202.3436
- Steidel, C. C., Adelberger, K. L., Giavalisco, M., Dickinson, M., & Trenti, M., Bradley, L. D., Stiavelli, M., et al. 2011, *ApJ*, 727, L39
- Verma, A., Lehnert, M. D., Förster Schreiber, N. M., Bremer, M. N., & Douglas, L. 2007, *MNRAS*, 377, 1024
- Wilkins, S. M., Bunker, A. J., Stanway, E., Lorenzoni, S., & Caruana, J. 2011, *MNRAS*, 417, 717
- Wyder, T. K., Treyer, M. A., Milliard, B., et al. 2005, *ApJ*, 619, L15

3

Evidence for Ubiquitous High-EW Nebular Emission in $z \sim 7$ Galaxies: towards a Clean Measurement of the Specific Star Formation Rate Using a Sample of Bright, Magnified Galaxies

Growing observational evidence indicates that nebular line emission has a significant impact on the rest-frame optical fluxes of $z \sim 5 - 7$ galaxies. This line emission makes $z \sim 5 - 7$ galaxies appear more massive, with lower specific star formation rates (sSFR). However, corrections for this line emission have been difficult to perform reliably due to huge uncertainties on the strength of such emission at $z \gtrsim 5.5$. In this chapter, we present the most direct observational evidence yet for ubiquitous high-equivalent width (EW) [OIII]+H β line emission in Lyman-break galaxies at $z \sim 7$, while also presenting a strategy for an improved measurement of the sSFR at $z \sim 7$. We accomplish this through the selection of bright galaxies in the narrow redshift window $z \sim 6.6 - 7.0$ where the Spitzer/IRAC 4.5 micron flux provides a clean measurement of the stellar continuum light, in contrast with the 3.6 micron flux which is contaminated by the prominent [OIII]+H β lines. To ensure a high S/N for our IRAC flux measurements, we consider only the brightest ($H_{160} < 26$ mag) magnified galaxies we have identified behind galaxy clusters. Remarkably, the mean rest-frame optical color for our bright seven-source sample is very blue, $[3.6] - [4.5] = -0.9 \pm 0.3$. Such blue colors cannot be explained by the stellar continuum light and require that the rest-frame EW of [OIII]+H β is greater than 637\AA for the average source. The bluest four sources from our seven-source sample require an even more extreme EW of 1582\AA . We can also set a robust lower limit of $\gtrsim 4 \text{ Gyr}^{-1}$ on the sSFR of our sample based on the mean SED.

3.1 Introduction

In the last decade the evolution of galaxies at the earliest times has been predominantly mapped out by studying the rest-frame UV light in galaxies across cosmic time (e.g. Stanway et al., 2003; Bouwens et al., 2007; Bouwens et al., 2011; Lorenzoni et al., 2011; Oesch et al., 2012, 2013; Bradley et al., 2012b; Bowler et al., 2012; Schenker et al., 2013b). Despite great progress in this area, an equally important part of the story regards the build-up of mass in galaxies and the specific star formation rate (sSFR, i.e. the star formation rate divided by the stellar mass), which provide direct constraints on the growth time scale of individual sources (Stark et al., 2009; González et al., 2010). Typical sSFRs of star-forming galaxies at $z \sim 2$ ($M_* \sim 5 \times 10^9 M_\odot$) are $\sim 2 \text{ Gyr}^{-1}$, equivalent to a doubling time of $\sim 500 \text{ Myr}$.

Over the last few years, there has been a substantial improvement in our characterization of the sSFR in high-redshift galaxies and how it evolves. Initial observational studies found little evolution in the sSFR from $z \sim 2$ to higher redshift in apparent disagreement with theories of star formation fueled by cold accretion (Stark et al. 2009; Gonzalez et al. 2010; Labbe et al. 2010a,b). However, the effect of nebular emission lines (e.g., [OIII], [OII], $H\alpha$) that can contaminate the IRAC measurements of the stellar continuum light had not been taken into account (e.g. Schaerer & de Barros, 2009, 2010).

The effect of this emission on broadband IRAC measurements can be quite considerable. Extrapolating the $H\alpha$ EWs measured by Fumagalli et al. (2012) and Erb et al. (2006) to higher redshifts suggests $H\alpha$ EWs as large as 1000 \AA at $z \gtrsim 6$. This would indicate that $\sim 45\%$ of the flux in [4.5] is due to $H\alpha$ for galaxies at $z \sim 6 - 7$, while [OIII]+ $H\beta$ can contribute $\sim 55\%$ of the flux in [3.6]. Correcting for the effects of nebular emission, one can derive sSFRs which are plausibly consistent with theoretical expectations (Stark et al., 2013; González et al., 2012b; de Barros et al., 2012).

As the previous discussion indicates, it is essential in quantifying the sSFR at $z > 5$ to characterize the EWs of nebular emission lines and their impact on the IRAC photometry. Pioneering studies in the last two years have quantified the strength of nebular emission lines at $z \gtrsim 4$, through the measured flux offsets to the Spitzer/IRAC [3.6] and [4.5] bands. Shim et al. (2011) compare the [3.6] and [4.5] fluxes at $z \sim 4$ and show that the [3.6]–[4.5] color correlates with the star formation rate (SFR), implying that the source of the offset is likely due to the presence of $H\alpha$ emission lines. Stark et al. (2013) estimate the influence of $H\alpha$ on the [3.6] flux at $z \sim 3 - 4$ by comparing the color distribution of contaminated and uncontaminated spectroscopically confirmed galaxies (see also Schenker et al., 2013b) and extrapolating the observed emission line contamination to $z \sim 5 - 7$.

The first attempt to derive nebular line EWs for a large sample of Lyman-break galaxies at $z \gtrsim 5$ is presented in Labbe et al. (2012), based on a comparison of a stacked [3.6] and [4.5] flux measurement at $z \sim 8$ from the IRAC Ultra Deep Field (IUDF) program with similar flux measurements from a stacked sample at $z \sim 7$ (see also González et al. 2012a who make inferences about the EWs of nebular emission lines from the stacks of $z \sim 4 - 6$ galaxies). Estimates of the nebular-line EWs have also been made from direct fits to large number of spectroscopically-confirmed $z \sim 4 - 7$ galaxies (de Barros et al., 2012; Ono et al., 2012; Tilvi et al., 2013; Curtis-Lake et al., 2013)

Even making use of the above methods, the sSFR in $z \sim 6 - 8$ galaxies is still very uncertain. While one can certainly estimate the sSFR in this redshift range by utilizing an extrapolation of

the $H\alpha$ EWs found at $z \sim 4$ to higher redshift, extrapolations are inherently uncertain. Results on the sSFR at $z \sim 8$ (Labbe et al., 2012), though providing good leverage to constrain the redshift evolution, are limited by the extreme faintness of the individual galaxies whose redshift distribution is only approximately known. Finally, the typical $H\alpha$ EW in $z \sim 4$ galaxies used for sSFR estimates has been established primarily through sources which show $Ly\alpha$ in emission; however, it is unclear if those sources are representative of the broader $z \sim 4$ population (for more discussion see Schenker et al. 2013b).

To overcome these issues, here we make use of a new strategy for measuring the sSFRs and stellar masses for galaxies at very high redshifts, while simultaneously obtaining very good constraints on the EWs of [OIII]+ $H\beta$ line emission. Our plan is to take advantage of the considerable quantity of deep, wide-area observations over the 524-orbit, 25-cluster Cluster Lensing And Supernova survey with Hubble (CLASH) program (Postman et al., 2012) and other programs observing strong lensing clusters with deep multiband HST data. We select a small sample of bright, magnified galaxies for which we can obtain a clean measurement of the stellar continuum light from the deep IRAC observations over these clusters. One particularly fruitful redshift window in which we can obtain such clean measurements is the redshift window $z \sim 6.6 - 7.0$, where [4.5] is completely free of any emission lines. This should allow us to place much more robust constraints on the sSFR and the EW of nebular emission of star-forming galaxies at $z \sim 7$.

This chapter is organized as follows. In §3.2 we discuss our data set, our photometric procedure, and source selection. In §3.3 we present the properties of our selected $z \sim 7$ sample. We discuss the constraints we put on the EWs of $H\alpha$, $H\beta$ and [OIII] and the sSFR. We present a summary and discussion of our results in §3.4.

Throughout this chapter we adopt a Salpeter IMF with limits $0.1-100 M_{\odot}$ (Salpeter, 1955). For ease of comparison with previous studies we take $H_0 = 70 \text{ km s}^{-1} \text{ Mpc}^{-1}$, $\Omega_m = 0.3$ and $\Omega_{\Lambda} = 0.7$. Magnitudes are quoted in the AB system (Oke & Gunn, 1983)

3.2 Observations

3.2.1 Data

In selecting our small sample of bright, magnified $z \sim 7$ galaxies, we make use of the deep HST observations available over the first 23 clusters in the CLASH multi-cycle treasury program (GO #12101: PI Postman), Abell 1689 and Abell 1703 (GO #11802: PI Ford), the Bullet cluster (GO #11099: PI Bradac), and 9 clusters from the Kneib et al. (GO #11591) program. The CLASH cluster fields are each covered with 20-orbit HST observations spread over 16 bands using the Advanced Camera for Surveys (ACS: B_{435} , g_{475} , V_{606} , r_{625} , i_{775} , I_{814} , and z_{850}), Wide Field Camera WFC3/UVIS (UV_{225} , UV_{275} , U_{336} and U_{390}) and WFC3/IR instrument (Y_{105} , J_{110} , J_{125} , JH_{140} and H_{160}). Abell 1703 was covered with 22 orbits of ACS and WFC3/IR (B_{435} , g_{475} , V_{606} , r_{625} , i_{775} , z_{850} , J_{125} , H_{160}), Abell 1689 was covered with 54 orbits (B_{435} , r_{625} , i_{775} , I_{814} , z_{850} , J_{125} , J_{140} , H_{160}), the Bullet cluster was covered with 16 orbits (V_{606} , i_{775} , z_{850} , J_{110} , H_{160}) and clusters in the Kneib et al. program were covered with 6 orbits (I_{814} , J_{110} , H_{160}). HST mosaics were produced using the Mosaicdrizzle pipeline (see Koekemoer et al. 2011 for further details), and individual bands in the deep imaging data reach 5σ depths of 26.4-27.7 mag ($0.4''$ -diameter aperture).

Deep Spitzer/IRAC observations of our fields in the [3.6] and [4.5] bands were provided by the ICLASH (GO #80168; Bouwens et al. 2011), the Ultra-Deep IRAC imaging of Massive Lensing Galaxy Clusters (GO #20439; PI Egami) and the Spitzer IRAC Lensing Survey program (GO #60034; PI Egami). The typical exposure time per cluster was 3.5 to 5 hours per band, allowing us to reach 26.5 mag at 1 sigma. Reductions of the IRAC observations used in this chapter were performed with MOPEX (Makovoz & Khan, 2005).

3.2.2 Photometry and Selection

The photometry we obtain for sources in our cluster fields follows a similar procedure as described in Bouwens et al. (2012). In short, we run the SExtractor software (Bertin & Arnouts, 1996) in dual-image mode. The detection images are constructed from all bands redwards of the Lyman break (i.e. Y_{105} , J_{110} , J_{125} , JH_{140} and H_{160}). After PSF-matching the observations to the H_{160} -band PSF, colors are measured in Kron-like apertures and total magnitudes derived from $0.6''$ -diameter circular apertures.

Our initial source selection is based on the Lyman-break technique (Steidel et al., 1999), with the requirement that the source drops out in the I_{814} band. Specifically, our requirements for $z \sim 6 - 7$ sources are

$$(I_{814} - J_{110} > 0.7) \wedge (J_{110} - JH_{140} < 0.45).$$

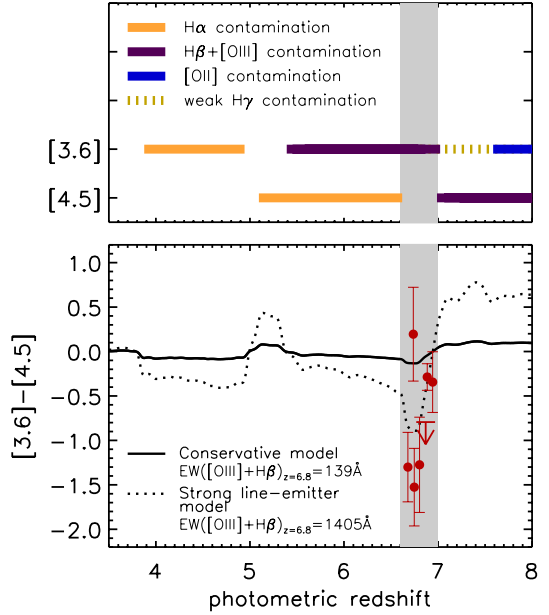
For sources in the CLASH program we require $H_{160} < 26$ AB, while we select sources to the brighter magnitude limit $H_{160} < 25$ AB in all other fields to ensure good photometric redshift constraints for all our sources. We also require sources to have either a non-detection in the V_{606} band ($< 2\sigma$) or to have a very strong Lyman break, i.e. $V_{606} - J_{125} > 2.5$. We require sources to be undetected in the optical χ^2 image (Bouwens et al., 2011) we construct from the observations bluewards of the r_{625} band. Finally we require the SExtractor stellarity parameter (equal to 0 and 1 for extended and point sources, respectively) in the J_{110} band be less than 0.92 to ensure that our selection is free of contamination by stars.

To identify those sources where we can obtain clean rest-frame optical stellar continuum, we also require that sources have a best-fit photometric redshift between $z = 6.6$ and 7.0 , as determined by the photometric redshift software EAZY (Brammer et al., 2008). All available HST photometry (i.e. 16 bands for CLASH clusters) is used in the redshift determinations. No use of the Spitzer/IRAC photometry is made in the photometric redshift determination to avoid coupling the selection of our sources to the [3.6]–[4.5] colors we will later measure. We use templates of young stellar populations with no Ly α emission.

Strong Ly α emission can systematically influence the photometric redshift estimate. However, we emphasize that any potential sources from outside our desired redshift interval that could be in our sample due to uncertainties in the photometric redshift estimate would only serve to increase the flux in the [4.5] band and redden the [3.6]–[4.5] color (i.e. due to contamination in the [4.5] band of H α at $z < 6.6$ and [OIII]+H β at $z > 7.0$). Correcting for this possible source of interlopers would result in higher EWs and sSFRs than in the case of no contamination. This reinforces the point we will make in §3.3 that the EWs we derive for the [OIII]+H β emission and the sSFRs are strong lower limits on the actual values.

Figure 3.1 shows the redshift range where we would expect the strongest emission lines, H α , H β , [OIII] $\lambda\lambda 4959, 5007$ and [OII] $\lambda 3727$, to impact the [3.6] and [4.5] fluxes. The top panel

Figure 3.1: The impact of emission lines on the [3.6] and [4.5] band fluxes and our strategy for deriving sSFRs and [OIII]+H β EWs from our $z \sim 7$ sample. *Top panel:* The redshift range over which strong nebular emission lines, H α , H β , [OIII] and [OII], will contaminate the [3.6] and [4.5] flux of galaxies. *Bottom panel:* The expected [3.6]–[4.5] colors as a function of redshift due to nebular emission lines. The solid and dotted lines show the expected color assuming relatively low EWs, i.e., $\text{EW}_0([\text{OIII}]+\text{H}\beta) \sim 140\text{\AA}$, and assuming strong evolution, i.e., $\text{EW}_0([\text{OIII}]+\text{H}\beta) \propto (1+z)^{1.8}\text{\AA}$ (Fumagalli et al., 2012), respectively, similar to the models considered in González et al. (2012b) and Stark et al. (2013). We select sources in the redshift range $z_{\text{phot}} = 6.6 - 7.0$, where [OIII] $\lambda\lambda 4959, 5007$ and H β are present in [3.6], while [4.5] receives no significant contamination from nebular emission lines, falling exactly in between the H α and [OIII] lines. The red solid circles and 1 sigma upper limit show the observed colors in our sample. We find that most sources show blue [3.6]–[4.5] colors, falling in the range between our two models. Four sources from our sample exhibit extremely blue rest-frame optical colors, with $[3.6] - [4.5] \lesssim -0.8$, indicating contamination of [OIII]+H β with a mean EW of $\gtrsim 1582\text{\AA}$ (see §3.3.2), even higher than using the Fumagalli et al. 2012 extrapolation indicated by the dotted line. Two sources at $z \sim 6.75$ have been offset by $\Delta z = 0.05$ for clarity.



indicates which lines fall in specific IRAC filters at a given redshift, while the bottom panel indicates the estimated [3.6]–[4.5] color offset due to the various emission lines. We select sources in the redshift range $z_{\text{phot}} = 6.6 - 7.0$, where we know that both [OIII] and H β fall in [3.6], while [4.5] falls exactly between [OIII] and H α where no significant emission lines are present (see for example Figure 3.2).

3.2.3 IRAC Photometry

Photometry of sources in the available Spitzer/IRAC data over our fields is challenging, due to blending with nearby sources from the broad PSF. We therefore use the automated cleaning procedure described in Labbé et al. (2010a,b). In short, we use the high-spatial resolution HST images as a template with which to model the positions and flux profiles of the foreground sources. The flux profiles of individual sources are convolved to match the IRAC PSF and then simultaneously fit to all sources within a region of $\sim 13''$ around the source. Flux from all the foreground galaxies is subtracted and photometry is performed in $2.5''$ -diameter circular apertures. We apply a factor of $\sim 2.0\times$ correction to account for the flux outside of the aperture, based on the radial light profile of the PSF. Figure 3.3 shows the cleaned IRAC images of our sample. Our photometric procedure fails when contaminating sources are either too close or bright. Sources with badly subtracted neighbors are excluded. In total, clean photometry is obtained for 78% of the sources,

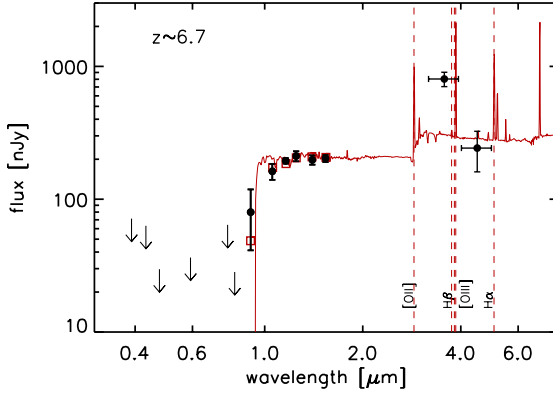


Figure 3.2: The observed HST+Spitzer fluxes (black circles) and 2σ upper limits (black arrows) with the best-fit spectrum (red) from our photometric redshift estimate (§3.2.2) for one $z \sim 7$ candidate rxj1347Z-7362045151 that exhibits a very blue [3.6]–[4.5] color. Because of the brightness of sources in our sample and the many HST filters with deep observations in the CLASH program, their photometric redshifts are well determined. This is important for establishing that our selected sources are likely in the target redshift window. The [3.6] and [4.5] bands that are shown are not used for the photo- z determination in order to avoid coupling the selection of our sources to the [3.6]–[4.5] colors.

resulting in 7 sources in our final selection (excluding only one source behind RXJ1347 and one source behind MACS1206 from our sample).

3.3 Results

Our search for bright ($H_{160} \lesssim 26$) LBGs in the redshift range $z \sim 6.6 - 7.0$ behind strong lensing clusters results in 9 candidates. One of the sources in our $z \sim 7$ sample was previously reported by Bradley et al. (2012a) based on a study of Abell 1703. For seven sources we obtain reasonably clean IRAC photometry, as shown in the postage stamps in Figure 3.3. The properties of the sources are summarized in Tables 3.1 and 3.2 and they range in H_{160} band magnitude from 24.3 to 25.7. Typical magnification factors, μ , for our sources are $\sim 2 - 9$, using the lensing models of Zitrin et al. (2010, 2011) and Zitrin et al. (in prep). Though the magnification of the sources improves the S/N of our measurements, we stress that measurements of emission line EWs and sSFRs only depend on the colors of the SED and therefore are not impacted by uncertainties in the model magnification factors.

3.3.1 [3.6]–[4.5] color distribution and nebular emission lines

Our selection of sources in the redshift range $z \sim 6.6 - 7.0$ provides us with the valuable opportunity to establish the typical EW of the nebular emission lines in $z \gtrsim 6$ sources through a comparison of the flux in [3.6] and [4.5]. For a given EW we calculate the [3.6]–[4.5] color by assuming that the observed flux in one filter can be approximated by

$$f_{\nu, \text{obs}} = f_{\nu, \text{continuum}} \cdot x_{\text{EW}} \quad (3.1)$$

$$x_{\text{EW}} = \left(1 + \sum_{\text{lines}, i} \frac{\text{EW}_{0,i} \cdot (1+z) \cdot R(\lambda_{\text{obs},i})}{\lambda_{\text{obs},i} \int R(\lambda)/\lambda d\lambda} \right)$$

Here, $f_{\nu, \text{continuum}}$ is the intrinsic flux of the stellar continuum, while $f_{\nu, \text{obs}}$ is the observed flux of the filter. Furthermore, $\lambda_{\text{obs},i}$ is the observed wavelength of the line and $R(\lambda)$ is the response

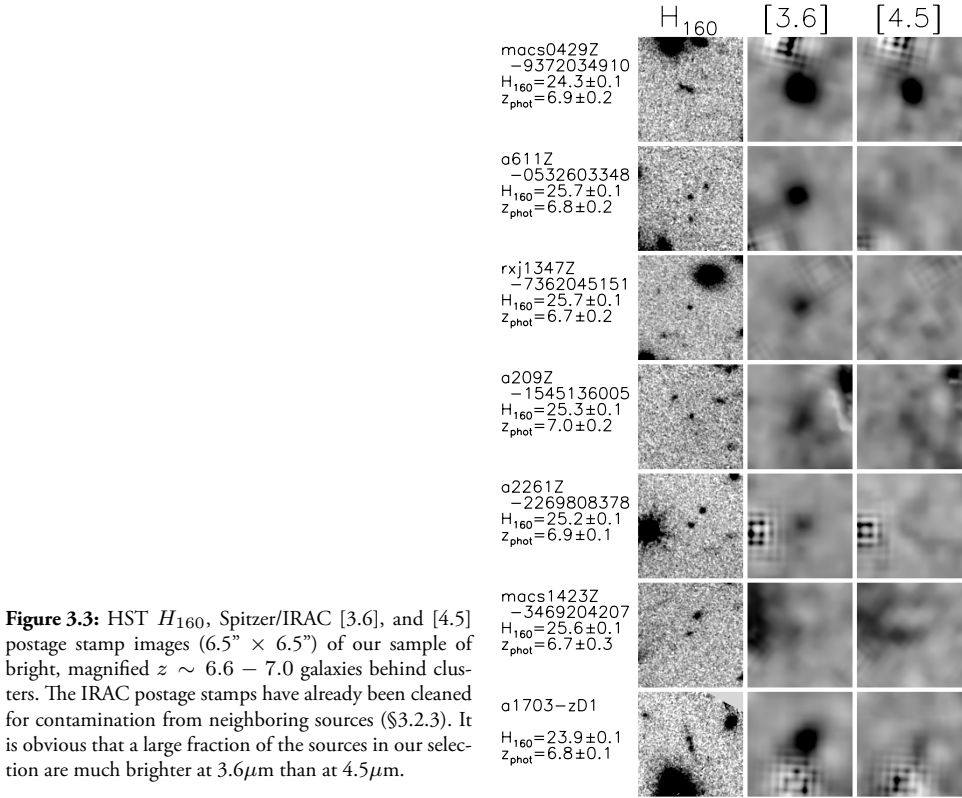


Figure 3.3: HST H_{160} , Spitzer/IRAC [3.6], and [4.5] postage stamp images ($6.5'' \times 6.5''$) of our sample of bright, magnified $z \sim 6.6 - 7.0$ galaxies behind clusters. The IRAC postage stamps have already been cleaned for contamination from neighboring sources (§3.2.3). It is obvious that a large fraction of the sources in our selection are much brighter at $3.6\mu\text{m}$ than at $4.5\mu\text{m}$.

curve of the filter. We sum over all nebular emission lines listed in Anders & Fritze-v. Alvensleben (2003), as well as the hydrogen Balmer lines. We assume fixed flux-ratios between the emission lines based on the tabulated values in Anders & Fritze-v. Alvensleben (2003) for $0.2Z_{\odot}$ metallicity and assuming case B recombination. The observed [3.6]–[4.5] color then simplifies to

$$[3.6] - [4.5] = ([3.6] - [4.5])_{\text{continuum}} - 2.5 \cdot \log \left(\frac{x_{\text{EW},3.6}}{x_{\text{EW},4.5}} \right). \quad (3.2)$$

LBGs at high redshift are expected to exhibit flat optical stellar continuum, based on stellar population synthesis models. In these models young galaxies with typical ages between 50–200Myr and low dust extinction, e.g. $E(B-V) \sim 0.1$, will have a $([3.6] - [4.5])_{\text{continuum}}$ color of $\sim 0 \pm 0.1$ mag. However, extremely young (i.e. $\sim 3 \times 10^6$ yr), dust-free galaxies can exhibit $([3.6] - [4.5])_{\text{continuum}}$ colors as blue as ~ -0.4 . To be conservative, we will adopt this for the color of the underlying stellar continuum, and assume that any bluer [3.6]–[4.5] color arises from the impact of emission lines to establish robust lower limits.

In the bottom panel of Figure 3.1 the dotted line shows a prediction of the observed optical color due to emission lines, using Equations 3.1 and 3.2 and assuming a flat continuum, for a model of strongly increasing rest-frame emission line EWs as a function of redshift (dotted line), with $\text{EW}_0([\text{OIII}] + \text{H}\beta) \propto (1+z)^{1.8} \text{\AA}$, based on the evolution in $\text{EW}_0(\text{H}\alpha)$ found by Fumagalli et al. (2012) for star forming galaxies over the redshift range $0 \lesssim z \lesssim 2$. The red points

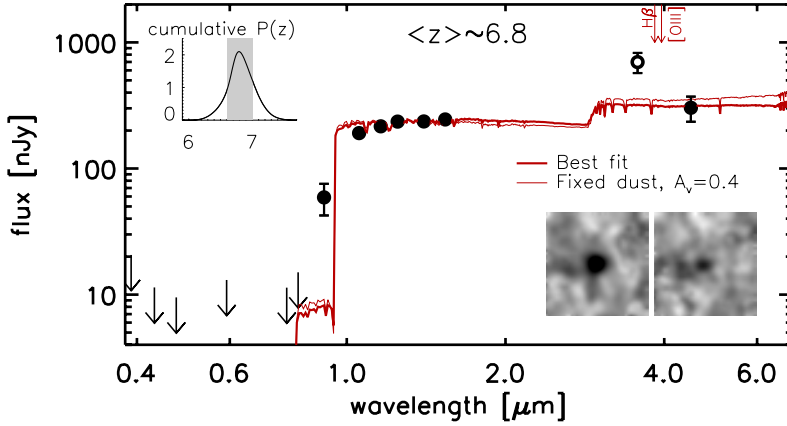


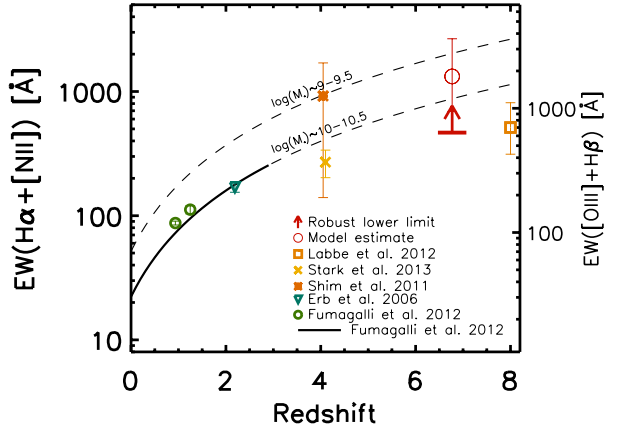
Figure 3.4: The mean-stacked SED of our $z \sim 6.6 - 7.0$ sample. The inset images on the bottom right show the stacked photometry of the [3.6] (left) and [4.5] (right) bands. The mean [3.6]–[4.5] color for our sample is ~ -0.9 and indicates significant line contamination for the typical $z \sim 7$ galaxy. The top left inset panel indicates the sum of the redshift probability distributions for the sources in our sample. A small fraction of the sources in our photometric redshift selection are expected to lie outside the target range $z \sim 6.6 - 7.0$ (due to redshift uncertainties). Any such contamination would make the [3.6]–[4.5] colors redder due to the contribution of $H\alpha$ (at $z < 6.6$) or $[OIII]+H\beta$ (at $z > 7$) to the [4.5] flux. The thick red line indicates the best fit SED to our observed photometry, excluding the [3.6] flux from the fit. The thin red line indicates a best fit SED when the dust content is fixed to $A_V = 0.38$, similar to the assumptions used in Bouwens et al. (2012), Stark et al. (2013), González et al. (2012b) and Labbé et al. (2012).

in Figure 3.1 show the observed colors for our sample. Most of our sources show quite blue [3.6]–[4.5] colors and essentially all of them are bluer than that expected based on a conservative model of constant rest-frame EW (solid black line: i.e. assuming no evolution from $z \sim 2$ where $EW_0([OIII]+H\beta) \sim 140\text{\AA}$, derived from the $H\alpha$ EWs found by Erb et al. 2006). Interestingly enough, three of the sources from our sample have [3.6]–[4.5] colors even bluer than expected at $z \sim 6.7 - 6.8$ for the model from Fumagalli et al. (2012) with $EW_0(H\alpha) \propto (1+z)^{1.8}\text{\AA}$. Four of the sources have [3.6]–[4.5] colors bluer than -0.8 . Since we would only expect galaxies to show such extreme [3.6]–[4.5] colors in the narrow redshift range $z \sim 6.6 - 7.0$, this provides us with additional confidence that our selection is effective at identifying sources in the desired redshift range.

3.3.2 Inferred $[OIII]+H\beta$ EWs of $z \sim 7$ galaxies from the mean SED

To obtain our best measurement of the [4.5] flux and hence stellar continuum light from $z \sim 7$ galaxies, we construct a mean SED that can be directly compared to studies of the mean rest-frame optical properties of $z \gtrsim 4$ galaxies in the literature (e.g. González et al., 2012a,b; Stark et al., 2013). We use a mean stack of the clean [3.6] and [4.5] images after dividing by the observed rest-frame UV luminosity (the geometric mean of the J_{125} , JH_{140} and H_{160} luminosities). We measure the flux in a $2.5''$ diameter aperture on the stacked image and apply an aperture correction measured from the PSF images ($\sim 2.0\times$). Additionally, we use the mean of the individual measurements of the HST bands, after dividing by the rest-frame UV-luminosity. The mean SED of our stacked $z \sim 6.8$ sample is shown in Figure 3.4. Errors are obtained through bootstrap

Figure 3.5: The constraint on the evolution of [OIII]+H β EWs (and equivalent H α EWs) from our stacking analysis and references from the literature (Erb et al., 2006; Shim et al., 2011; Fumagalli et al., 2012; Stark et al., 2013; Labbe et al., 2012). The robust lower limit (red arrow) assumes all sources are at $z = 6.76$ where the [3.6]–[4.5] color is expected to be the most extreme for a given set of EWs and that the underlying stellar continuum has a [3.6]–[4.5] color of ~ -0.4 (which would only be the case if all galaxies have an age of $\sim 3 \times 10^6$ yr). Any bluer [3.6]–[4.5] color would therefore arise from the impact of the [OIII]+H β emission lines on the [3.6] flux. For the model estimate (red open circle) we model the effects of a broader redshift distribution as described in §3.3.2. For comparison with lower redshift estimates we have converted our EWs to $\text{EW}(\text{H}\alpha + [\text{NII}])$ using the conversion factors from Anders & Fritze-v. Alvensleben (2003). The high EW inferred from our mean stacked sample indicates significantly stronger emission lines than observed at redshift $z \sim 0 - 2$, possibly consistent with an extrapolation of the trends with redshift and mass found by Fumagalli et al. (2012, indicated by the dashed black lines).



resampling.

We use the stacked detections in the IRAC bands to evaluate the mean contribution of the emission lines. From the mean [3.6]–[4.5] color we estimate the [OIII]+H β EW by assuming that our entire sample is at $z = 6.76$, where we expect the most extreme colors because [4.5] is completely free of emission lines, while [3.6] is contaminated by both the [OIII] doublet and H β . In practice, this results in an underestimate of the intrinsic line strength, since we know that the [OIII] lines start to drop out of [3.6] at $z \sim 6.9 - 7.0$. Therefore we expect a less extreme [3.6]–[4.5] color for a given mean EW at $z \sim 6.9 - 7.0$ than at $z \sim 6.7 - 6.8$. It is also possible that due to uncertainties in the photometric redshifts, sources outside of our target redshift range have been included in our selection and therefore the measurement of the [4.5] flux is contaminated by either H α ($z < 6.6$) or [OIII] ($z > 7$). This would also make the mean [3.6]–[4.5] color redder and accordingly make the emission lines appear to be less extreme.

The mean observed [3.6]–[4.5] color for our sample is -0.9 ± 0.3 (error obtained through bootstrap resampling). In the most conservative estimate, we assume that the underlying stellar continuum exhibits a [3.6]–[4.5] color of ~ -0.4 and therefore the [OIII] and H β are responsible for a color of [3.6] – [4.5] ~ -0.5 , which would give a robust lower limit of $\text{EW}_0([\text{OIII}]+\text{H}\beta) \gtrsim 637\text{\AA}$ for the mean $z \sim 7$ galaxy distribution. The [OIII]+H β EW we estimate here is equivalent to $\text{EW}_0(\text{H}\alpha + [\text{NII}]) \gtrsim 495\text{\AA}$ adopting the tabulated values from Anders & Fritze-v. Alvensleben (2003) for $0.2Z_{\odot}$ metallicity and assuming case B recombination.

The mean observed $[3.6] - [4.5]$ color for our four bluest sources is -1.4 ± 0.4 . If we assume again a very blue underlying continuum (i.e., -0.4), line emission would be responsible for a color of $[3.6] - [4.5] \sim -1.0$, consistent with a robust lower limit of $\text{EW}_0([\text{OIII}] + \text{H}\beta) \gtrsim 1582 \text{ \AA}$ for these sources. The individual lower limits for these blue sources are listed in Table 3.2. While the four bluest sources in our sample are, given their extreme colors, almost certainly at a redshift $z \sim 6.7 - 6.8$, it is unclear if the three other sources are less extreme due to a lower $[\text{OIII}] + \text{H}\beta$ EW or simply because they lie in a different redshift range (i.e. $z \gtrsim 6.9$ or close to $z \sim 6.6$), where for a given EW we expect somewhat redder colors.

To obtain a good estimate of the EW, detailed knowledge of the redshift distribution and the underlying stellar continuum color is required. Given our lack of deep spectroscopy for our sample we will make some reasonable assumptions to obtain a model estimate of the rest-frame EW of our sample. We assume that the redshift probability distribution of our sources is given by the sum of the probability distributions obtained from our photometric redshift code, corrected for the fact that galaxies are more difficult to observe at higher redshift scaling roughly as $\frac{d \log \phi}{dz} = 0.3$ (Bouwens et al., 2012b) and assuming no sources are outside our desired redshift range $z \sim 6.6 - 7.0$. We use this redshift probability distribution in our sample to estimate the expected $[3.6] - [4.5]$ color distribution, for a given mean $\text{EW}_0([\text{OIII}] + \text{H}\beta)$ and 0.3 dex scatter around the mean. We assume the underlying continuum color is -0.25 , as would be expected for a galaxy age of $\sim 10 \text{ Myr}$. We randomly draw sources from the distribution and calculate the 68% likelihood of finding a mean $< [3.6] - [4.5] >$ color given a total of seven observed sources and the observed photometric errors. Based on this modeling, the observed $[3.6] - [4.5] \sim -0.9 \text{ mag}$ color is consistent with a possible $\text{EW}_0([\text{OIII}] + \text{H}\beta)$ EW of $\sim 1806_{-863}^{+1826} \text{ \AA}$. This is equivalent to $\text{EW}_0(\text{H}\alpha + [\text{NII}]) \sim 1323_{-632}^{+1338} \text{ \AA}$, adopting the same conversion factor from Anders & Fritzev. Alvensleben (2003) assumed above.

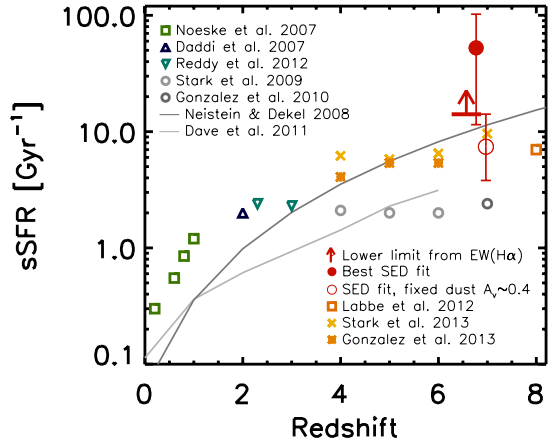
The modeling we perform above indicates that the true $\text{EW}_0([\text{OIII}] + \text{H}\beta)$ may be $\sim 2 - 3 \times$ larger than our robust lower limit of 637 \AA . Figure 3.5 compares our results with other determinations from the literature (Erb et al., 2006; Shim et al., 2011; Fumagalli et al., 2012; Stark et al., 2013; Labbe et al., 2012). The solid and dashed lines in Figure 3.5 show the expected evolution of the $\text{H}\alpha + [\text{NII}]$ EWs extrapolating the evolution found in Fumagalli et al. (2012) at $z \sim 0 - 2$. We note however that a direct comparison is difficult to make since the Fumagalli et al. (2012) relation was derived for galaxies in the mass range $M_* = 10^{10} - 10^{10.5} M_\odot$, while we are probing galaxies in the mass range $10^9 - 10^{9.5} M_\odot$. For reference we show the possible evolution of galaxies $M_* = 10^9 - 10^{9.5} M_\odot$ (top dashed line), using the same scaling with redshift $\text{EW}_0(\text{H}\alpha + [\text{NII}]) \propto (1 + z)^{1.8} \text{ \AA}$ but extrapolating the normalization to lower masses, based on the mass trend in the SDSS-DR7 data derived in Fumagalli et al. (2012).

In general, the EWs we infer are in good agreement with extrapolations from previous results at lower redshift. However our results are based on a UV-selected sample, which could yield different results from a mass complete sample. It is clear nonetheless, that our EWs estimates strongly support the high EWs used by Stark et al. (2013) and González et al. (2012b) in correcting the SEDs of $z \sim 5 - 7$ samples to derive higher values of the sSFRs.

3.3.3 Specific star formation rates

The redshift range where we select galaxies is the only redshift window at $z \gtrsim 5$ where we can probe the rest-frame stellar continuum light in an uncontaminated fashion, using the $[4.5]$ IRAC

Figure 3.6: The evolution of the sSFR as a function of redshift, based on the fitted SED to our stacked photometry, excluding the [3.6] flux from the fit. Error bars are the 68% confidence interval, based on the photometric uncertainties. The red filled circle indicates the best fit using the assumptions described in §3.3.3, leaving dust as a free parameter. The red open circle indicates a fit where the dust content is fixed at $A_V = 0.38 \pm 0.16$. We also show a lower limit (red arrow) on the sSFR we derive from the EW of [OIII]+H β , by converting to H α assuming the line ratios from Anders & Fritze-v. Alvensleben (2003). For context, we also include many previous sSFR results from the literature (Noeske et al., 2007; Daddi et al., 2007; Stark et al., 2009, 2013; González et al., 2010, 2012b; Reddy et al., 2012; Labbe et al., 2012). Our results indicate possible strong evolution in the sSFRs from redshift $z \sim 2$ to $z \sim 7$, consistent with other recent results based on an extrapolation of the $z \sim 4$ H α EW distribution (Stark et al., 2013; González et al., 2012b) or for single $z \sim 7$ galaxies (e.g. Ono et al., 2012; Tilvi et al., 2013; Ouchi et al., 2013). Our results are also in agreement with theoretical predictions (e.g., Neistein & Dekel 2008 [dark grey line] and Davé et al. 2011 [light grey line]).



band (see figure 3.1). This allows us to estimate the sSFR, with minimal contamination from emission lines.

Due to the low signal-to-noise of the uncontaminated [4.5] band, we can set only weak constraints on the specific star formation rates of the individual galaxies (see Table 3.2). To optimize the S/N we perform stellar population modeling of our stacked photometry, leaving out the [3.6] measurement. The modeling was performed with FAST (Kriek et al., 2009), using the Bruzual & Charlot (2003, hereafter BC03) stellar populations synthesis models. We use a Salpeter (1955) IMF with limits $0.1-100 M_{\odot}$ and a Calzetti et al. (2000) dust-law. We consider ages between 10 Myr and the age of the universe at $z \sim 6.8$ and dust extinction between $A_V = 0 - 2$. A constant star formation history and subsolar metallicity ($0.2Z_{\odot}$) is assumed. For the mean stack we fix the redshift to the median of the photometric redshifts, at $z = 6.77$.

Given this freedom of parameters the mean SED is best described by a fairly young galaxy (age $\lesssim 100$ Myr) and reasonable dust ($A_V \sim 0.7$) in order to fit both the small Balmer break ($H_{160} - [4.5] \sim 0.2$) and moderately red UV-continuum slope ($\beta \sim -1.9$), resulting in a notably high sSFR of $52^{+50}_{-41} \text{ Gyr}^{-1}$ (see the SED in Figure 3.4). However, the interpretation of this result is not straightforward. First of all, we have only the [4.5] band in the rest-frame optical to break the age-dust degeneracy. Given our modest sample there is still a range of models that can fit the data well. A possibly more insightful answer is obtained when we fix the dust to the expected value derived from the typical spread of UV-continuum slopes and the Meurer et al. (1999) law (e.g. Bouwens et al., 2012) similar to the assumptions made in Bouwens et al. (2012), Stark et al. (2013), González et al. (2012b) and Labbe et al. (2012). This results in a dust content of $A_V = 0.38 \pm 0.16$ using the latest numbers from Bouwens et al. (2014a). We fix the dust

Table 3.1: $z \sim 6.6 - 7.0$ candidates included in this work

ID ^a	RA	Dec	z_{phot}	μ^b	M_{UV}^c
macs0429Z-9372034910	04:29:37.20	-2:53:49.10	6.9 ± 0.2	2.5 ± 0.2	-21.6 ± 0.1
a611Z-0532603348	08:00:53.26	36:03:34.8	6.7 ± 0.2	1.8 ± 0.1	-20.5 ± 0.1
rxj1347Z-7362045151	13:47:36.20	-11:45:15.1	6.7 ± 0.2	2.7 ± 0.2	-20.1 ± 0.1
a209Z-1545136005	01:31:54.51	-13:36:00.5	6.9 ± 0.2	1.2 ± 0.0	-21.4 ± 0.1
a2261Z-2269808378 ^d	17:22:26.99	32:08:37.8	6.9 ± 0.1	5.6 ± 1.7	-19.9 ± 0.3
macs1423Z-3469204207	14:23:46.92	24:04:20.7	6.7 ± 0.3	4.7 ± 1.0	-19.6 ± 0.3
a1703-zD1 ^e	13:14:59.41	51:50:00.8	6.8 ± 0.1	9.0 ± 4.5	-20.6 ± 0.5

^aTwo sources from our initial Lyman Break selection displayed bad residuals after subtraction of the closest neighbors and were therefore excluded from the analysis. The two rejected sources are RXJ13471-7332751567 (RA 13:47:33.27, Dec -11:45:15.67) and MACS1206Z-6100148441 (RA 12:06:10.01, Dec -8:48:44.1).

^bThe lens models for RXJ1347, MACS0429, Abell 611 and Abell 209 are made with an improved version of the method described in Zitrin et al. (2009) and will be published in Zitrin et al. (in prep). The model for Abell 2261 is described Coe et al. (2012). The model for MACS1423 is described in Zitrin et al. (2011), but here we use a refined model (the CLASH collaboration, in prep). The model for Abell 1703 is described in Zitrin et al. (2010). Errors on the magnification factors are typical errors at a given μ , calculated using the modeled uncertainties of Abell 383, Abell 611, MS2137 and MACS1423 (Zitrin et al., in prep).

^cThe intrinsic UV magnitude is derived from the H-band magnitude, corrected for the magnification, μ . The quoted uncertainty includes the estimated uncertainty in μ .

^dWhile this source is very compact, our size measurements indicate that it is slightly extended.

^ePreviously reported in Bradley et al. (2012a)

content to $A_V = [0.22, 0.38, 0.54]$ in turn. The fit for $A_V = 0.38$ is shown with the thin red line in Figure 3.4. We obtain a sSFR of $7_{-3}^{+7} \text{ Gyr}^{-1}$. Given that the reduced χ^2 with the lowest dust content $A_V = 0.22$ is only ~ 1.3 times higher than for our best fit ($\chi^2 = 1.79$ versus $\chi^2 = 1.33$) we assume a conservative lower limit of the sSFR of $\gtrsim 4 \text{ Gyr}^{-1}$.

Alternatively, we can estimate the sSFR of our $z \sim 7$ sample from the [OIII]+H β EWs we infer, by converting to H α EW assuming same line ratios from Anders & Fritze-v. Alvensleben (2003) as described in §3.3.2. We use the Kennicutt (1998) relation to convert H α luminosity to star formation rate and we use BC03 models (assuming no dust) to convert the rest-frame optical continuum light to stellar mass. Using these assumption we obtain a lower limit on the sSFR for our seven source sample and the bluest four sources of $\sim 14 \text{ Gyr}^{-1}$ and $\sim 130 \text{ Gyr}^{-1}$ respectively, based on the robust lower limits on the [OIII]+H β EW derived in §3.3.2.

Comparing with direct constraints at $z \sim 2$ we estimate $\gtrsim 2\times$ evolution in the sSFR over this redshift range, in good agreement with estimates at $z \sim 7$ based on a few spectroscopically confirmed sources (Ono et al., 2012; Tilvi et al., 2013) and extrapolating the H α EWs from lower redshifts (Yabe et al., 2009; Stark et al., 2013; González et al., 2012b). Our derived constraint is also in agreement with theoretical models that predict the sSFR to follow the specific infall rate of baryonic matter (e.g. Neistein & Dekel, 2008).

Table 3.2: Properties of the mean stack and the individual sources in our sample of $z \sim 6.6 - 7.0$ galaxies

ID	H_{160}	$H_{160} - [4.5]$	$[3.6] - [4.5]$	β^a	$\text{EW}_{[\text{OIII}]+\text{H}\beta}^b$	$\log(\frac{\text{sSFR}}{yr^{-1}})$
macs0429Z-9372034910	24.3 ± 0.1	0.7 ± 0.1	-0.3 ± 0.1	-1.4 ± 0.4	—	$-7.8^{+0.8}_{-0.7}$
a611Z-0532603348	25.7 ± 0.1	0.3 ± 0.4	-1.5 ± 0.4	-1.5 ± 0.5	> 1905	$> -8.1^c$
rxj1347Z-7362045151	25.7 ± 0.1	0.2 ± 0.4	-1.3 ± 0.4	-2.2 ± 0.5	> 1363	$-7.6^{+0.6}_{-1.0}$
a209Z-1545136005	25.3 ± 0.1	1.0 ± 0.3	-0.3 ± 0.3	-2.7 ± 0.6	—	$< -8.1^d$
a2261Z-2269808378	25.2 ± 0.1	< 0.0	< -0.8	-2.0 ± 0.3	> 1043	$> -7.8^c$
macs1423Z-3469204207	25.6 ± 0.1	1.0 ± 0.3	0.2 ± 0.5	-1.2 ± 0.8	—	$< -7.0^d$
a1703-zD1	23.9 ± 0.1	-1.0 ± 0.4	-1.3 ± 0.5	-1.4 ± 0.3	> 1304	$-6.4^{+0.4}_{-0.1}$
Mean stack	25.5 ± 0.1	0.2 ± 0.2	-0.9 ± 0.3	-1.9 ± 0.3	> 637	$-7.3^{+0.3}_{-0.7}$

Upper and lower limits are 1σ

^aThe UV-continuum slope β is estimated using a log-linear fit to the J_{125} , JH_{140} and H_{160} fluxes.

^bEstimates (in \AA) are lower limits assuming the bluest possible continuum color of $[3.6] - [4.5] = -0.4$, see §3.3.1.

^cWe can only put a lower limit on the specific star formation rate of this source due to the blue $H_{160} - [4.5]$ color in combination with the large errorbar on the $[4.5]$ flux, i.e. the fit of the stellar population is consistent with an arbitrarily young age.

^dWe can only put an upper limit on the specific star formation rate of this source with our data. The lower limit is set by the age of the universe ($\sim 1.3 \text{ Gyr}^{-1}$ at $z \sim 6.8$).

3.4 Summary and discussion

In this chapter, we present the strongest direct evidence yet for very high $[\text{OIII}]+\text{H}\beta$ EWs in the $z \sim 7$ galaxy population. We also simultaneously explore a strategy for obtaining a clean measurement of the sSFR at $z \sim 7$ based on the stellar continuum flux measured in the $[4.5]$ micron band – which is largely free of contamination from the strongest nebular lines. Nebular emission lines ($[\text{OIII}]$, $\text{H}\alpha$, $\text{H}\beta$) and the extreme faintness of $z \gtrsim 5.5$ galaxies make it extremely challenging to establish the stellar masses and sSFRs of the typical galaxy at high redshift.

To overcome these issues, we have isolated a small sample of nine bright ($H_{160} < 26 \text{ mag}$), magnified galaxies in the redshift range $z \sim 6.6 - 7.0$ from CLASH and other programs, seven of which we can perform high-quality IRAC photometry. Galaxies with photometric redshifts in the range $z \sim 6.6 - 7.0$ are useful, since there the $[4.5]$ band from Spitzer/IRAC provides us with a clean measurement of the stellar continuum flux from galaxies in the rest-frame optical, free of contamination from dominant nebular emission lines (Figure 3.1 and Figure 3.2).

For the mean source in our sample, we find that we can set a robust lower limit on the rest-frame EW of $[\text{OIII}]+\text{H}\beta$ of 637\AA . For this lower limit, we adopt the bluest conceivable $[3.6] - [4.5]$ colors for the stellar continuum and assume that all sources in our sample are at $z = 6.76$ where a given $[\text{OIII}]+\text{H}\beta$ EW would produce the most extreme $[3.6] - [4.5]$ color. Use of a more realistic redshift distribution for our sample, i.e., consistent with the photometric redshift estimates and not assuming that all sources are at $z = 6.76$, suggest that these lower limits may underestimate the true EWs by a factors of $\sim 2\times$.

The four bluest sources in our selection (58% of our sample) show evidence for even more extreme line emission, with $[3.6] - [4.5] \lesssim -0.8$. For these 4 sources, we can set a robust lower limit of 1582\AA on the rest-frame EW in $[\text{OIII}]+\text{H}\beta$.

Extreme line emission with EWs greater than 1000\AA has been found at lower redshift in low

mass galaxies (van der Wel et al., 2011; Atek et al., 2011). Our results are consistent with the idea that extreme line emission may be present in the typical star-forming galaxy at $z \sim 7$.

Furthermore, our [4.5] stack results imply a firm lower limit on the sSFR of $\sim 4 \text{ Gyr}^{-1}$ for star-forming galaxies at $z \sim 7$. If any sources from our $z \sim 6.6 - 7.0$ photometric redshift sample lie at lower or higher redshifts than this, it would imply even lower [4.5] micron fluxes for the stack and hence higher sSFRs. Compared with sSFRs measurements at $z \sim 2$ (Daddi et al., 2007; Reddy et al., 2012), this implies at least a $\gtrsim 2\times$ evolution in the sSFR over the redshift range $z \sim 2$ to $z \sim 7$. Similar to a few other spectroscopically confirmed $z \sim 7$ galaxies in the literature (Ono et al., 2012; Tilvi et al., 2013), this provides strong evidence that the sSFRs at $z \sim 7$ are high.

We expect improvement in these results through the measurement of spectroscopic redshifts for our sample from deep spectroscopy. This should allow us to obtain an even cleaner selection of $z \sim 6.6 - 7.0$ galaxies from which to quantify the emission line contamination and sSFRs. Follow-up observations of our sample are facilitated by the fact that these candidates are typically ~ 1 magnitude brighter than similar candidates found in the field, making these efforts quite feasible in terms of the telescope time required.

Moreover, our bright $z \sim 7$ sample is small and the S/N we have per source is still modest. Increases in sample size can come from shallow surveys over a larger numbers of clusters, such as those available from recent snapshot programs. S/N increases will come from very deep HST+Spitzer observations being taken by the Frontier Fields program and the SURF'S Up program (Bradac et al., 2012).

Acknowledgements

We thank Jeff Cooke, Rob Crain, Eichii Egami, Andrea Ferrara, Marijn Franx, Max Pettini, Norbert Pirzkal and Vivienne Wild for interesting conversations. Eichii Egami independently discovered the same extreme [3.6]–[4.5] colors in at least one of the sources from the present sample. We thank Pascal Oesch for useful feedback on our manuscript. We thank the anonymous referee for providing excellent feedback. We acknowledge support from ERC grant HIGHZ #227749, an NWO vrij competitie grant, and the NASA grant for the CLASH MCT program. Support for AZ is provided by NASA through Hubble Fellowship grant #HST-HF-51334.01-A awarded by STScI, which is operated by the Association of Universities for Research in Astronomy, Inc., for NASA, under contract NAS 5-26555. Part of this work was also supported by contract research “Internationale Spitzenforschung II/2-6” of the Baden Württemberg Stiftung. The work of LAM was carried out at Jet Propulsion Laboratory, California Institute of Technology, under a contract with NASA.

References

- Anders, P., & Fritze-v. Alvensleben, U. 2003, *A&A*, 401, 1063
- Atek, H., Siana, B., Scarlata, C., et al. 2011, *ApJ*, 743, 121
- Bertin, E., & Arnouts, S. 1996, *A&AS*, 117, 393
- Bouwens, R. J., Illingworth, G. D., Franx, M., et al. 2009, *ApJ*, 705, 936
- Bouwens, R. J., Illingworth, G. D., Franx, M., & Ford, H. 2007, *ApJ*, 670, 928
- Bouwens, R. J., Illingworth, G. D., Oesch, P. A., et al. 2011, *ApJ*, 737, 90
- Bouwens, R., Zheng, W., Moustakas, L., et al. 2011, *Spitzer Proposal*, 80168
- Bouwens, R. J., Illingworth, G. D., Oesch, P. A., et al. 2012, *ApJ*, 754, 83
- Bouwens, R., Bradley, L., Zitrin, A., et al. 2012b, *arXiv:1211.2230*
- Bowler, R. A. A., Dunlop, J. S., McLure, R. J., et al. 2012, *MNRAS*, 426, 2772
- Bradac, M., Gonzalez, A., Schrabback, T., et al. 2012, *Spitzer Proposal*, 90009
- Bradley, L. D., Bouwens, R. J., Zitrin, A., et al. 2012a, *ApJ*, 747, 3
- Bradley, L. D., Trenti, M., Oesch, P. A., et al. 2012b, *ApJ*, 760, 108
- Bouwens, R. J., Illingworth, G. D., Oesch, P. A., et al. 2013, *arXiv:1306.2950*
- Brammer, G. B., van Dokkum, P. G., & Coppi, P. 2008, *ApJ*, 686, 1503
- Bruzual, G., & Charlot, S. 2003, *MNRAS*, 344, 1000
- Coe, D., Umetsu, K., Zitrin, A., et al. 2012, *ApJ*, 757, 22
- Calzetti, D., Armus, L., Bohlin, R. C., et al. 2000, *ApJ*, 533, 682
- Curtis-Lake, E., McLure, R. J., Dunlop, J. S., et al. 2013, *MNRAS*, 429, 302
- Daddi, E., Dickinson, M., Morrison, G., et al. 2007, *ApJ*, 670, 156
- Davé, R., Oppenheimer, B. D., & Finlator, K. 2011, *MNRAS*, 415, 11
- de Barros, S., Schaerer, D., & Stark, D. P. 2012, *arXiv:1207.3663*
- Erb, D. K., Steidel, C. C., Shapley, A. E., et al. 2006, *ApJ*, 647, 128
- Fumagalli, M., Patel, S. G., Franx, M., et al. 2012, *ApJ*, 757, L22
- González, V., Labbé, I., Bouwens, R. J., et al. 2010, *ApJ*, 713, 115
- González, V., Bouwens, R. J., Labbé, I., et al. 2012a, *ApJ*, 755, 148
- González, V., Bouwens, R., Illingworth, G., et al. 2012b, *arXiv:1208.4362*
- Postman, M., Coe, D., Benítez, N., et al. 2012, *ApJS*, 199, 25
- Kennicutt, Jr., R. C. 1998, *ARA&A*, 36, 189
- Koekemoer, A. M., Faber, S. M., Ferguson, H. C., et al. 2011, *ApJS*, 197, 36
- Kriek, M., van Dokkum, P. G., Labbé, I., et al. 2009, *ApJ*, 700, 221
- Labbé, I., González, V., Bouwens, R. J., et al. 2010a, *ApJ*, 716, L103
- Labbé, I., González, V., Bouwens, R. J., et al. 2010b, *ApJ*, 708, L26
- Labbe, I., Oesch, P. A., Bouwens, R. J., et al. 2012, *submitted to ApJL*, *arXiv:1209.3037*
- Lorenzoni, S., Bunker, A. J., Wilkins, S. M., et al. 2011, *MNRAS*, 414, 1455
- Makovoz, D., & Khan, I. 2005, *Astronomical Data Analysis Software and Systems XIV*, 347, 81
- Meurer, G. R., Heckman, T. M., & Calzetti, D. 1999, *ApJ*, 521, 64
- Neistein, E., & Dekel, A. 2008, *MNRAS*, 388, 1792
- Noeske, K. G., Weiner, B. J., Faber, S. M., et al. 2007, *ApJ*, 660, L43
- Oesch, P. A., Bouwens, R. J., Illingworth, G. D., et al. 2012, *ApJ*, 745, 110
- Oesch, P. A., Bouwens, R. J., Illingworth, G. D., et al. 2013, *arXiv:1301.6162*
- Oke, J. B., & Gunn, J. E. 1983, *ApJ*, 266, 713
- Ono, Y., Ouchi, M., Mobasher, B., et al. 2012, *ApJ*, 744, 83
- Ouchi, M., Ellis, R., Ono, Y., et al. 2013, *arXiv:1306.3572*
- Reddy, N., Dickinson, M., Elbaz, D., et al. 2012, *ApJ*, 744, 154

- Salpeter, E. E. 1955, *ApJ*, 121, 161
- Shim, H., Chary, R.-R., Dickinson, M., et al. 2011, *ApJ*, 738, 69
- Schaerer, D., & de Barros, S. 2009, *A&A*, 502, 423
- Schaerer, D., & de Barros, S. 2010, *A&A*, 515, A73
- Schenker, M. A., Ellis, R. S., Konidaris, N. P., & Stark, D. P. 2013b, arXiv:1306.1518
- Schenker, M. A., Robertson, B. E., Ellis, R. S., et al. 2013a, *ApJ*, 768, 196
- Stanway, E. R., Bunker, A. J., & McMahon, R. G. 2003, *MNRAS*, 342, 439
- Stark, D. P., Ellis, R. S., Bunker, A., et al. 2009, *ApJ*, 697, 1493
- Stark, D. P., Schenker, M. A., Ellis, R., et al. 2013, *ApJ*, 763, 129
- Steidel, C. C., Adelberger, K. L., Giavalisco, M., Dickinson, M., & Pettini, M. 1999, *ApJ*, 519, 1
- Tilvi, V., Papovich, C., Tran, K.-V. H., et al. 2013, *ApJ*, 768, 56
- van der Wel, A., Straughn, A. N., Rix, H.-W., et al. 2011, *ApJ*, 742, 111
- Weinmann, S. M., Neistein, E., & Dekel, A. 2011, *MNRAS*, 417, 2737
- Yabe, K., Ohta, K., Iwata, I., et al. 2009, *ApJ*, 693, 507
- Zitrin, A., Broadhurst, T., Umetsu, K., et al. 2009, *MNRAS*, 396, 1985
- Zitrin, A., Broadhurst, T., Umetsu, K., et al. 2010, *MNRAS*, 408, 1916
- Zitrin, A., Broadhurst, T., Barkana, R., Rephaeli, Y., & Benítez, N. 2011, *MNRAS*, 410, 1939

4

High-Precision Photometric Redshifts from Spitzer/IRAC: Extreme [3.6]-[4.5] Colors Identify Galaxies in the Redshift Range $z \sim 6.6 - 6.9$

One of the most challenging aspects of studying galaxies in the $z \gtrsim 7$ universe is the infrequent confirmation of their redshifts through spectroscopy, a phenomenon thought to occur from the increasing opacity of the intergalactic medium to $\text{Ly}\alpha$ photons at $z > 6.5$. The resulting redshift uncertainties inhibit the efficient search for [CII] in $z \sim 7$ galaxies with sub-mm instruments such as ALMA, given their limited scan speed for faint lines. One means by which to improve the precision of the inferred redshifts is to exploit the potential impact of strong nebular emission lines on the colors of $z \sim 4 - 8$ galaxies as observed by *Spitzer*/IRAC. At $z \sim 6.8$, galaxies exhibit IRAC colors as blue as $[3.6] - [4.5] \sim -1$, likely due to the contribution of [OIII]+H β to the $3.6 \mu\text{m}$ flux combined with the absence of line contamination in the $4.5 \mu\text{m}$ band. In this chapter we explore the use of extremely blue [3.6]–[4.5] colors to identify galaxies in the narrow redshift window $z \sim 6.6 - 6.9$. When combined with an *I*-dropout criterion, we demonstrate that we can plausibly select a relatively clean sample of $z \sim 6.8$ galaxies. Through a systematic application of this selection technique to our catalogs from all five CANDELS fields, we identify 20 probable $z \sim 6.6 - 6.9$ galaxies. We estimate that our criteria select the $\sim 50\%$ strongest line emitters at $z \sim 6.8$ and from the IRAC colors we estimate a typical [OIII]+H β rest-frame equivalent width of 1085 \AA for this sample. The small redshift uncertainties on our sample make it particularly well suited for follow-up studies with facilities such as ALMA.

4.1 Introduction

Since the installation of the Wide Field Camera 3 (WFC3) on the *Hubble Space Telescope* (*HST*), numerous ultraviolet (UV) bright galaxies in the reionization era have been detected through their broadband photometric properties. These observations allow for the determination of the UV luminosity function (e.g., Bouwens et al., 2011; Lorenzoni et al., 2011; Oesch et al., 2012, 2013, 2014; Bradley et al., 2012; Bowler et al., 2012, 2014; Schenker et al., 2013a; McLure et al., 2013) and the typical UV colors of galaxies out to $z \sim 8$ (Stanway et al., 2005; Bouwens et al., 2009, 2012, 2014a; Dunlop et al., 2012, 2013; Wilkins et al., 2011; Finkelstein et al., 2012).

In contrast to the success of identifying candidate galaxies out to $z \sim 8$ with *HST*/WFC3 imaging, confirming the redshift of these sources with spectroscopy has proven very challenging due to the absorption of Ly α photons by the neutral Intergalactic Medium (IGM) at $z \gtrsim 6.5$ (Pentericci et al., 2011; Treu et al., 2013; Finkelstein et al., 2013; Caruana et al., 2014; Schenker et al., 2014; Vanzella et al., 2014). This creates particular challenges for follow-up studies with the newest generation of sub-mm telescopes such as ALMA. ALMA has the potential to perform detailed studies of star formation rates (SFRs), kinematic structure, and energetics of $z \sim 6 - 8$ galaxies through the direct detection of sub-mm fine structure lines such as [CII] $\lambda 157.7 \mu\text{m}$ (e.g. Carilli & Walter, 2013). However, the frequency range that ALMA is able to scan in one tuning is relatively small, making follow-up studies with ALMA on sources without accurate redshift information observationally expensive.

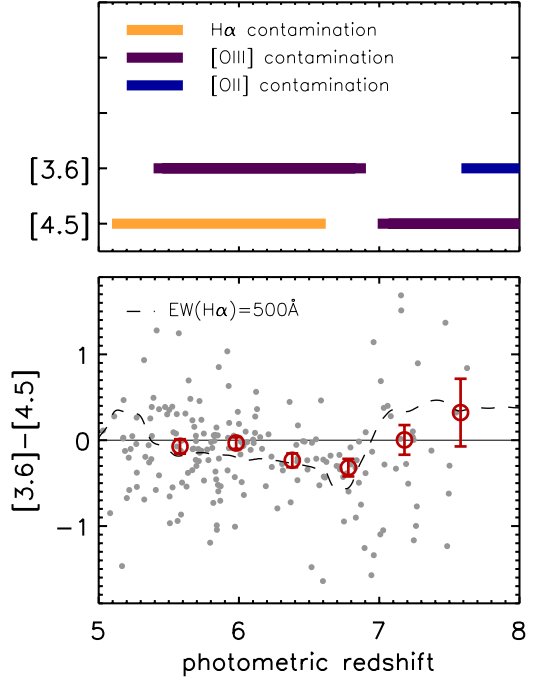
One way to make progress in this area involves a search for the CIII] $\lambda 1908 \text{ \AA}$ line in $z \gtrsim 6$ galaxies (Stark et al., 2014a,b). This line has a typical rest-frame equivalent width (EW_0) of $\sim 4 - 14 \text{ \AA}$ in two $z \sim 6 - 7$ galaxies where this line has been successfully located (Stark et al., 2014b) and in low-mass lensed star-forming galaxies at $z \sim 2$ (Stark et al., 2014a). The challenge with this approach is the faintness of the CIII] line and high density of sky lines in many regions of the near-infrared (IR) spectrum.

Another potentially promising way forward is to utilize the information provided by the *Spitzer*/IRAC. Recent studies have reported evidence for the presence of strong nebular emission lines such as H α and [OIII] $\lambda 5007 \text{ \AA}$ through the apparent impact of these lines on the IRAC 3.6 μm and 4.5 μm fluxes of $z \sim 4 - 8$ galaxies (Schaerer & de Barros, 2009; Shim et al., 2011; Stark et al., 2013; Labbé et al., 2013; González et al., 2012, 2014; Smit et al., 2014). These lines appear to cause the [3.6]–[4.5] colors of high redshift galaxies to vary significantly as a function of redshift. This results in modestly blue [3.6]–[4.5] colors in $z \sim 6$ galaxies, where both bands are contaminated by emission lines, very blue [3.6]–[4.5] colors at $z \sim 6.8$, where only the 3.6 μm band suffers line contamination, and red [3.6]–[4.5] colors for sources at redshifts $z > 7$, where the 4.5 μm band is contaminated (Labbé et al., 2013; Wilkins et al., 2013; Smit et al., 2014; Laporte et al., 2014).

In this chapter we attempt to exploit the extreme IRAC colors galaxies exhibit at specific redshifts to isolate galaxies over a narrow range in redshift. To test this method, we utilize a large sample of $z \sim 5 - 8$ galaxies identified from the CANDELS program (Grogin et al., 2011; Koekemoer et al., 2011). We select a sample of sources with extremely blue [3.6]–[4.5] IRAC colors and show that these sources likely fall in the narrow redshift range $z \sim 6.6 - 6.9$. Ultimately, of course, this approach and the assumptions behind it will need to be tested through spectroscopy with the *James Webb Space Telescope* (*JWST*).

Additionally we discuss a few objects with blue [3.6]–[4.5] colors that are clearly at $z \lesssim 6.6$

Figure 4.1: *Top panel:* A schematic overview of the redshift range where the strongest nebular lines ($H\alpha$, [OIII] and [OII]) can contaminate the rest-frame optical flux in the $3.6 \mu\text{m}$ and $4.5 \mu\text{m}$ bands. *Bottom panel:* Measurements of the $[3.6]-[4.5]$ color (grey points) in UV-selected galaxies from GOODS-N/S, placed at their photometric redshift. The red points indicate the median colors in $\Delta z = 0.4$ redshift bins (error bars represent the uncertainty in the median, i.e., σ/\sqrt{N}). The black dashed line provides an example of the IRAC color at different redshifts for a source with flat continuum and $\text{EW}_0(H\alpha) = 500 \text{ \AA}$ in combination with emission line ratios as defined by Anders & Fritze-v. Alvensleben (2003) for sub-solar metallicity $Z = 0.2Z_\odot$. The overall blue $[3.6]-[4.5]$ colors at $z < 7$, versus red $[3.6]-[4.5]$ colors at $z > 7$ indicate that in particular the presence of [OIII] in the IRAC bands might have a significant impact on the $[3.6]-[4.5]$ color.



from their *HST* photometry, and we suggest that these objects could be explained by high [OIII]/ $H\beta$ ratios such as found at $z \sim 3$ (Schenker et al., 2013b; Holden et al., 2014).

This chapter is organized as follows. §2 discusses our data set and photometric procedure. §3 presents the $[3.6]-[4.5]$ IRAC colors as a function of photometric redshift for a sample of $z \sim 5 - 8$ UV-selected galaxies. §4 discusses the selection of extreme $[3.6]-[4.5]$ color galaxies, and §5 presents our $z \sim 6.6 - 6.9$ galaxy sample. §6 gives a short summary of our results.

Throughout this chapter we adopt a Salpeter IMF with limits $0.1-100 M_\odot$ (Salpeter, 1955). For ease of comparison with previous studies we take $H_0 = 70 \text{ km s}^{-1} \text{ Mpc}^{-1}$, $\Omega_m = 0.3$ and $\Omega_\Lambda = 0.7$. Magnitudes are quoted in the AB system (Oke & Gunn, 1983).

4.2 Observations, photometry and $z \sim 5 - 8$ sample

4.2.1 *HST* data and photometry

The primary sample of $z \sim 5 - 8$ galaxies that we use in this chapter was selected from the catalogs described by Bouwens et al. (2014b). The purpose of this sample is to establish how the $[3.6]-[4.5]$ color of galaxies depends on redshift and also to establish the redshift distribution of galaxies with the most extreme IRAC colors. The catalogs were compiled from *HST* ACS (B_{435} , V_{606} , i_{775} , I_{814} and z_{850}) and WFC3/IR (Y_{098}/Y_{105} , J_{125} , JH_{140} and H_{160}) data over the GOODS-N and GOODS-S fields. We also used the deep and wide-area observations obtained in the HUDF09+HUDF12 (Beckwith et al., 2006; Bouwens et al., 2011; Ellis et al.,

2013; Illingworth et al., 2013), ERS (Windhorst et al., 2011) and CANDELS (Grogin et al., 2011; Koekemoer et al., 2011) programs as well as any archival *HST* observations over these fields. The shallow JH_{140} imaging was taken from the 3D-*HST* survey (Brammer et al., 2012a) and A Grism H-Alpha Spectroscopic survey (AGHAST, PI:Weiner). The procedure for reducing the data is described in detail by Illingworth et al. (2013) and Bouwens et al. (2014b).

A secondary sample of $z \sim 5 - 8$ galaxies is used to increase the number of $z \sim 6.8$ and $z \sim 6.0$ galaxies in our selection. We derived this sample from the *HST* data over the CANDELS-UDS, CANDELS-COSMOS, and CANDELS-EGS fields (V_{606} , I_{814} , J_{125} and H_{160} , for more details on the CANDELS fields see Koekemoer et al. 2011 and Skelton et al. 2014) and deep U - and B -band ground-based observations from CFHT and Subaru (Capak et al., 2007; Furusawa et al., 2008).

An overview of all fields, bands and depths is given in Table 1 of Bouwens et al. (2014b). Both the ACS and WFC3/IR data reach total magnitudes of $\gtrsim 27.2$ at 5σ , using as a basis the flux uncertainties on the total magnitude measurements for the faintest 20% of galaxies from the Bouwens et al. (2014b) catalogs over these fields. Our total search area over all the fields is 720 arcmin^2 .

The photometry followed the procedure described by Bouwens et al. (2012). In short, we ran an adapted version of the Source Extractor software (Bertin & Arnouts, 1996) in dual-image mode. The detection images were created by combining all deep bands redwards of the Lyman break (i.e., Y_{098}/Y_{105} , J_{125} , and H_{160}) into a square-root χ^2 image (Szalay et al., 1999). After matching the observations to the H_{160} -band point spread function (PSF), colors and total magnitudes were measured in Kron-like apertures with Kron factors 1.6 and 2.5 respectively (defined on the H_{160} -band).

4.2.2 *Spitzer*/IRAC data and photometry

The first part of our *Spitzer*/IRAC data set covers all five CANDELS fields with the $3.6 \mu\text{m}$ and $4.5 \mu\text{m}$ bands¹ from the *Spitzer* Extended Deep Survey (SEDS, PI: Fazio) and all available archival data sets from before 2011 (Ashby et al., 2013). We complement this data set with the new deep IRAC imaging from the *Spitzer* Very Deep Survey (S-CANDELS) Exploration Science Project (Ashby et al., submitted), which brings the IRAC coverage up to 50 hours in depth (26.8 mag at 5σ in the $3.6 \mu\text{m}$ band). For the sources in the HUDF, we utilize additional data from the IRAC Ultra Deep Field (IUDF: Labbé et al., 2013) program.

Before performing photometry on the sources in our sample, we removed the contamination of foreground sources with an automated cleaning procedure (Labbé et al., 2010a,b). In short, the *HST* images provided a high-spatial resolution template with which to model the positions and flux profiles of the foreground sources. The light profiles of individual sources in the *HST* image were convolved with a kernel to match the IRAC PSF and then simultaneously fitted to the IRAC image within a region of ~ 11 arcseconds around the sources from our sample. We subtracted the flux from the foreground galaxies and performed photometry in $2''.0$ -diameter circular apertures on the resulting images. We applied a correction to account for the flux outside of the aperture, given by the ratio of the flux enclosed in the photometric aperture in the *HST* image (before convolution) to the IRAC model (after convolution). This correction ranges from

¹<http://irsa.ipac.caltech.edu/data/SPITZER/docs/irac/calibrationfiles/spectralresponse/>

$\sim 2.2\times$ to $\sim 2.4\times$, depending on the size of the source. The local noise was estimated from the clean background on a residual IRAC image from which all sources were subtracted. Our procedure for deblending can fail when contaminating sources are too bright or too close to the central source. We removed sources from our sample with a high χ^2 parameter determined from the residual IRAC image (see §4.2.3).

4.2.3 Base sample of $z \sim 5 - 8$ galaxies

In this section, we present the base sample of $z \sim 5 - 8$ galaxies we use to study how the IRAC colors of star-forming galaxies depend upon redshift. We selected our sources from which we measure IRAC colors in the rest-frame UV, adopting the Lyman-break technique (Steidel et al., 1999) with the requirement that the source drops out in the I_{814} band. Specifically, our requirements for $z \sim 5 - 8$ Lyman Break Galaxies (LBGs) were

$$(I_{814} - J_{125} > 0.8) \wedge (J_{125} - H_{160} < 0.4) \\ \wedge (I_{814} - J_{125} > 2(J_{125} - H_{160}) + 0.8), \quad (4.1)$$

where \wedge indicates logical AND. We chose the I_{814} and J_{125} band fluxes for our identification of $z \gtrsim 5$ Lyman Break galaxies, instead of more closely spaced passbands like z_{850} and Y_{105} , which are available over the GOODS-N and GOODS-S fields. While this is less optimal for selecting a sample of galaxies with the lowest contamination rate, these bands were chosen in order to select galaxies over a relatively extended redshift range $z \sim 5.5$ to $z \sim 8.5$ (without any gaps) and to use filters that are available over all five CANDELS fields for a more uniform selection. Information from the more closely spaced bandpasses was nevertheless utilized in deriving photometric redshifts for sources from our selection and hence determining the relationship between the IRAC colors of sources and their redshifts.

We also required sources to have either a non-detection in the V_{606} band ($< 2\sigma$) or to have a very strong Lyman break, i.e., $V_{606} - J_{125} > 2.5$. Furthermore, we required sources to be undetected ($< 2\sigma$) in the available B_{435} -band data over GOODS North and South or, in the case of the CANDELS UDS, COSMOS, or EGS fields, to be undetected ($< 2.5\sigma$) in the χ^2 statistic image Bouwens et al. (2014b) derived from the ground-based U and B images. We required the SExtractor stellarity parameter (equal to 0 and 1 for extended and point sources, respectively) in the J_{125} band be less than 0.92 to ensure that our selection is largely free of contamination by stars (e.g. Holwerda et al., 2014). Moreover, the blue IRAC color criterion introduced in §4.2.3 also selects effectively against contamination from brown dwarfs in our Milky Way (Kirkpatrick et al. 2011, Holwerda et al., in prep). We selected sources with a signal-to-noise ratio $S/N(H_{160}) > 5$, and additionally we required $f_\nu(H_{160})/ef_\nu(3.6 \mu\text{m}) > 2.5$ and $f_\nu(H_{160})/ef_\nu(4.5 \mu\text{m}) > 2.5$, where $f_\nu(H_{160})$ is the measured flux density in the H_{160} band and $ef_\nu(3.6 \mu\text{m})$ and $ef_\nu(4.5 \mu\text{m})$ are the estimated uncertainties in the $3.6 \mu\text{m}$ and $4.5 \mu\text{m}$ band fluxes. Our chosen requirements explicitly do not include a dependence on the observed flux in the IRAC bands to ensure that our results are not biased according to the emission line flux in our candidates. In practice, most high-redshift sources exhibit a somewhat red UV-to-optical color (González et al., 2012), and as a result 75% of our sample is detected at $> 5\sigma$ in the $3.6 \mu\text{m}$ IRAC band. We exclude those $\sim 30\%$ of the sources that show strong residuals in the IRAC images after our deblending procedure (§4.2.2), which results in a final sample of 220 sources in GOODS-N/S and 224 sources in CANDELS-EGS/UDS/COSMOS.

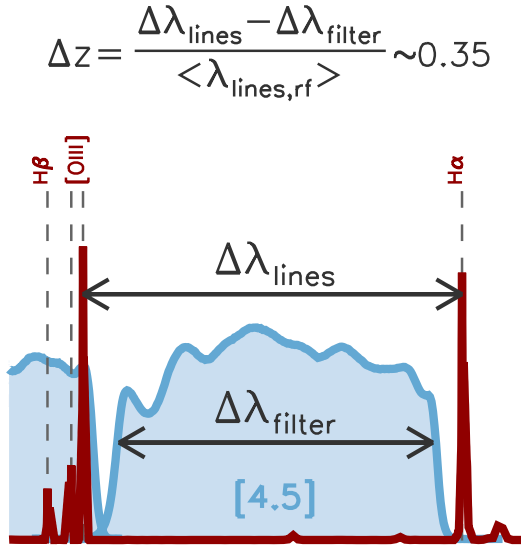


Figure 4.2: An illustration of the position of the optical nebular emission lines in a $z \sim 6.8$ star-forming galaxy (red line) with respect to the *Spitzer*/IRAC response function (indicated in blue). Our strategy for selecting star-forming galaxies in the narrow redshift range $z \sim 6.6 - 6.9$ capitalizes on the [OIII] and H α emission lines being separated by almost the same wavelength difference as the width of *Spitzer*/IRAC 4.5 μm band. Our [3.6]–[4.5] selection technique furthermore requires that the [OIII] line has not yet dropped out of the 3.6 μm band, which narrows the redshift window where we expect to find these ultra-blue galaxies, from $\Delta z \sim 0.35$ to $\Delta z \sim 0.25$.

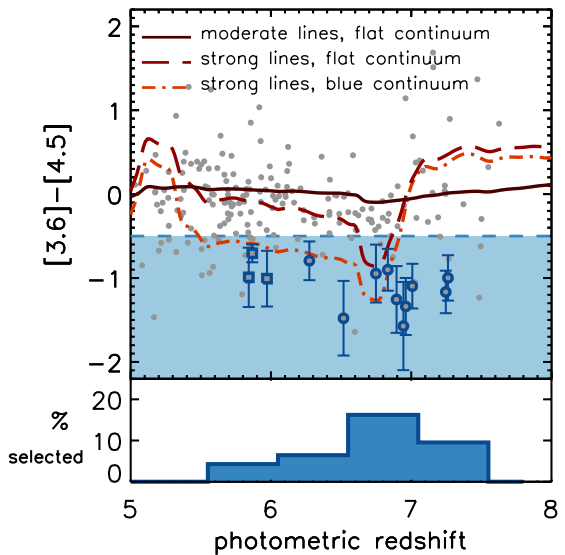
4.3 [3.6]–[4.5] color vs. redshift

Before moving onto a discussion of how the IRAC [3.6]–[4.5] color might be used to refine redshift determinations for specific $z > 6$ selections, it is useful to quickly assess whether our sample agrees with our main assumption: that the [3.6]–[4.5] color is strongly influenced by the presence of strong nebular emission lines such as H α and [OIII] in the IRAC filters. To this end we explore the variation of the median [3.6]–[4.5] color as a function of redshift for our sample.

Figure 4.1 shows the colors of our GOODS-N/S sample as a function of the photometric redshift, as derived from the *HST* broadband photometry. We used the software Easy and Accurate Zphot from Yale (EAZY; Brammer et al., 2008) to estimate photometric redshifts for the galaxies in our sample. We used the standard template set of EAZY, but we complemented these templates with a number of templates generated with Galaxy Evolutionary Synthesis Models (GALEV; Kotulla et al., 2009), which includes nebular continuum and emission lines as described by Anders & Fritze-v. Alvensleben (2003). Additionally we included a template with an [OIII] λ 4959,5007 \AA /H β ratio of 10 to match the most extreme line ratios observed in spectroscopy of galaxies at lower redshifts (Amorín et al., 2012; Brammer et al., 2012b; Jaskot & Oey, 2013; Schenker et al., 2013b; van der Wel et al., 2013; Holden et al., 2014; Steidel et al., 2014). No use of the *Spitzer*/IRAC photometry is made in the photometric redshift determination to avoid coupling between our redshift estimates and the measured IRAC fluxes. We do not include sources from our EGS/UDS/COSMOS sample in Figure 4.1 because of the lack of deep *HST* coverage in the z_{850} and Y_{105}/Y_{098} bands, which is needed for obtaining sufficiently accurate redshifts for the analysis we describe.

We observe a clear discontinuity in the median color (red points) around $z \sim 7$, where the [OIII] emission line moves from the 3.6 μm to the 4.5 μm band. Moreover, we find the bluest median [3.6]–[4.5] color at $z \sim 6.8$, where [OIII] boosts the 3.6 μm flux while H α has already moved out of the 4.5 μm band. This suggests that the IRAC colors are strongly influenced by

Figure 4.3: *Top panel:* Measurements of the [3.6]–[4.5] color (grey points) in UV-selected galaxies from GOODS-N/S, placed at their photometric redshift (see also bottom panel of Figure 4.1). The blue encircled points indicate sources that show IRAC colors significantly bluer than [3.6]–[4.5] < -0.5 (blue shaded area), as given by Eq. 4.2 (the ultra-blue [3.6]–[4.5] colors for many sources in the blue shaded area are not significant). Blue circles indicate sources that are consistent with the redshift range $z \sim 6.6 - 6.9$, while blue squares indicate sources that are at $z < 6.6$ from their photometric redshift probability distribution (99% confidence). The solid lines indicate three tracks of galaxy templates: the dark red solid line indicates a stellar population with moderate emission lines ($EW_{H\alpha,0} \sim 100 \text{ \AA}$) and a flat continuum, the red dashed lines indicates a young ($\sim 5 \text{ Myr}$) stellar population with strong emission lines ($EW_{H\alpha,0} \sim 1000 \text{ \AA}$) and a flat continuum from moderate dust extinction ($E(B - V) \sim 0.2$), while the dot-dashed orange line indicates a young population with strong emission lines, in combination with a high [OIII]/H β ratio such as described in Anders & Fritze-v. Alvensleben (2003) for low metallicity gas ($Z = 0.2Z_{\odot}$) and with blue continuum (dust-free). *Bottom panel:* The percentage of the galaxy population that has blue [3.6]–[4.5] colors, such as defined by Eq. 4.2, at a given photometric redshift. The presence of extremely blue [3.6]–[4.5] colors is most abundant in galaxy candidates at $z \sim 7$.



emission lines, in agreement with recent studies (Schaerer & de Barros, 2009; Shim et al., 2011; Stark et al., 2013; Labbé et al., 2013; González et al., 2012, 2014; Smit et al., 2014) and in agreement with predictions of stellar population synthesis models with emission lines. We can use this information to improve our determinations of the redshift probability functions for strong line emitters by including the IRAC fluxes in our photometric redshift estimates.

4.4 Ultra-blue [3.6]–[4.5] galaxies

In the previous section we showed how the [3.6]–[4.5] IRAC color would likely change as the [OIII] and H α nebular lines move in and out of the photometric bands, due to the redshifting spectrum. We can use this information to significantly improve our photometric redshift estimates. In particular the IRAC [3.6]–[4.5] color can provide a valuable constraint in sources that have uncertain photometric redshifts from their HST photometry, such as sources over COSMOS, UDS or EGS where only 4 HST bands are available. This is important due to the considerable challenges involved in improving redshift estimates through spectroscopy (largely due to the impact of the more neutral IGM on the prevalence of Ly α emission in $z > 6.5$ galaxies). In

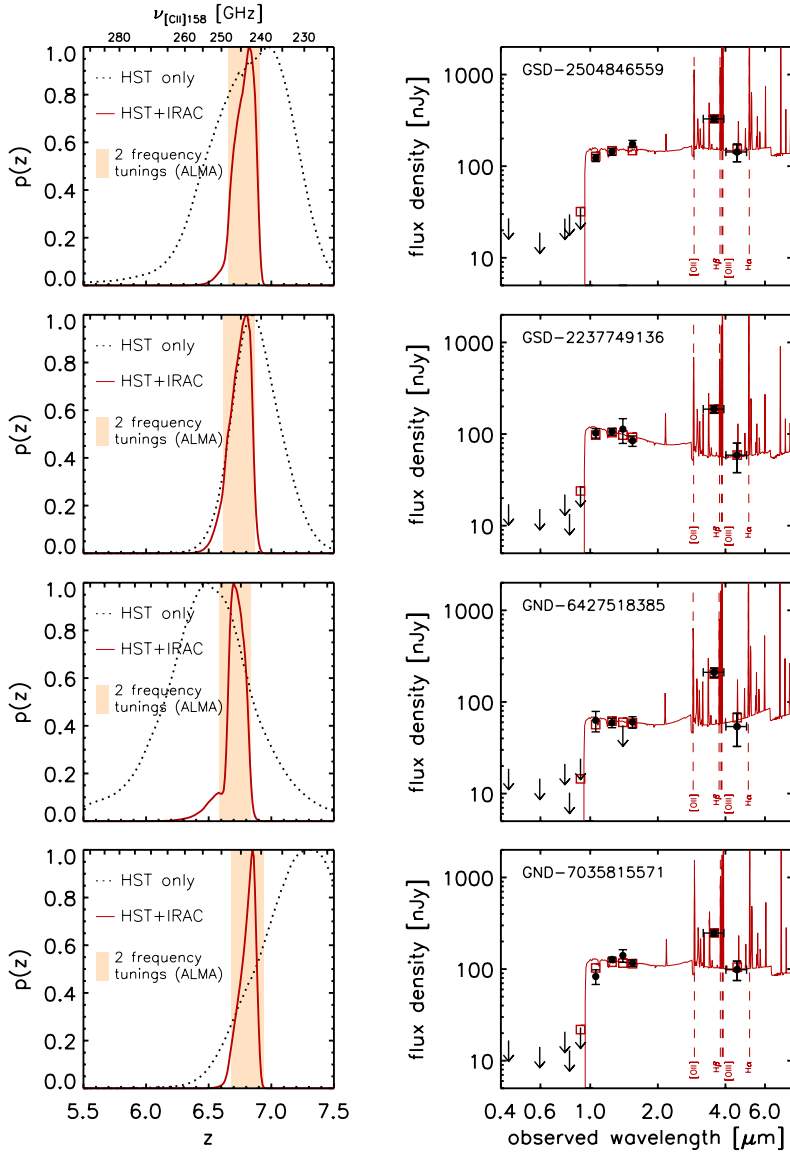


Figure 4.4: Four examples of sources selected on their blue IRAC colors (Eq. 4.2) that have a photometric redshift probability distribution consistent (within the 95% confidence interval) with the redshift range $z \sim 6.6 - 6.9$; from top to bottom GSD-2504846559, GSD-2237749136, GND-6427518385, and GND-7035815571 (from the larger Bouwens et al. 2014b catalogs). *Left panels:* the redshift probability distribution using only the *HST* bands (black dotted line) and using the constraints from both *HST* and *Spitzer*/IRAC (red line). Due to the substantial impact [OIII] emission can have on the 3.6 μm flux, the [3.6]–[4.5] color can set tight constraints on the redshifts of individual sources. Two ALMA tunings (indicated with the yellow shaded regions) would be sufficient to obtain a spectroscopic redshift through the [CII] $\lambda 158 \mu\text{m}$ line if one is present within the $\sim 95\%$ likelihood window. *Right panel:* Flux densities and 2σ upper limits (black points and arrows) of the *HST* and *Spitzer*/IRAC photometry with the best-fit template (red line). For sources in the redshift window $z \sim 6.6 - 6.9$, the 4.5 μm band is not contaminated by strong emission lines, in contrast with the 3.6 μm band which is dominated by the flux in the [OIII] line.

this section we will investigate a [3.6]–[4.5] color selection on our sample of $z \sim 5 - 8$ galaxies over the GOODS-N and GOODS-S, where good photometric redshift constraints are available and in §4.5 we will present a sample of $z \sim 6.6 - 6.9$ galaxies over all five CANDELS fields.

4.4.1 Blue [3.6]–[4.5] sources at $z \sim 6.8$

A particularly interesting redshift interval is $z \sim 6.6 - 6.9$, where we expect extreme [3.6]–[4.5] colors due to the presence of the [OIII] line in the $3.6 \mu\text{m}$ band and the absence of any strong emission lines in the $4.5 \mu\text{m}$ band. This is illustrated in Figure 4.2. Because the $\text{H}\alpha$ to [OIII] line separation ($\Delta\lambda_{\text{lines}}$) at $z \sim 6.8$ is slightly wider than the $4.5 \mu\text{m}$ filter width ($\Delta\lambda_{\text{filter}}$), there is very narrow redshift range $\Delta z = (\Delta\lambda_{\text{lines}} - \Delta\lambda_{\text{filter}}) / \langle\lambda_{\text{lines,rest-frame}}\rangle = 0.35$ in which the $4.5 \mu\text{m}$ band is free of strong emission lines. In practice, the effective redshift range where we can observe the extremely blue IRAC colors is even narrower than this, i.e., $\Delta z \sim 0.25$, because the relevant wavelength is where [OIII] leaves the $3.6 \mu\text{m}$ filter, not where this line enters the $4.5 \mu\text{m}$ filter (see the top panel of Figure 4.1).

To investigate whether the selection of sources with blue [3.6]–[4.5] colors can be used to unambiguously identify galaxies at $z \sim 6.8$, we collected a sample of emission line candidate galaxies by selecting sources with [3.6]–[4.5] colors significantly bluer than -0.5 mag. We adopted the criterion

$$P([3.6] - [4.5] < -0.5) > 84\%. \quad (4.2)$$

This criterion indicates that the sources in our selection have a probability (P) of at least 84% to have a true IRAC color bluer than $[3.6] - [4.5] < -0.5$, based on the uncertainties in the $3.6 \mu\text{m}$ and $4.5 \mu\text{m}$ fluxes. We show the galaxies meeting this color criterion in Figure 4.3. A color cut in the [3.6]–[4.5] color can identify galaxies with strong emission lines in the redshift range $z \sim 6.6 - 6.9$, but a galaxy with more moderate emission lines and very blue continuum [3.6]–[4.5] colors can also meet the criterion.

We purposely decided to try to select $z \sim 6.8$ galaxies based on a color criterion rather than fitting emission line templates to the IRAC bands to obtain photometric redshifts. This was done to avoid a dependence on the SED template set and the assumed line ratios in these templates. Since the physical properties of the H_2 regions in star-forming galaxies, such as gas metallicity and gas density, strongly influence the line ratios we observe (e.g. Kewley et al., 2013) we wanted to avoid having our results implicitly depend on these ratios.

Over the 270 arcmin^2 CANDELS/ERS region of GOODS-North and GOODS-South, 13 sources satisfy this criterion out of the 220 sources from our base $z \sim 5 - 8$ sample. We indicate these in the top panel of Figure 4.3 and show a histogram in the bottom panel of Figure 4.3. Furthermore there are 15 sources out of 224 sources from the base sample over a 450 arcmin^2 area in the CANDELS-EGS/CANDELS-UDS/CANDELS-COSMOS fields that meet the criterion, but we do not present them in Figure 4.3 due to the greater difficulty in determining their photometric redshifts.

We identify a large number of blue [3.6]–[4.5] sources that are broadly consistent with a $z \sim 6.8$, similar to the sources found by Smit et al. (2014). For these galaxies the extreme [3.6]–[4.5] colors are explained by the likely scenario that the [OIII] emission dominates the $3.6 \mu\text{m}$ flux while at the same time the $4.5 \mu\text{m}$ flux is free of emission line contamination. Interestingly enough, Figure 4.3 indicates there might be a few sources at slightly lower redshift (at

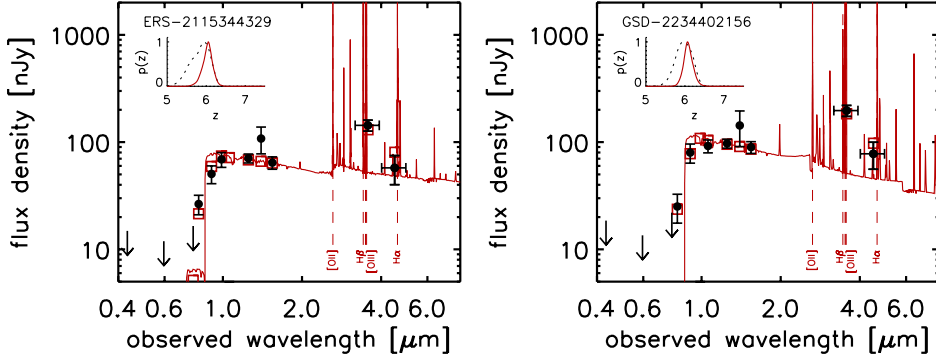


Figure 4.5: Two examples of sources that prefer a redshift below $z < 6.6$ (ERS-2115344329 and GSD-2234402156) from their photometric redshift distribution (99% confidence), but that also satisfy our $[3.6] - [4.5]$ color criterion (Eq. 4.2). Flux densities and upper limits (2σ) of the *HST* and *Spitzer*/IRAC photometry are indicated with black points and arrows, while the best-fit template is drawn in red. The $4.5 \mu\text{m}$ band is dominated by the flux in the [OIII] line. The inset panel in the top left corner indicates the redshift probability distribution using only the *HST* bands (black dotted line) and using the constraints from both *HST* and *Spitzer*/IRAC (red line).

$z \sim 6.0$ instead of at $z \sim 6.8$) with such blue IRAC colors; we will discuss these sources in §4.4.2.

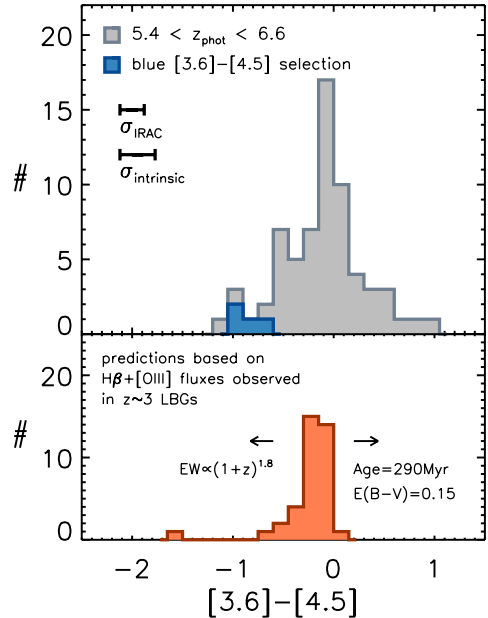
Figure 4.4 shows four examples of blue $[3.6] - [4.5]$ sources in GOODS-N/S that are consistent with a $z \sim 6.8$ from their *HST* photometry only. We present the redshift probability function using only the *HST* bands and also when using constraints from both *Spitzer*/IRAC and *HST*. Due to their extreme $[3.6] - [4.5]$ colors we can place very tight constraints on the photometric redshift of these galaxies.

This is particularly useful for follow-up studies to obtain line detections with sub-mm detectors such as ALMA. Line detections with interferometer arrays are inherently limited in frequency space by the capabilities of the correlator. ALMA can roughly observe ~ 4 GHz in one tuning in band 6 (211-275 GHz)². As a reference we indicate the frequency of the bright [CII] $\lambda 157.7 \mu\text{m}$ line at a given redshift in Figure 4.4 and we indicate the frequency range that ALMA can observe in two frequency tunings. With only twice the observing time required with respect to spectroscopically confirmed sources, we can typically search the $\sim 95\%$ probability window for [CII] emission in these sources.

The selection of galaxies at $z \sim 6.8$ is also of interest for deriving stellar masses of high-redshift galaxies using *Spitzer*/IRAC constraints (Eyles et al., 2005, 2007; Yan et al., 2005, 2006; Labbé et al., 2006, 2010b; Yabe et al., 2009; Stark et al., 2009; González et al., 2010, 2011; Curtis-Lake et al., 2013). In particular, the redshift range $z \sim 6.6 - 7.0$ provides us with the only opportunity beyond $z \gtrsim 5.4$ to measure the rest-frame optical stellar continuum without the contamination of nebular line emission in the $4.5 \mu\text{m}$ band, allowing for more accurate stellar mass and specific star formation rate estimates (e.g., Smit et al., 2014).

²A. Lundgren, 2013, ALMA Cycle 2 Technical Handbook Version 1.1, ALMA, ISBN 978-3-923524-66-2

Figure 4.6: *Top panel:* The [3.6]–[4.5] color distribution (grey histogram) of sources with photometric redshifts (from the *HST* photometry) within the redshift range $z \sim 5.4 - 6.6$ (68% confidence) where [OIII] contributes to the $3.6 \mu\text{m}$ flux, while $\text{H}\alpha$ contributes to the $4.5 \mu\text{m}$ flux. Sources that satisfy our ultra-blue IRAC selection criterion (Eq. 4.2), but prefer a $z < 6.6$ are indicated with the blue histogram (note that for a few sources the very blue [3.6]–[4.5] colors are not significant). The upper error bar on the left side of the panel indicates the scatter in the [3.6]–[4.5] color distribution due to photometric uncertainty in the IRAC bands. The lower error bar indicates the intrinsic scatter, as calculated from the observed scatter and the simulated IRAC uncertainties. *Bottom panel:* The predicted [3.6]–[4.5] color distribution (orange histogram) using the [OIII] and $\text{H}\beta$ EWs as measured by Schenker et al. (2013b) and Holden et al. (2014) in $z \sim 3$ LBGs with the MOSFIRE spectrograph. We predict the [3.6]–[4.5] color assuming Case B recombination and a flat continuum in f_ν . Evolution of the EW strength as a function of redshift (e.g., Smit et al., 2014) will broaden the [3.6]–[4.5] color distribution and at the same time shift the median color of the distribution to bluer values as indicated by the left black arrow on the panel. The right black arrow indicates the shift in [3.6]–[4.5] color when we assume a somewhat more evolved stellar population with an age of 290 Myr and a dust content of $E(B - V) = 0.15$ (see §4.4.2 for details).



4.4.2 Blue [3.6]–[4.5] sources at $z \sim 6.0$

In the previous section we showed that a large number of sources with ultra-blue [3.6]–[4.5] colors very likely have redshifts in the narrow range $6.6 - 6.9$, where the blue colors can be easily explained by the presence of [OIII] in the $3.6 \mu\text{m}$ band, in contrast to the $4.5 \mu\text{m}$ band that contains no strong line emission.

Figure 4.3 also shows a number of very blue [3.6]–[4.5] sources that prefer a redshift around $z \sim 6.0$ and that have a probability of less than $< 1\%$ of being at $z \sim 6.6 - 6.9$ (based on the photometric redshift probability distribution using only *HST* bands). In the redshift range $z \sim 5.4 - 6.6$, [OIII] still contaminates the $3.6 \mu\text{m}$ band, but the strong $\text{H}\alpha$ line also boosts the $4.5 \mu\text{m}$ flux. Both lines are expected to be strong in young, actively star-forming galaxies, and therefore it is unclear what the explanation is for the significant spread in [3.6]–[4.5] colors and in particular the very blue [3.6]–[4.5] colors observed for a small fraction of the population. While galaxies containing Active Galactic Nuclei (AGN) can exhibit extremely high [OIII]/ $\text{H}\beta$ ratios, this phenomenon is rare in local galaxies with stellar masses below $M_* < 10^{10} M_\odot$ (e.g., Juneau et al., 2013). For our sample of star-forming galaxies at $z \sim 6.0$, with UV-luminosities ranging from $M_{\text{UV}} \sim -19$ to $M_{\text{UV}} \sim -21$, we expect nearly all sources to have stellar masses below this limit (e.g., González et al., 2011; Salmon et al., 2014). However, we cannot completely rule out this option based on the limited photometric information available for these sources.

Figure 4.5 shows two examples of sources that are at $z < 6.6$ at high confidence. One source has an IRAC color of $[3.6] - [4.5] = -1.0 \pm 0.4$ but a photometric redshift of $5.84^{+0.25}_{-0.30}$; the

other source has an IRAC color of $[3.6] - [4.5] = -1.0 \pm 0.3$ but a photometric redshift of $5.97_{-0.22}^{+0.22}$. In both cases, we clearly cannot use the IRAC colors alone to distinguish between these sources and the sources from Figure 4.4, which strongly prefer a redshift around $z \sim 6.8$.

One effect that could influence our estimated photometric redshifts for these objects – and possibly offer an explanation for their blue $[3.6] - [4.5]$ colors – is the presence of high EW Ly α emission in these galaxies. For example Schenker et al. (2014) show that a 160Å EW Ly α line can cause the photometric redshift of a $z \sim 7.5$ galaxy to be underestimated by as much as $\Delta z = 0.2$, suggesting that our blue $z \sim 6.0$ sample may actually be at higher redshift. Though our templates do not include strong Ly α lines, searches for Ly α have shown a low abundance of Ly α emission at $z > 6.5$ (Pentericci et al., 2011; Treu et al., 2013; Finkelstein et al., 2013; Caruana et al., 2014; Schenker et al., 2014), and even at lower redshifts high-EW Ly α is rarely detected in UV bright ($M_{UV} < -20$) galaxies (e.g. Stark et al., 2010). Therefore it seems unlikely to suppose that these blue sources with $z_{phot} \sim 6.0$ are actually $z \sim 6.8$ galaxies with strong Ly α emission.

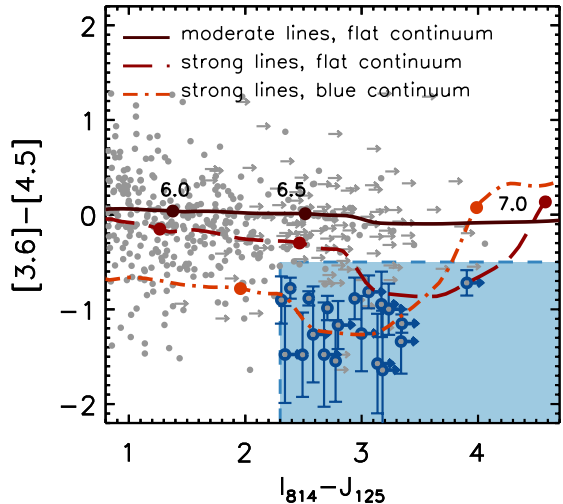
In order to understand the origin of these extreme IRAC colors at $z \sim 6.0$ we compare the $[3.6] - [4.5]$ color distribution of these sources with the colors we would predict based on a sample of $z \sim 3$ galaxies with near-IR spectroscopy in Figure 4.6. In the top panel of Figure 4.6 we show the sub-sample of sources that (with 68% confidence) have a redshift in the range $z \sim 5.4 - 6.6$, where [OIII] emission contaminates the 3.6 μm band while at the same time H α emission contaminates the 4.5 μm band (see the top panel of Figure 4.1). In the bottom panel of Figure 4.6 we show a prediction of the $[3.6] - [4.5]$ color distribution from the spectroscopic properties of [OIII] and H β in $z \sim 3$ LBGs as listed by Schenker et al. (2013b) and Holden et al. (2014). These authors find line ratios as high as $[\text{OIII}]\lambda 4959, 5007 \text{ \AA} / \text{H}\beta \sim 10$. This strong [OIII] flux with respect to the hydrogen Balmer lines could result in very blue $[3.6] - [4.5]$ colors if similar sources are present at $z \sim 6$. We computed the predicted $[3.6] - [4.5]$ colors from the observed $[\text{OIII}]\lambda 4959, 5007 \text{ \AA}$ EW and an estimate of the H α EW derived from the H β EW, assuming case B recombination and a flat continuum in f_ν . For $([3.6] - [4.5])_{\text{continuum}} = 0$ and assuming all sources are at $z = 6$, the [OIII] and H β EWs allow for a direct calculation of the $[3.6] - [4.5]$ colors such as shown in the bottom panel of Figure 4.6.

The spread in colors in the predicted distribution is smaller than the spread in the observed distribution at $z \sim 6.0$. Even when accounting for the spread in $[3.6] - [4.5]$ due to the observational uncertainties in the IRAC bands, the intrinsic spread exceeds the width of the predicted distribution (see the error bars in the top panel of Figure 4.6). However, this is likely explained by the spread in the color of the underlying continuum emission due to different dust content and ages of the galaxies in the observed distribution, while we assumed a fixed flat continuum in f_ν for our predicted colors. A somewhat evolved population (~ 300 Myr) and modest dust content ($E(B - V) \sim 0.15$) could redden the IRAC color of some of the observed galaxies by $\Delta([3.6] - [4.5]) \sim 0.2$ (see Figure 4.6). Similarly, the $[3.6] - [4.5]$ color of the continuum can be as blue as -0.4 mag for a very young ($\lesssim 10$ Myr) and dust-free galaxy.

Another effect that can change the predicted $[3.6] - [4.5]$ color distribution is a probable evolution of the emission line EWs between $z \sim 3$ and $z \sim 6$, e.g., because we are observing increasingly younger generations of galaxies. Assuming all line EWs follow the evolution of the H α EW derived by Fumagalli et al. (2012) for star-forming galaxies in the redshift range $z \sim 0 - 2$, the predicted spread in $[3.6] - [4.5]$ color would increase, while the median predicted $[3.6] - [4.5]$ color would be bluer by $\Delta([3.6] - [4.5]) = 0.23$.

From the above comparison we conclude that the blue $[3.6] - [4.5]$ sources at $z \sim 6.0$ (in-

Figure 4.7: Color-color diagram showing the selection criteria for our fiducial $z \sim 6.8$ sample (blue shaded region) with the color measurements of galaxies from our base as sample of $z \sim 5 - 8$ galaxies over all five CANDELS fields (grey points and arrows; non-detections in the I_{814} band are placed at the 1σ upper limit). The blue encircled points indicate the 20 selected sources listed in Table 4.1, that satisfy our blue IRAC criterion (Eq. 4.2) as well as a $I_{814} - J_{125} > 2.3$ (see §4.5) criterion (Sources that have large uncertainties in the IRAC color are not selected). The solid lines indicate tracks for three different galaxy templates as described in Figure 4.3, with the solid points indicating the colors of the templates at $z = [6.0, 6.5, 7.0]$.



indicated with the blue histogram in the top panel of Figure 4.6) can be explained by the high $[\text{OIII}]/\text{H}\beta$ values observed in $z \sim 3$ LBGs and a blue continuum $[3.6] - [4.5]$ color as seen in young galaxies with low dust content and low metallicity, possibly in combination with an evolving EW strength of nebular emission lines as a function of redshift.

4.5 A fiducial sample of $z \sim 6.8$ emission line galaxies

In this section we will present a strategy for the efficient use of *HST*+IRAC information to select galaxies over the redshift range $z \sim 6.6 - 6.9$. In §4.4.1 we showed that sources at $z \sim 6.6 - 6.9$ have very blue $[3.6] - [4.5]$ colors and that we can use this information to significantly reduce the uncertainty on the redshift determination. However, we also found that a small number of galaxies at $z < 6.6$ show extremely blue colors as well and we cannot distinguish these sources from galaxies in the redshift range $z \sim 6.6 - 6.9$ on the basis of the $[3.6] - [4.5]$ IRAC colors alone.

4.5.1 Selection of our fiducial $z \sim 6.8$ sample

To effectively exclude $z \sim 6$ galaxies from our selection of galaxies in the narrow redshift range $z \sim 6.6 - 6.9$, we require an additional selection criterion besides our $[3.6] - [4.5]$ color cut (Eq. 4.2). For our fiducial sample we require that sources show a significant break across the I_{814} and J_{125} bands:

$$I_{814} - J_{125} > 2.3 \quad (4.3)$$

If I_{814} is undetected we use the 1σ upper limit to compute the color. This dropout criterion should effectively exclude the $z < 6.5$ contaminating galaxies from our target $z \sim 6.8$ selection (see Figure 4.7). We will separately select $z \sim 6$ ultra-blue galaxies using a $I_{814} - J_{125} < 2.3$ criterion.

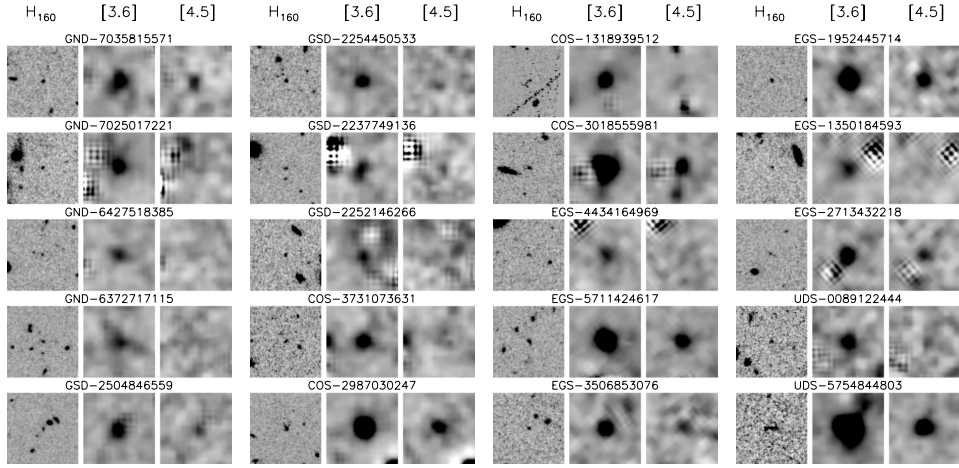


Figure 4.8: *HST* H_{160} , *Spitzer/IRAC* 3.6 μm , and 4.5 μm band postage stamp negative images ($8''4 \times 8''4$) of our fiducial sample of galaxies at $z \sim 6.8$ in the CANDELS fields with extremely blue [3.6]–[4.5] IRAC colors (satisfying Eq. 4.2) and $I_{814} - J_{125} > 2.3$ (see §4.5). The IRAC postage stamps have been cleaned for contamination from neighboring sources (see §4.2.2). Properties of the sources are listed in Table 4.1.

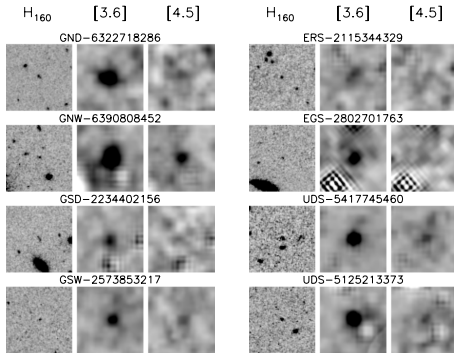


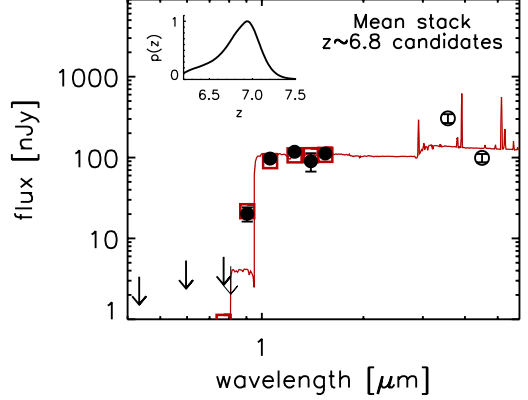
Figure 4.9: *HST* H_{160} , *Spitzer/IRAC* 3.6 μm , and 4.5 μm band postage stamp negative images ($8''4 \times 8''4$) of our sample of galaxies at $z \sim 6.0$ in the CANDELS fields with extremely blue [3.6]–[4.5] IRAC colors (satisfying Eq. 4.2) and $I_{814} - J_{125} < 2.3$ (see §4.5). The IRAC postage stamps have been cleaned for contamination from neighboring sources (see §4.2.2). Properties of the sources are listed in Table 4.1.

We apply the criteria given by Eq. 4.2 and Eq. 4.3 to our photometric catalogs of sources in all five CANDELS fields (Bouwens et al., 2014b) and find 20 sources in our fiducial $z \sim 6.8$ sample and 8 sources that are likely at lower redshift. We summarize the properties of the fiducial sample and the sources that satisfy Eq. 4.2 but not Eq. 4.3 in Table 4.1, and we show postage stamps of the sources in Figures 4.8 and 4.9. The typical width of the 68% redshift confidence intervals for the sources in our fiducial sample as given by $P(z_{\text{phot}, HST+IRAC})$ is $\Delta z = 0.2$.

4.5.2 Ascertaining the mean redshift and contamination fraction of the $z \sim 6.8$ sample

To test the robustness of our selection we stacked the sources from GOODS-N/S selected by Eq. 4.2 and 4.3 and we show the resulting spectral energy distribution (SED) in Figure 4.10. We estimate the mean redshift for our selected sources from the stacked photometry. We emphasize

Figure 4.10: Template fit to the stacked broadband observations of blue $[3.6] - [4.5]$ galaxies (Eq. 4.2) that also satisfy $I_{814} - J_{125} > 2.3$ (see §4.5). Fluxes and upper limits (black points and thick arrows) show the mean *HST* photometry (error bars obtained from bootstrapping). We do not include the stacked I_{814} , $3.6 \mu\text{m}$ and $4.5 \mu\text{m}$ band flux measurements (indicated by the thin arrow and open black points) in this analysis in order to avoid biasing our photometric redshift due to our use of the $I_{814} - J_{125}$ and $[3.6] - [4.5]$ colors in selecting the sources. The inset panel shows the probability distribution on the mean redshift for our sample. This distribution has a mean value of $z_{\text{phot}} = 6.81^{+0.25}_{-0.28}$, consistent with the desired redshift range for our selection.



that we do not use our flux measurements in the I_{814} , $3.6 \mu\text{m}$ and $4.5 \mu\text{m}$ bands, due to flux measurements in these bands playing an important role in the selection of the sources themselves; this should ensure that our derived redshift is not significantly biased by the selection process itself. We find a photometric redshift of $z_{\text{phot}} = 6.81^{+0.25}_{-0.28}$, consistent with the redshift range $z \sim 6.6 - 6.9$. Since the measured flux in the J_{125} band was also used in the selection of individual sources, it could have a minor effect on the estimated redshift for the stacked photometry. Excluding the J_{125} -band flux measurements in deriving the best-fit redshift, gives a photometric redshift of $z_{\text{phot}} = 6.77 \pm 0.31$.

As a test of the robustness of our blue IRAC selection criterion (Eq. 4.2) against scatter in the $[3.6] - [4.5]$ color due to the uncertainties in the $3.6 \mu\text{m}$ and $4.5 \mu\text{m}$ flux measurements, we simulated the photometric scatter assuming an intrinsic IRAC color $[3.6] - [4.5] = 0$ for all sources from the five CANDELS fields in our $z \sim 5 - 8$ base sample. We simulated the observed colors by adding noise to the $3.6 \mu\text{m}$ and $4.5 \mu\text{m}$ -band fluxes, that match the measured flux uncertainties ($1000\times$ per source). From this simulation we conclude that less than 0.1 source with an intrinsic IRAC color $[3.6] - [4.5] = 0$ has scattered into our fiducial selection over all five CANDELS fields.

The only significant source of interlopers to our fiducial sample of $z \sim 6.8$ galaxies would seem to arise from galaxies at $z < 6.6$. To quantify this interloper fraction, we first estimate the fraction of ultra-blue $[3.6] - [4.5]$ sources at $z < 6.6$ from Figure 4.6, which is 6%. From the bottom panel of Figure 4.3 (see also Table 4.1) we find that sources in our fiducial sample have estimated redshifts as far as $\Delta z \sim 0.3$ away from our desired redshift range $z \sim 6.6 - 6.9$. We therefore assume that $z \sim 6.3 - 6.6$ galaxies cannot be completely removed from our fiducial sample using our $I_{814} - J_{125} < 2.3$ color criterion (Eq. 4.3) and could potentially be contaminating our $z \sim 6.8$ sample. Multiplying those sources from our base sample of galaxies from all five CANDELS fields (§4.2.3) with $z_{\text{phot},HST} \sim 6.3 - 6.6$ by the 6% fraction with ultra-blue IRAC colors, we estimate that ~ 2.0 sources could have scattered into our fiducial $z \sim 6.8$ sample from $z < 6.6$. We therefore conservatively estimate that $\sim 90\%$ of the 20 sources with extreme IRAC colors and $I_{814} - J_{125}$ colors > 2.3 (Table 4.1) lie in the redshift range $z \sim 6.6 - 6.9$.

Furthermore, comparing the 20 galaxies from our $z \sim 6.8$, IRAC ultra-blue sample (90%

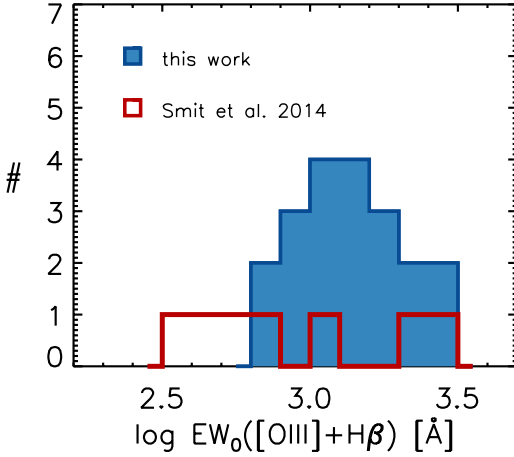


Figure 4.11: The rest-frame EW distribution of [OIII]+H β (blue filled histogram), estimated from the sources in our $z \sim 6.8$ sample (see §4.5.3). For reference we show the EWs of the sources from Smit et al. (2014) that were selected on their photometric redshift being in the range $z \sim 6.6 - 7.0$ (red histogram). In §4.5.2 we calculated that our fiducial sample roughly selects the $\sim 50\%$ strongest line emitters at $z \sim 6.8$. The observed median of the distribution is 1375 Å rest-frame EW, but correcting for the bias in the measurement due to scatter in the [3.6]–[4.5] color (for details see §4.5.3) we estimate a median $\text{EW}_0([\text{OIII}]+\text{H}\beta)$ of 1085 Å. The excellent agreement between our sample and the 50% most extreme sources from Smit et al. (2014) provides further evidence that high-EW nebular emission lines are indeed ubiquitous at high redshift.

of which we estimated to lie in this redshift range: see previous paragraph) with the 35 galaxies estimated to lie in the redshift range $z \sim 6.6 - 6.9$ from the redshifts of our $z \sim 5 - 8$ base sample, we estimate that $\sim 50\%$ of all sources at $z \sim 6.8$ exhibit ultra-blue colors (vs. 6% at $z \sim 6$). This makes IRAC ultra-blue sources roughly ~ 8 times more common at $z \sim 6.8$ than at $z < 6.6$. This is useful to establish, since it indicates that ultra-blue IRAC criteria - such as we propose - reduce the numbers of contaminants in our samples significantly, i.e., improving the purity of $z \sim 6.6 - 6.9$ selections by a factor of 8 over what one would manage using *HST* and ground-based observations alone.

4.5.3 Quantifying the rest-frame EWs of [OIII]+H β in our $z \sim 6.8$ IRAC ultra-blue sample

Using the assumption that the 4.5 μm band is free of emission line contamination at $z \sim 6.6 - 6.9$ while the 3.6 μm band is contaminated by [OIII] and H β , we can make a prediction of the [OIII] strength and estimate the fraction of high-EW [OIII] emitters in the high redshift galaxy population. The median [3.6]–[4.5] color of our $z \sim 6.8$ sample is -1.2 ± 0.3 , indicating a typical rest-frame $\text{EW}_0([\text{OIII}]+\text{H}\beta) > 1000$ Å (see Smit et al., 2014).

In order to obtain a more accurate estimate of the [OIII] EW, we calculated the difference between the contaminated 3.6 μm flux and an estimate of the rest-frame optical continuum flux. The continuum flux was estimated by fitting the SEDs of the galaxies with stellar population templates using the Fitting and Assessment of Synthetic Templates (FAST) code (Kriek et al., 2009). In the fitting procedure we used stellar population templates by Bruzual & Charlot (2003) and constant star formation histories with ages between 30 Myr and the age of the Universe at $z = 6.6$. We assumed a Salpeter (1955) IMF with limits 0.1–100 M_\odot and a Calzetti et al. (2000) dust law. We considered dust contents between $A_V = 0 - 1.5$ and subsolar metallicities between 0.2 and 0.4 Z_\odot . We only considered the *HST* and the 4.5 μm IRAC photometry in deriving our best-fit model, while excluding the measured 3.6 μm fluxes (due to their being impacted by the [OIII]+H β lines). We used the best fit templates from our fitting procedure to obtain an estimate of the 3.6 μm continuum flux and from this we derived the rest-frame EW of the combined

[OIII] λ 4959,5007 Å+H β lines.

Our estimates of rest-frame $EW_0([\text{OIII}]+\text{H}\beta)$ are listed in table 4.1 and range from ~ 900 Å to > 2000 Å with a median of 1375 Å. Though the uncertainties on the EWs are too large for the > 2000 Å EW measurements to be secure, we estimate rest-frame EWs as high as $\gtrsim 1000$ Å in the majority of our selected sources. Nevertheless, we note that the median EW we derive here will be biased towards high values because we are using the same [3.6]–[4.5] color measurements to derive the EWs as we used for the selection. We estimate this bias by investigating the selection process in a distribution of galaxies with an intrinsic IRAC color [3.6]–[4.5] = 0 and simulated the noise in the 3.6 μm and 4.5 μm bands based on the measured flux uncertainties. We selected 50% of the sources with the bluest simulated [3.6]–[4.5] colors (in agreement with our estimates in §4.5.2) and found these sources have a median [3.6]–[4.5] = -0.15 . Using this color bias and eq. 1 and 2 from Smit et al. (2014) and assuming a flat continuum in f_ν for these sources, we estimate an observed bias of ~ 290 Å on the measured [OIII]+H β EW of 1375 Å due to the noise in the IRAC bands. This suggests that the median EW of our selected sources is really 1085 Å in the noise-free case.

We show the predicted $EW_0([\text{OIII}]+\text{H}\beta)$ distribution of our $z \sim 6.8$ sample in Figure 4.11. We compare this distribution with the EW distribution from the seven lensed sources selected in the redshift range $z \sim 6.6 - 7.0$ reported by Smit et al. (2014) and comparable intrinsic UV luminosities. We use the same procedure to derive EWs for these sources as described in the paragraph above. For one source we use the 1σ upper limit due to the high uncertainties in the IRAC photometry. The comparison between the two distributions confirms that our suggested criteria for selecting $z \sim 6.8$ sources roughly selects the $\sim 50\%$ most extreme line emitters at that redshift.

The median UV luminosity of our sample (computed from the H_{160} -band fluxes and assuming $z = 6.75$) is $M_{\text{UV}} = -20.66$, roughly comparable to the $M_{\text{UV}}^* = -20.87 \pm 0.26$ from the $z \sim 7$ luminosity function derived by Bouwens et al. (2014b). Combining this information with our calculation in §4.5.2 we argue that roughly $\sim 50\%$ of the M_{UV}^* galaxy population at $z \sim 7$ produces extreme nebular emission lines ($EW_0([\text{OIII}]+\text{H}\beta) \gtrsim 1000$ Å) in the rest-frame optical.

It is interesting to compare these derived EWs to the observed [OIII]+H β EW distribution at $z \sim 3$ reported by Schenker et al. (2013b) and Holden et al. (2014). In order to match our $z \sim 6.8$ sample, we use only the 50% most extreme emitters from the combined Schenker et al. (2013b) and Holden et al. (2014) samples and calculate a median $EW_0([\text{OIII}]+\text{H}\beta) = 390$ Å (with a median redshift $z \sim 3.5$). Comparing this number to the mean EW at $z \sim 6.8$ and assuming the evolution of nebular emission line EWs scales as $\sim (1+z)^n$ (see Fumagalli et al., 2012), we derive $EW_0([\text{OIII}]+\text{H}\beta) \propto (1+z)^{1.9 \pm 0.36}$. This slope is consistent with the slope derived by Fumagalli et al. (2012) for H α EWs over the redshift range $z \sim 0 - 2$ ($n \sim 1.8$) but somewhat steeper than the slope derived by Labbé et al. (2013), who found $n = 1.2 \pm 0.25$ over the redshift range $z \sim 1 - 8$.

4.6 Summary and discussion

In this chapter we explore the use of IRAC colors to select star-forming galaxies in the narrow redshift range $z \sim 6.6 - 6.9$. Sources in this redshift range are expected to be very blue due to the boosted flux in the 3.6 μm band from high-EW [OIII] emission, while the 4.5 μm band is free

from contamination of strong nebular emission lines. This suggests a blue IRAC criterion may be appropriate for selecting galaxies in the redshift range $z \sim 6.6 - 6.9$.

In evaluating the suitability of such a selection criterion we analyze a large sample of Lyman Break galaxies in GOODS-N and GOODS-S with relatively high S/N Spitzer/IRAC coverage from the Spitzer GOODS, ERS, and S-CANDELS programs (Ashby et al., submitted). We find that the majority of candidates with extremely blue [3.6]–[4.5] colors are consistent with $z \sim 6.8$. In addition to the $z \sim 6.6 - 6.9$ sources, we also find a small number of sources with extreme [3.6]–[4.5] colors more likely to be at $z \sim 6.0$. The blue [3.6]–[4.5] galaxies at $z \sim 6.0$ can be explained by high [OIII]/ $H\beta$ ratios, such as found in $z \sim 3$ LBGs (Schenker et al., 2013b; Holden et al., 2014), lensed galaxies at $z \sim 1 - 2$ (Brammer et al., 2012b; van der Wel et al., 2013), and in Green Pea galaxies at $z \sim 0$ (Amorín et al., 2012; Jaskot & Oey, 2013) in combination with blue colors for the optical continuum.

To obtain a clear selection in the redshift range $z \sim 6.6 - 6.9$, we suggest the use of ultra-blue IRAC colors combined with an $I_{814} - J_{125} > 2.3$ dropout criterion. Based on our analysis in section §4.5, we estimate that at least 90% of the sources selected by these criteria lie in the redshift range $z \sim 6.6 - 6.9$. We systematically apply such criteria to our source catalogs from the five CANDELS fields (720 arcmin²) and find 20 sources (~ 0.03 arcmin⁻²). A comparison with the total number of galaxies from our catalogs in this redshift range suggests that we select the $\sim 50\%$ bluest IRAC sources at $z \sim 6.8$ at a typical UV-luminosity $M_{UV} \sim M_{UV,z=7}^*$.

We estimate a median uncertainty on the redshift estimates for our fiducial sources of $\Delta z = 0.2$ (68% confidence). Such redshift uncertainties are significantly smaller than one finds for these objects without the inclusion of the IRAC fluxes. For example, we find a median 68% confidence interval on $z_{\text{phot,HST}}$ of $\Delta z = 0.6$ and $\Delta z = 1.7$, respectively, for sources in GOODS-N/S and COSMOS/EGS/UDS. Among other uses, such tight constraints on the redshifts are necessary for efficient observations with ALMA. Our constraints on the redshift of these sources means that we should typically only require two ALMA tunings to successfully observe [CII] $\lambda 157.7 \mu\text{m}$ in band 6.

Using our fiducial sample of $z \sim 6.8$ sources with ultra-blue [3.6]–[4.5] colors, we estimate the strength of [OIII] $\lambda 4959, 5007 \text{ \AA} + H\beta$ from the contaminated $3.6 \mu\text{m}$ flux. We find that the majority of the sources in our sample show EWs as high as $\text{EW}_0([\text{OIII}] + H\beta) \gtrsim 1000 \text{ \AA}$, in excellent agreement with the $\sim 50\%$ most extreme sources from Smit et al. (2014).

Given the recent study by Stark et al. (2014a), who found evidence for strong [OIII] $\lambda\lambda 4959, 5007 \text{ \AA}$ emission in sources with high-EW CIII] $\lambda 1908 \text{ \AA}$ lines at $z \sim 2$, it seems reasonable to suppose that our strong [OIII] emitters also exhibit relatively strong CIII] lines, and therefore our sources are excellent targets for follow-up studies with near-IR spectroscopy (e.g. Stark et al., 2014b).

Finally, with the future launch of the *JWST*, we will be able to target these extreme line-emitter galaxies with *JWST*'s near infrared spectrograph (NIRSpec). The [OIII] $\lambda 5007 \text{ \AA}$ line in a typical galaxy from our sample should be detected at 10σ in the *JWST*/NIRSpec $R = 100$ mode with a mere 60 second exposure.

Acknowledgements

We thank Jarle Brinchmann, Rob Crain, Paul van der Werf and Tim van Kempen for useful discussions. We are grateful to Brad Holden for providing us with the complete catalog from

Holden et al. (2014). We thank the anonymous referee of our chapter for valuable feedback on our manuscript. We acknowledge support from ERC grant HIGHZ #227749, and an NWO vrij competitie grant.

Table 4.1: Properties of extremely blue [3.6]–[4.5] galaxies in our samples

ID	RA	Dec	m_{H160}	$I_{814} - J_{125}$	[3.6]–[4.5]	$z_{\text{phot,HST}}^c$	$z_{\text{phot,HST+IRAC}}^c$	EW _{[OIII]+Hβ}
Fiducial $z \sim 6.8$ sample ^a								
GND-7035815571	12:37:03.586	+62:15:57.18	26.3 ± 0.1	> 3.2	-1.0 ± 0.3	$7.26^{+0.33}_{-0.34}$	$6.81^{+0.07}_{-0.07}$	1374 ± 415
GND-7025017221	12:37:02.500	+62:17:22.17	26.8 ± 0.1	> 2.8	-1.2 ± 0.3	$7.25^{+0.33}_{-0.45}$	$6.76^{+0.07}_{-0.06}$	1779 ± 486
GND-6427518385	12:36:42.753	+62:18:38.55	27.0 ± 0.2	2.5 ± 0.9	-1.5 ± 0.4	$6.52^{+0.37}_{-0.37}$	$6.71^{+0.08}_{-0.06}$	2591 ± 1095
GND-6372717115	12:36:37.279	+62:17:11.59	26.3 ± 0.1	> 3.2	-0.9 ± 0.3	$6.75^{+0.27}_{-0.26}$	$6.70^{+0.13}_{-0.12}$	1193 ± 485
GSD-2504846559 ^d	03:32:50.481	-27:46:55.95	25.8 ± 0.1	2.3 ± 0.9	-0.9 ± 0.2	$6.83^{+0.32}_{-0.34}$	$6.78^{+0.08}_{-0.08}$	962 ± 293
GSD-2254450533	03:32:25.443	-27:50:53.36	26.3 ± 0.1	> 3.3	-1.3 ± 0.3	$6.96^{+0.26}_{-0.23}$	$6.78^{+0.06}_{-0.06}$	1471 ± 432
GSD-2237749136	03:32:23.778	-27:49:13.64	26.6 ± 0.1	> 3.0	-1.3 ± 0.4	$6.90^{+0.20}_{-0.19}$	$6.74^{+0.09}_{-0.09}$	1800 ± 704
GSD-2252146266 ^e	03:32:25.216	-27:46:26.69	26.9 ± 0.1	> 3.1	-1.6 ± 0.5	$6.94^{+0.23}_{-0.23}$	$6.75^{+0.06}_{-0.06}$	2424 ± 1083
COS-3731073631	10:00:37.310	+02:27:36.31	26.0 ± 0.1	> 2.3	-1.5 ± 0.5	$7.43^{+1.07}_{-1.23}$	$6.68^{+0.14}_{-0.14}$	1686 ± 676
COS-2987030247 ^d	10:00:29.870	+02:13:02.47	24.8 ± 0.1	2.7 ± 0.8	-1.0 ± 0.1	$6.99^{+1.23}_{-1.25}$	$6.66^{+0.14}_{-0.14}$	1128 ± 166
COS-1318939512 ^e	10:00:13.189	+02:23:9.512	25.0 ± 0.1^e	2.8 ± 1.0	-1.5 ± 0.4	$7.18^{+1.07}_{-0.89}$	$6.75^{+0.09}_{-0.08}$	786 ± 301
COS-3018555981 ^f	10:00:30.185	+02:15:59.81	24.9 ± 0.1	> 3.3	-1.2 ± 0.1	$7.76^{+0.79}_{-0.82}$	$6.76^{+0.07}_{-0.07}$	1424 ± 143
EGS-4434164969	14:19:44.341	+52:56:49.69	26.3 ± 0.1	> 2.6	-1.3 ± 0.5	$7.08^{+1.22}_{-1.41}$	$6.62^{+0.20}_{-0.20}$	1321 ± 619
EGS-5711424617	14:19:57.114	+52:52:46.17	25.1 ± 0.1	2.4 ± 0.2	-0.8 ± 0.1	$6.33^{+0.22}_{-0.22}$	$6.47^{+0.10}_{-0.10}$	927 ± 149
EGS-3506853076 ^g	14:19:35.068	+52:55:30.76	26.2 ± 0.1	2.9 ± 0.9	-0.9 ± 0.2	$7.18^{+0.51}_{-0.82}$	$6.62^{+0.10}_{-0.16}$	1084 ± 298
EGS-1952445714 ^h	14:19:19.524	+52:44:57.14	25.3 ± 0.1	> 3.9	-0.7 ± 0.1	$7.52^{+0.66}_{-0.66}$	$6.75^{+0.11}_{-0.11}$	768 ± 151
EGS-1350184593 ⁱ	14:19:13.501	+52:48:45.93	26.5 ± 0.1	> 3.2	-1.6 ± 0.6	$7.56^{+0.71}_{-0.74}$	$6.72^{+0.09}_{-0.08}$	2391 ± 1196
EGS-2713432218	14:19:27.134	+52:53:22.18	26.1 ± 0.1	> 3.1	-0.8 ± 0.2	$7.56^{+0.66}_{-0.68}$	$6.71^{+0.13}_{-0.14}$	1048 ± 242
UDS-0089122444	02:17:00.891	-05:12:24.44	26.5 ± 0.2	> 2.7	-1.5 ± 0.6	$7.34^{+0.83}_{-0.87}$	$6.70^{+0.11}_{-0.10}$	2620 ± 1350
UDS-5754844803 ^j	02:17:57.548	-05:08:44.80	24.8 ± 0.2	2.5 ± 1.1	-0.9 ± 0.1	$7.05^{+1.08}_{-1.28}$	$6.61^{+0.19}_{-0.17}$	915 ± 95
$z \sim 6.0$ sample ^b								
GND-6322718286	12:36:32.273	+62:18:28.67	26.2 ± 0.1	2.0 ± 0.4	-1.1 ± 0.3	$7.01^{+0.23}_{-0.24}$	$6.75^{+0.08j}_{-0.09}$	–
GNW-6390808452	12:36:39.080	+62:08:45.29	26.1 ± 0.2	2.1 ± 0.8	-0.7 ± 0.1	$5.87^{+0.33}_{-0.33}$	$4.84^{+1.50k}_{-0.03}$	–
GSD-2234402156	03:32:23.449	-27:50:21.56	26.5 ± 0.1	1.5 ± 0.3	-1.0 ± 0.3	$5.97^{+0.22}_{-0.22}$	$6.09^{+0.13k}_{-0.12}$	–
GSW-2573853217	03:32:57.381	-27:53:21.78	26.2 ± 0.2	> 1.7	-0.8 ± 0.2	$6.27^{+0.25}_{-0.26}$	$6.46^{+0.13k}_{-0.13}$	–
ERS-2115344329	03:32:11.539	-27:44:32.99	26.9 ± 0.1	1.1 ± 0.2	-1.0 ± 0.4	$5.84^{+0.25}_{-0.30}$	$6.03^{+0.12k}_{-0.12}$	–
EGS-2802701763	14:20:28.027	+53:00:17.63	26.5 ± 0.2	1.1 ± 0.3	-1.4 ± 0.5	$5.48^{+0.54}_{-0.84}$	$5.94^{+0.14k}_{-0.24}$	–
UDS-5417745460	02:17:54.177	-05:14:54.60	25.5 ± 0.1	2.2 ± 0.4	-0.7 ± 0.2	$6.32^{+0.29}_{-0.23}$	$6.45^{+0.18k}_{-0.19}$	–
UDS-5125213373	02:17:51.252	-05:11:33.73	25.6 ± 0.1	1.8 ± 0.3	-0.9 ± 0.3	$6.01^{+0.34}_{-1.36}$	$6.25^{+0.14k}_{-0.15}$	–

^aIn addition to our blue IRAC criterion (see Eq. 4.2) we require $I_{814} - J_{125} > 2.3$ for our fiducial 6.6 – 6.9 sample. If I_{814} is undetected we use the 1σ upper limit to compute the color.

^bHere, we list sources with $I_{814} - J_{125} < 2.3$, as well as blue IRAC colors (satisfying Eq. 4.2). Low S/N sources cannot unambiguously be selected in the $z \sim 6.0$ sample, i.e., if they satisfy $I_{814} - J_{125} < 2.3 \wedge S/N(I_{814}) < 1$. However, this is only the case for one source in our sample, i.e. GSW-2573853217. The photometric redshift estimate of this source indicates it likely belongs in the $z \sim 6.0$ sample.

^cError bars indicate the 68% confidence interval.

^dIn the stacked ground-based optical image (inverse variance weighted) this source is detected at 7.9 ± 1.5 nJy. However, this flux appears to derive from a foreground source, close to our object of interest but distinctly separated in the HST optical images.

^eThis source is detected at the edge of the *HST*/WFC3 field of view. We have verified that this source is also detected in the ground-based photometry from the UltraVISTA survey (see Ilbert et al., 2013). However, the total magnitude for this source measured from ground-based data appears to be somewhat fainter than we measure for HST, suggesting that our HST stack might be affected by some non-gaussian noise.

^fThis source was independently discovered by Tilvi et al. (2013) and Bowler et al. (2014), who estimated a photometric redshift of $7.24^{+0.38}_{-0.25}$ and $6.77^{+0.14}_{-0.19}$ respectively.

^gThis source is only marginally resolved; while its spatial profile and SED are much more consistent with its being a $z \sim 6.8$ galaxy, we cannot completely exclude the possibility it is a low-mass star.

^hThough the size of this source is consistent with its being a low-mass star, the SED of this source is better fit by a high-redshift galaxy than a stellar template.

ⁱThis source, better known as ‘Himiko’ (Ouchi et al., 2009, 2013), has a spectroscopic redshift at $z_{Ly\alpha} = 6.59$, consistent with our photometric redshift estimate within the 68% probability window.

^jThis source is weakly detected in I_{814} with $I_{814} - J_{125} = 2.0 \pm 0.4$ and therefore included in the $z \sim 6$ sample. However, due to a $< 1\sigma$ detection in the z_{850} band, our estimated photometric redshift indicates a $z \sim 6.75$ solution.

^kThe typical uncertainty in $z_{\text{phot,HST+IRAC}}$ for this $z \sim 6$ sample is very small. The ultra-blue IRAC colors of these galaxies are preferentially fit by the template with the most extreme [OIII]/H α ratio, which allows for little variation of the colors of the continuum emission and thereby narrows the redshift probability distribution. However, the shape of the spectral energy distributions of these galaxies (and the range of [OIII]/H α ratios at $z \sim 6$) is unknown, and therefore it is likely that the width of the redshift probability distribution is underestimated for this particular sample.

^lThe $4.5\mu\text{m}$ images for these candidates require a modest ($\sim 50\%$) correction for contaminating flux from neighbouring sources. While we would expect the corrections we perform to be generally quite accurate, we flag these candidates as somewhat less robust than the other candidates in our sample.

References

- Amorín, R., Pérez-Montero, E., Vilchez, J. M., & Papaderos, P. 2012, *ApJ*, 749, 185
- Anders, P., & Fritze-v. Alvensleben, U. 2003, *A&A*, 401, 1063
- Ashby, M. L. N., Willner, S. P., Fazio, G. G., et al. 2013, *ApJ*, 769, 80
- Ashby, M. L. N., Willner, S. P., Fazio, et al. *ApJS*, submitted
- Beckwith, S. V. W., Stiaivelli, M., Koekemoer, A. M., et al. 2006, *AJ*, 132, 1729
- Bertin, E., & Arnouts, S. 1996, *A&AS*, 117, 393
- Bouwens, R. J., Illingworth, G. D., Franx, M., et al. 2009, *ApJ*, 705, 936
- Bouwens, R. J., Illingworth, G. D., Oesch, P. A., et al. 2011, *ApJ*, 737, 90
- Bouwens, R. J., Illingworth, G. D., Oesch, P. A., et al. 2012, *ApJ*, 754, 83
- Bouwens, R. J., Illingworth, G. D., Oesch, P. A., et al. 2013, *ApJ*, 793, 115
- Bouwens, R. J., Illingworth, G. D., Oesch, P. A., et al. 2014, *ApJ*, submitted, arXiv:1403.4295
- Bowler, R. A. A., Dunlop, J. S., McLure, R. J., et al. 2012, *MNRAS*, 426, 2772
- Bowler, R. A. A., Dunlop, J. S., McLure, R. J., et al. 2014, *MNRAS*, 440, 2810
- Bradley, L. D., Trenti, M., Oesch, P. A., et al. 2012, *ApJ*, 760, 108
- Brammer, G. B., van Dokkum, P. G., & Coppi, P. 2008, *ApJ*, 686, 1503
- Brammer, G. B., van Dokkum, P. G., Franx, M., et al. 2012a, *ApJS*, 200, 13
- Brammer, G. B., Sánchez-Janssen, R., Labbé, I., et al. 2012b, *ApJ*, 758, L17
- Bruzual, G., & Charlot, S. 2003, *MNRAS*, 344, 1000
- Capak, P., Aussel, H., Ajiki, M., et al. 2007, *ApJS*, 172, 99
- Carilli, C. L., & Walter, F. 2013, *ARA&A*, 51, 105
- Caruana, J., Bunker, A. J., Wilkins, S. M., et al. 2014, *MNRAS*, 443, 2831
- Coe, D., Benítez, N., Sánchez, S. F., et al. 2006, *AJ*, 132, 926
- Calzetti, D., Armus, L., Bohlin, R. C., et al. 2000, *ApJ*, 533, 682
- Curtis-Lake, E., McLure, R. J., Dunlop, J. S., et al. 2013, *MNRAS*, 429, 302
- Dunlop, J. S., McLure, R. J., Robertson, B. E., et al. 2012, *MNRAS*, 420, 901
- Dunlop, J. S., Rogers, A. B., McLure, R. J., et al. 2013, *MNRAS*, 432, 3520
- Ellis, R. S., McLure, R. J., Dunlop, J. S., et al. 2013, *ApJ*, 763, L7
- Eyles, L. P., Bunker, A. J., Stanway, E. R., et al. 2005, *MNRAS*, 364, 443
- Eyles, L. P., Bunker, A. J., Ellis, R. S., et al. 2007, *MNRAS*, 374, 910
- Finkelstein, S. L., Papovich, C., Salmon, B., et al. 2012, *ApJ*, 756, 164
- Finkelstein, S. L., Papovich, C., Dickinson, M., et al. 2013, *Nature*, 502, 524
- Fumagalli, M., Patel, S. G., Franx, M., et al. 2012, *ApJ*, 757, L22
- Furusawa, H., Kosugi, G., Akiyama, M., et al. 2008, *ApJS*, 176, 1
- González, V., Labbé, I., Bouwens, R. J., et al. 2010, *ApJ*, 713, 115
- González, V., Labbé, I., Bouwens, R. J., et al. 2011, *ApJ*, 735, L34
- González, V., Bouwens, R. J., Labbé, I., et al. 2012, *ApJ*, 755, 148
- González, V., Bouwens, R., Illingworth, G., et al. 2014, *ApJ*, 781, 34
- Grogin, N. A., Kocevski, D. D., Faber, S. M., et al. 2011, *ApJS*, 197, 35
- Holden, B. P., Oesch, P. A., Gonzalez, V. G., et al. 2014, *ApJ*, submitted, arXiv:1401.5490
- Holwerda, B. W., Trenti, M., Clarkson, W., et al. 2014, *ApJ*, 788, 77
- Ilbert, O., McCracken, H. J., Le Fèvre, O., et al. 2013, *A&A*, 556, A55
- Illingworth, G. D., Magee, D., Oesch, P. A., et al. 2013, *ApJS*, 209, 6
- Jaskot, A. E., & Oey, M. S. 2013, *ApJ*, 766, 91
- Juneau, S., Dickinson, M., Bournaud, F., et al. 2013, *ApJ*, 764, 176
- Kewley, L. J., Dopita, M. A., Leitherer, C., et al. 2013, *ApJ*, 774, 100

- Kirkpatrick, J. D., Cushing, M. C., Gelino, C. R., et al. 2011, *ApJS*, 197, 19
- Koekemoer, A. M., Faber, S. M., Ferguson, H. C., et al. 2011, *ApJS*, 197, 36
- Kotulla, R., Fritze, U., Weilbacher, P., & Anders, P. 2009, *MNRAS*, 396, 462
- Kriek, M., van Dokkum, P. G., Labbé, I., et al. 2009, *ApJ*, 700, 221
- Labbé, I., Bouwens, R., Illingworth, G. D., & Franx, M. 2006, *ApJ*, 649, L67
- Labbé, I., González, V., Bouwens, R. J., et al. 2010a, *ApJ*, 716, L103
- Labbé, I., González, V., Bouwens, R. J., et al. 2010b, *ApJ*, 708, L26
- Labbé, I., Oesch, P. A., Bouwens, R. J., et al. 2013, *ApJ*, 777, L19
- Laporte, N., Streblyanska, A., Clement, B., et al. 2014, *A&A*, 562, L8
- Lorenzoni, S., Bunker, A. J., Wilkins, S. M., et al. 2011, *MNRAS*, 414, 1455
- McLure, R. J., Dunlop, J. S., Bowler, R. A. A., et al. 2013, *MNRAS*, 432, 2696
- Oesch, P. A., Bouwens, R. J., Illingworth, G. D., et al. 2012, *ApJ*, 745, 110
- Oesch, P. A., Bouwens, R. J., Illingworth, G. D., et al. 2013, *ApJ*, 773, 75
- Oesch, P. A., Bouwens, R. J., Illingworth, G. D., et al. 2014, *ApJ*, 786, 108
- Oke, J. B., & Gunn, J. E. 1983, *ApJ*, 266, 713
- Ouchi, M., Ono, Y., Egami, E., et al. 2009, *ApJ*, 696, 1164
- Ouchi, M., Ellis, R., Ono, Y., et al. 2013, *ApJ*, 778, 102
- Pentericci, L., Fontana, A., Vanzella, E., et al. 2011, *ApJ*, 743, 132
- Salmon, B., Papovich, C., Finkelstein, S. L., et al. 2014, *ApJ*, submitted, arXiv:1407.6012
- Salpeter, E. E. 1955, *ApJ*, 121, 161
- Schaerer, D., & de Barros, S. 2009, *A&A*, 502, 423
- Schenker, M. A., Robertson, B. E., Ellis, R. S., et al. 2013a, *ApJ*, 768, 196
- Schenker, M. A., Ellis, R. S., Konidaris, N. P., & Stark, D. P. 2013b, *ApJ*, 777, 67
- Schenker, M. A., Ellis, R. S., Konidaris, N. P., & Stark, D. P. 2014, *ApJ*, 795, 20
- Shim, H., Chary, R.-R., Dickinson, M., et al. 2011, *ApJ*, 738, 69
- Sirianni, M., Jee, M. J., Benítez, N., et al. 2005, *PASP*, 117, 1049
- Skelton, R. E., Whitaker, K. E., Momcheva, I. G., et al. 2014, *ApJS*, 214, 24
- Smit, R., Bouwens, R. J., Labbé, I., et al. 2014, *ApJ*, 784, 58
- Stanway, E. R., McMahon, R. G., & Bunker, A. J. 2005, *MNRAS*, 359, 1184
- Stark, D. P., Ellis, R. S., Bunker, A., et al. 2009, *ApJ*, 697, 1493
- Stark, D. P., Ellis, R. S., Chiu, K., Ouchi, M., & Bunker, A. 2010, *MNRAS*, 408, 1628
- Stark, D. P., Schenker, M. A., Ellis, R., et al. 2013, *ApJ*, 763, 129
- Stark, D. P., Richard, J., Siana, B., et al. 2014, *MNRAS*, 445, 3200
- Stark, D. P., Richard, J., Charlot, S., et al. 2014, *MNRAS*, arXiv:1408.3649
- Steidel, C. C., Adelberger, K. L., Giavalisco, M., Dickinson, M., & Pettini, M. 1999, *ApJ*, 519, 1
- Steidel, C. C., Rudie, G. C., Strom, A. L., et al. 2014, *ApJ*, 795, 165
- Szalay, A. S., Connolly, A. J., & Szokoly, G. P. 1999, *AJ*, 117, 68
- Tilvi, V., Papovich, C., Tran, K.-V. H., et al. 2013, *ApJ*, 768, 56
- Treu, T., Schmidt, K. B., Trenti, M., Bradley, L. D., & Stiavelli, M. 2013, *ApJ*, 775, L29
- van der Wel, A., van de Ven, G., Maseda, M., et al. 2013, *ApJ*, 777, L17
- Vanzella, E., Fontana, A., Pentericci, L., et al. 2014, *A&A*, 569, AA78
- Wilkins, S. M., Bunker, A. J., Stanway, E., Lorenzoni, S., & Caruana, J. 2011, *MNRAS*, 417, 717
- Wilkins, S. M., Coulton, W., Caruana, J., et al. 2013, *MNRAS*, 435, 2885
- Windhorst, R. A., Cohen, S. H., Hathi, N. P., et al. 2011, *ApJS*, 193, 27
- Yabe, K., Ohta, K., Iwata, I., et al. 2009, *ApJ*, 693, 507
- Yan, H., Dickinson, M., Stern, D., et al. 2005, *ApJ*, 634, 109
- Yan, H., Dickinson, M., Giavalisco, M., et al. 2006, *ApJ*, 651, 24

5

On the Systematic Use of $H\alpha$ to Measure Star Formation Rates in $z \sim 4$ Galaxies: Understanding the Origin of High-EW Nebular Emission Lines

We take advantage of a large spectroscopic and photometric-redshift-selected sample of sources at $z = 3.8 - 5.0$ to study the $H\alpha$ properties of high redshift galaxies from ultra-deep *Spitzer*/IRAC observations. We use the offset in the $3.6 \mu\text{m}$ IRAC band to derive the $H\alpha$ flux and show that we can use this as a good star formation rate (SFR) indicator. Similar to Shim et al. (2011), we find a systematic offset in the $\text{SFR}_{H\alpha}/\text{SFR}_{UV+\beta}$ ratios from local relations. However, we cannot explain this offset by assuming extremely young ages, since the same offset appears to apply not simply to $\text{Ly}\alpha$ emitting galaxies (which dominate the Shim et al. 2011 samples) but also to the general high-redshift star-forming galaxy population. We show that we can resolve this discrepancy by assuming bluer intrinsic UV slopes (increasing the dust correction) and a changing shape of the ionizing spectrum for lower metallicity galaxies (increasing the $L_{H\alpha}/\text{SFR}$ ratio). With these assumptions we find a higher normalization of the star formation main sequence compared to recent SED-based determinations. Finally, we derive the SFR function at $z \sim 4 - 7$ and find a SFR density of the universe that does not decline from $z \sim 2$ to $z \sim 4$. These findings demonstrate the importance of new facilities like ALMA for elucidating the dust-obscured star formation in high-redshift UV-selected samples if we are to understand the star formation history of the Universe.

5.1 Introduction

Over the last decade, dedicated deep field programs with the *Hubble Space Telescope* (*HST*) have identified more than 10000 candidate galaxies with a redshift beyond $z \gtrsim 4$, based on their photometric colors (e.g. Bouwens et al., 2014b). Although a number of these objects have been successfully confirmed out the $z \sim 7.5$ through near-infrared (NIR) spectroscopy (e.g. Finkelstein et al., 2013), the progress in characterizing the spectral energy distributions (SEDs) of these galaxies and identifying their physical properties has been slow. This is largely due to the fact that spectroscopy and deep, high-resolution photometry in the rest-frame optical wavelengths, shifted to observed mid-infrared (MIR) wavelengths for sources at $z \gtrsim 4$, will not be available until the launch of the *James Webb Space Telescope* (*JWST*).

Despite these challenges a number of notable results have emerged on the observational properties of the $z \gtrsim 4$ galaxy population. First of all, the typical rest-frame UV colors of galaxies from $z \sim 4$ to $z \sim 8$ have been meticulously characterized through their *HST* photometry (Bouwens et al., 2009, 2012, 2014a; Dunlop et al., 2012, 2013; Wilkins et al., 2011; Finkelstein et al., 2012). Furthermore, photometric studies using the *Spitzer Space Telescope* have obtained the first constraints on the shape of the rest-frame optical SED of $z \gtrsim 4$ galaxies (Eyles et al., 2005; Verma et al., 2007; Wiklind et al., 2008; Yabe et al., 2009; Stark et al., 2009; Labbé et al., 2010a,b; González et al., 2010, 2012). In particular, observational evidence has emerged for the presence of strong optical nebular emission lines, such as $H\alpha$ and [OIII], in the typical $z \gtrsim 4$ source (Schaerer & de Barros, 2009; Shim et al., 2011; Stark et al., 2013; Labbé et al., 2013; González et al., 2014; de Barros et al., 2014; Smit et al., 2014).

While the rest-frame equivalent widths (EWs) of $H\alpha$ in typical star-forming galaxies at $z \sim 0 - 2$ range from 10-200Å in the typical source (Fumagalli et al., 2012), a large fraction of sources between $z \sim 4 - 7$ have inferred $H\alpha$ and [OIII] EWs in the range 300 - 1000Å (Schaerer & de Barros, 2009; Shim et al., 2011; Stark et al., 2013; Labbé et al., 2013; González et al., 2014; de Barros et al., 2014; Smit et al., 2014). The origin of these ubiquitous high-EW lines is still unclear and proves an ongoing challenge in our current understanding of the physical properties of high-redshift galaxies.

While the interpretation of the [OIII] line strength is complicated by the dependence on, for example, the gas density in the HII regions (e.g. Kewley et al., 2013; Shirazi et al., 2014), the $H\alpha$ line strength is known to be stable against variations in density or temperature and therefore should be a direct tracer of the star formation (Kennicutt, 1998). Shim et al. (2011) use the derived $H\alpha$ fluxes from a spectroscopic sample of sources in the range $z = 3.8 - 5.0$, where $H\alpha$ falls into the 3.6 μm *Spitzer*/IRAC filter, to understand the origin of these strong line emitters. Shim et al. (2011) argue that the most dominant factor that results in $H\alpha$ emission is the star formation history. However, the low signal-to-noise IRAC data of their sample combined with potential incompleteness of the sample due to preferential selection of $\text{Ly}\alpha$ emitters makes this analysis particularly challenging.

In this chapter we select both a large spectroscopic sample as well as a sample selected on photometric redshifts in the range $z = 3.8 - 5.0$ with exceptionally deep *Spitzer*/IRAC coverage from the S-CANDELS survey (Ashby et al., in prep) and deep K -band data (Kajisawa et al., 2006; Hathi et al., 2012; Fontana et al., 2014). This approach allows us to make a state of the art assessment on the origin of high-EW $H\alpha$ emission in typical high redshift sources. We search for correlations of $H\alpha$ EW with a large number of observational and physical properties and we

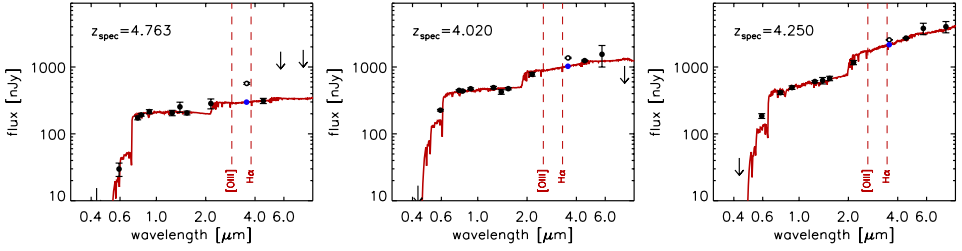


Figure 5.1: Three examples of stellar population fits to the broadband observations of galaxies from our sample. Flux densities and upper limits (2σ) of the *HST*, groundbased and *Spitzer*/IRAC photometry are indicated with black points and arrows, while the best-fit stellar population (§5.3.1) is drawn in red. The IRAC $3.6\ \mu\text{m}$ band flux is contaminated by $\text{H}\alpha$ and [NII] and is not included in the fit (open points). The $4.5\ \mu\text{m}$ band is largely free of line contamination and therefore provides the most important constraint on the stellar continuum at rest-frame visible wavelengths. The offset between the predicted $3.6\ \mu\text{m}$ continuum flux from the SED (indicated by the blue points) and the observed $3.6\ \mu\text{m}$ flux, provides a good estimate of the total $\text{H}\alpha$ + [NII] line flux.

study the bias of our spectroscopic and photometric-redshift-selected samples. Finally, we will discuss what we can learn from inferred $\text{H}\alpha$ star formation rates (SFRs) at $z \sim 4$ about the main sequence of star-forming galaxies and the SFR function at $z \sim 4 - 7$.

This chapter is organized as follows. In §5.2 we describe the observations we use and how we define our spectroscopic and photometric-redshift-selected samples, while we derive the observational and physical properties of our samples in §5.3. In §5.4 we derive $\text{H}\alpha$ -based SFRs, which we compare with UV-based SFRs and we discuss the potential origin of the discrepancy we find between the different probes. In §5.5 we establish the main sequence of star-forming galaxies from our $\text{H}\alpha$ measurements, while in §5.6 we translate our findings into SFR functions. Finally, we summarize our results in §5.7.

Throughout this chapter we adopt a Salpeter IMF with limits $0.1\text{--}100\ M_{\odot}$ (Salpeter, 1955). For ease of comparison with previous studies we take $H_0 = 70\ \text{km s}^{-1}\ \text{Mpc}^{-1}$, $\Omega_m = 0.3$ and $\Omega_{\Lambda} = 0.7$. Magnitudes are quoted in the AB system (Oke & Gunn, 1983)

5.2 Data and Samples

5.2.1 Spectroscopic sample

For our main sample of $z \sim 4$ galaxies we take advantage of the spectroscopic data collected over the GOODS-N field with the Keck/DEIMOS spectrograph (Stark et al., 2010, 2011) and over the GOODS-S field with the VLT/VIMOS and VLT/FORS2 spectrographs (Balestra et al., 2010; Vanzella et al., 2005, 2006, 2008, 2009). These authors have collected galaxy samples from spectroscopic follow-up of B- and V-drop selected galaxy candidates. Redshifts for these galaxies are mainly derived from the position of the $\text{Ly}\alpha$ emission line, although redshifts for a few bright galaxy candidates are derived from their UV absorption lines or continuum breaks.

We select sources with secure spectroscopic redshifts between $z = 3.8$ and $z = 5.0$; the redshift range where the $\text{H}\alpha$ line contributes to the flux in the $3.6\ \mu\text{m}$ band, while the $4.5\ \mu\text{m}$ band is free of contamination from strong nebular lines (see Shim et al., 2011; Stark et al., 2013). Within this redshift range the *K*-band is largely free of strong emission lines such as [OIII], $\text{H}\alpha$

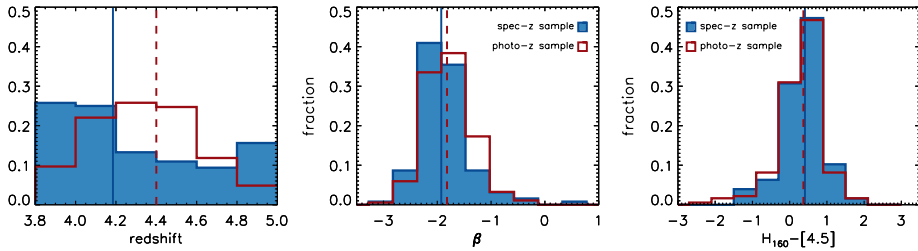


Figure 5.2: Comparison of the observational properties of our spectroscopic (filled blue histograms) and photometric-redshift-selected (red histograms) sample. The solid blue lines and dashed red lines indicate the median values for the spectroscopic and photometric-redshift-selected samples respectively. The median i_{775} -band magnitudes of the two samples are identical by construction, due to our $i_{775} \lesssim 26$ luminosity cut on the photometric-redshift-selected sample (see §5.2.2). *Left panel:* The redshift distribution of the two samples. We find a median $\langle z_{\text{spec}} \rangle \sim 4.17$ and a median $\langle z_{\text{phot}} \rangle \sim 4.40$. *Middle panel:* The UV-continuum slope, β , defined as $f_{\lambda} \propto \lambda^{\beta}$. The median UV-continuum slope of the spectroscopic sample is slightly bluer than the median slope for the photometric-redshift-selected sample. *Right panel:* The $H_{160} - [4.5]$ color, where the H_{160} -band probes the rest-frame UV-continuum and the $4.5 \mu\text{m}$ band gives a measure of the rest-frame optical continuum flux. The medians of the two samples are within errors. Overall, the colors of the SEDs of the spectroscopic sample show very little bias when compared to the photometric-redshift-selected sample, even though the majority of our spectroscopic redshifts are obtained from Ly α in emission.

and H β , though the [OII] $\lambda 3727\text{\AA}$ emission line could result in a slight boost to the K -band flux ($\sim 0.1 - 0.2$ mag) for galaxies between $z = 4.35$ and $z = 5.0$.

We obtain photometry for the sources in our sample by matching the spectroscopic $z = 3.8 - 5.0$ sample with the public 3D-*HST*/CANDELS catalogs presented by Skelton et al. (2014). We utilize their measured photometry in all *HST* bands (B_{435} , V_{606} , i_{775} , I_{814} , z_{850} , J_{125} , JH_{140} and H_{160}). The median 5σ limiting magnitude in the bands, measured in a $0''.7$ diameter aperture, ranges from 25.6 to 27.4. In short, Skelton et al. (2014) obtain their photometry by running Source Extractor (Bertin & Arnouts, 1996) in dual image mode on all bands, while matching their point spread function (PSF) to the H_{160} -band PSF. A combination of the J_{125} , JH_{140} and H_{160} images is used as the detection image (weighted by the square root of the inverse variance) and total fluxes are measured in Kron apertures.

Furthermore, we include the photometry in the *Spitzer*/IRAC bands at 6.8 and $8.0 \mu\text{m}$ from the Skelton et al. (2014) photometric catalogs, who make use of the GOODS *Spitzer* 3rd data release. We obtain the deepest possible photometry for the $3.6 \mu\text{m}$ and $4.5 \mu\text{m}$ bands by taking advantage of the imaging from the *Spitzer* Extended Deep Survey (SEDS: Ashby et al., 2013) and the *Spitzer* Very Deep Survey (*S-CANDELS*) Exploration Science Project (Ashby et al., in preparation), which covers the GOODS-N and GOODS-S fields with up to 50 hours exposure times (26.8 mag at 5σ in the $3.6 \mu\text{m}$ band). Similar to the procedure used for the public 3D-*HST*/CANDELS catalogs described in Skelton et al. (2014) we obtain photometry with the Multi-resolution Object PHotometry oN Galaxy Observations (MOPHONGO) code described in Labbé et al. (2006, 2010a,b), which provides an automated cleaning procedure for deblending the sources of interest and their neighboring sources. In short MOPHONGO creates model fluxes for all sources in a $\sim 11\text{''}$ radius by PSF-matching all detected galaxies in the H_{160} band to the IRAC image PSF and simultaneous fitting the normalizations of the modeled galaxies to match the observed IRAC image. Cleaned images are created by subtracting the model fluxes of all neighboring sources from the observed image. We measure the flux in the 3.6 and $4.5 \mu\text{m}$

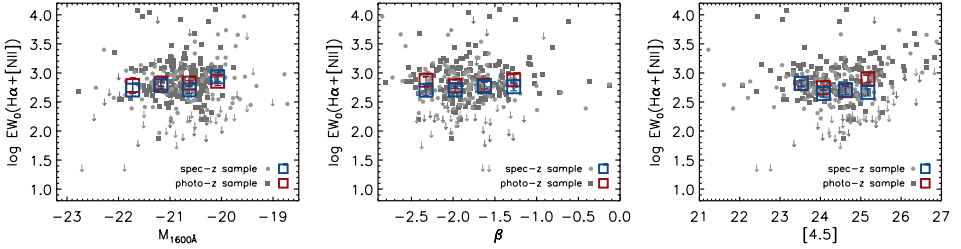


Figure 5.3: The rest-frame $H\alpha+[NII]$ EWs of our spectroscopic (light grey points) and our photometric-redshift-selected sample (dark grey squares), measured from the offsets in the observed $3.6\ \mu\text{m}$ flux with respect to the predicted stellar continuum (see §5.3.2). Errorbars are not shown to improve clarity of the figures. The left, middle and right panel show the dependence of $EW_0(H\alpha+[NII])$ as a function of the observed UV luminosity (measured at 1600\AA from the best fit stellar template), UV-continuum slope β and observed $[4.5]$ magnitude respectively. The blue and red squares indicate the median EWs (error bars represent the uncertainty in the median). We find no clear evidence for a dependence of the median emission line EW on the UV luminosity, UV-continuum slope β or the observed $[4.5]$ magnitude.

band from the cleaned images in $2''0$ diameter apertures and we apply a $\sim 2.2 - 2.4\times$ aperture correction based on the ratio of the flux enclosed in the photometric aperture in the *HST* image (before convolution) to the IRAC model (after convolution) of the source of interest.

In order to obtain good constraints on the rest-frame optical stellar light, both shortwards and longwards of the $H\alpha$ emission line, we require good signal-to-noise K -band photometry. For the GOODS-N field we therefore combine CFHT/WIRCam K_s -band imaging (Hathi et al., 2012) and Subaru/MOIRCS K_s -band imaging (Kajisawa et al., 2006). For the GOODS-S field we combine deep FOURSTAR K_s -band imaging from the Z-FOURGE survey (Spitler et al., 2012), VLT/ISAAC K_s -band imaging from the FIREWORKS survey (Retzlaff et al., 2010) and VLT/HAWK-I K_s band imaging from the HUGS survey (Fontana et al., 2014). We use MOPHONGO to perform an identical deblending procedure as described in the previous paragraph and we perform photometry on the cleaned images in $1''0$ diameter apertures. The median 5σ limiting depths are 24.8 and 25.2 mags in GOODS-N and GOODS-S respectively.

Our resulting catalog of $z_{\text{spec}} = 3.8 - 5.0$ galaxies consists of 98 sources in GOODS-N and 26 sources in GOODS-S, with high-quality constraints on the spectral energy distributions (SEDs) of the galaxies. The SEDs of three typical galaxies are presented in Figure 5.1.

5.2.2 Photometric sample

We complement our spectroscopic sample with a high-confidence photometric sample in order to evaluate potential biases introduced in the spectroscopic sample because we select mostly $Ly\alpha$ emitters. For this photometric sample we utilize the public photometric redshift catalog over the GOODS-S field from the 3D-*HST*/CANDELS data release (Skelton et al., 2014), generated using the EAZY software (Brammer et al., 2008). We require selected sources to have a photometric redshift within the redshift range $z = 3.8 - 5.0$ with at least 99% probability. We assemble the photometry for our photometric sample in an identical way to the spectroscopic sample as described in §5.2.1. We apply a luminosity cut for our sample below $i_{775} < 26.0$ in order to match the median i -band luminosity of our photometric sample as closely as possible to the median of the spectroscopic sample. Our resulting photometric catalog contains 206 sources.

We compare the observational properties of the two samples in Figure 5.2. The UV-continuum

colors are parametrized using the UV-continuum slope β , with $f_\lambda \propto \lambda^\beta$. The β -slope is approximated by a log-linear fit to the z_{850} , J_{125} , JH_{140} and H_{160} fluxes. The median UV-continuum color for the spectroscopic sample is $\Delta\beta \sim 0.1$ bluer than the median color for the photometric sample, while the difference in the median $H_{160} - [4.5]$ colors is similar to the uncertainty in the median (estimated by σ_β/\sqrt{N}). We conclude that the spectroscopic sample targeting mainly Ly α emitters is only mildly biased towards bluer galaxies with respect to the photometric sample (see also Schenker et al., 2013).

5.3 Derived properties of $z = 3.8 - 5.0$ galaxies

5.3.1 SED fitting

We determine stellar masses and other stellar population parameters by fitting stellar population synthesis templates to the observed photometry using FAST (Kriek et al., 2009). Since we consider only stellar continuum in our models we exclude the $3.6 \mu\text{m}$ band, where $H\alpha$ and [NII] boosts the observed flux, from our fitting procedure. We consider constant star formation histories with ages between 10 Myr and the age of the Universe at $z = 3.8$. Furthermore, we assume a Calzetti et al. (2000) dust law, with A_V in the range $0 - 2$. Finally, we fit metallicities between $0.2 - 1.0Z_\odot$. While the redshifts for our spectroscopic sample are fixed, we allow the redshifts for our photometric sample to vary between $z = 3.8 - 5.0$, given that we determined in §5.2.2 that the sources from this sample have photometric redshifts between $z \sim 3.8 - 5.0$ at 99% confidence. Our estimated median stellar mass is $\sim 6 \cdot 10^9 M_\odot$ for our spectroscopic sample and $\sim 5 \cdot 10^9 M_\odot$ for our photometric sample. Furthermore we find a median age of 174 Myr for our spectroscopic sample and 79 Myr for our photometric sample.

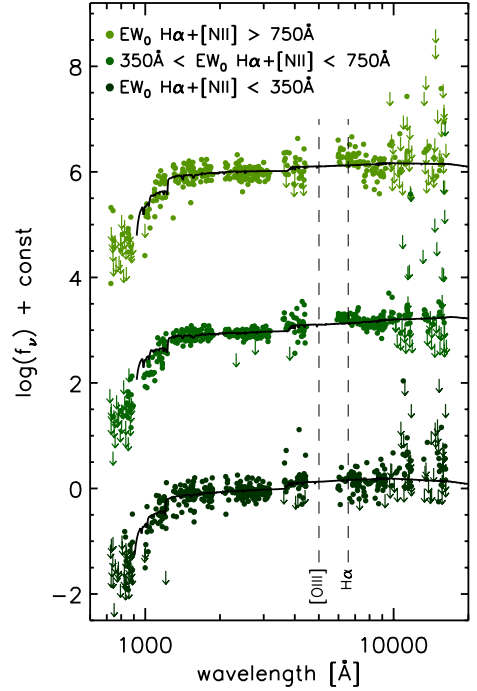
5.3.2 $H\alpha$ + [NII] equivalent widths and line strengths

We infer the total emission line flux in our sources from the $3.6 \mu\text{m}$ band by subtracting the predicted continuum fluxes of the best fit stellar templates (see Figure 5.1) from the observed $3.6 \mu\text{m}$ fluxes and we correct for the width of the $3.6 \mu\text{m}$ filter using the spectral response curve of the filter¹ (see also Shim et al., 2011; Stark et al., 2013). We estimate the uncertainty on the predicted continuum flux to be equal to the uncertainty on the $4.5 \mu\text{m}$ band flux and we therefore calculate the uncertainties estimated line strength from the noise in the $3.6 \mu\text{m}$ and $4.5 \mu\text{m}$ bands. If the uncertainty on the line flux is larger than the offset between the observed $3.6 \mu\text{m}$ flux and the predicted continuum, we place an upper limit on the line flux.

Since the total emission line flux is dominated by the contribution from $H\alpha$ and [NII] (e.g. Anders & Fritze-v. Alvensleben, 2003) we directly obtain rest-frame equivalent widths (EW_0) for these combined lines from the inferred total emission line flux and the predicted continuum of the best fit stellar template, after correcting the observed EW by a factor $(1 + z)$. Here, we use the FAST redshift estimates for the photometric sample. We find $EW_0(H\alpha+[NII]) \sim 500\text{\AA}$ in the median source. No dust correction is performed for the observed EWs. This is in excellent agreement with the results by Stark et al. (2013) who measure $\langle \log_{10}(EW_{3.6\mu\text{m}}) \rangle \sim 2.73$ in the rest-frame when they exclude the $3.6 \mu\text{m}$ band from the continuum fitting.

¹<http://irsa.ipac.caltech.edu/data/SPITZER/docs/irac/calibrationfiles/spectralresponse/>

Figure 5.4: Composite spectral energy distributions of the sources in the spectroscopic sample, shown as a function of the rest-frame wavelengths (green points). The sources are used in the top, middle, and bottom SED when their estimated $EW_0(H\alpha+[NII])$ are greater than 750\AA , between 350\AA and 750\AA , and less than 350\AA respectively. The SEDs are offset in the y-axis for clarity. All points are normalized by the log mean of the z_{850} , H_{160} and $4.5\ \mu\text{m}$ fluxes. The black curves indicate a stellar continuum fit to the composite SEDs. The dashed black lines indicate the position of $[OIII]$ and $H\alpha$ nebular lines. Although the offsets in the photometry around the $H\alpha$ line are clearly visible in the top and middle SEDs, there is surprisingly little variation in the shape of the stellar continuum of the three SEDs.



We show the distribution of the resulting EWs as a function of the UV-luminosity (measured at 1600\AA from the best fit stellar template), UV-continuum slope β and observe $[4.5]$ magnitude in Figure 5.3. Surprisingly, the typical derived $EW_0(H\alpha+[NII])$ does not depend strongly on the observed UV properties of sample, indicating high $H\alpha$ EWs regardless of the UV luminosity, slope β or $[4.5]$ magnitude (i.e. rest-frame optical $\sim 8500\text{\AA}$).

To gain further insight into the origin of these high EWs, we use the public catalogs with structural parameters presented by van der Wel et al. (2012, 2014) to identify potential correlations with our $H\alpha$ measurements. However, we find no dependence of $EW_0(H\alpha+[NII])$ on half-light radius or Sérsic index. Furthermore, we study the dependence of $H\alpha$ EW on the parameters from our stellar population modeling (§5.3.1). We find a clear dependence of $EW_0(H\alpha+[NII])$ on age and sSFR (given our assumption of constant SFH, age and sSFR are inversely proportional). We find a weak trend of higher $H\alpha$ EWs with lower stellar masses, which is consistent with the fact that we find higher sSFRs with lower masses. In §5.4.2 we will discuss various physical interpretations that could be underlying the high-EW $H\alpha$ emission.

Finally, we derive an estimate of the $H\alpha$ line flux by adopting a fixed ratio between $H\alpha$ and $[NII]$ as tabulated in Anders & Fritze-v. Alvensleben (2003) for sub-solar ($0.2Z_{\odot}$) metallicity, i.e. $L_{H\alpha} = 0.84 \times L_{3.6\ \mu\text{m}}$.

5.3.3 Composite SEDs

Our spectroscopic sample is particularly well suited to construct composite SEDs of star-forming galaxies over the redshift range $z = 3.8 - 5.0$. Figure 5.4 shows three composite SEDs, with

galaxies divided in to different samples based their estimated $EW_0(H\alpha+[NII])$. The flux measurements are normalized on the z_{850} , H_{160} and $4.5 \mu\text{m}$ bands. By construction the offset in the flux measurements around the $H\alpha$ line increases from bottom to top. However, we find little variation in the shape of the SEDs otherwise.

5.4 Inferred $H\alpha$ as star formation rate indicator

Our determination of the $H\alpha$ line flux in §5.3.2 provides us with the unique opportunity to explore the use of inferred $H\alpha$ fluxes as an independent star formation rate indicator in high-redshift galaxies. Shim et al. (2011) pioneered the use of inferred $H\alpha$ to measure SFRs of $z \sim 4$ galaxies. However, the exceptionally deep S/N Spitzer/IRAC data from the S-CANDELS data-set (Ashby et al., in prep) covering our large spectroscopic sample and photometric sample allows us to systematically asses SFRs over the general $z \sim 4$ galaxy population.

5.4.1 Star formation rate indicators

In this section we will define two independent SFR indicators, based on the $H\alpha$ and UV properties of our samples, using calibrations of local star-forming galaxies. The comparison of these two probes will allow us to investigate the different time scales of star-formation, since $H\alpha$ is sensitive to the star-formation history (SFH) over a ~ 10 Myr timescale, while UV light provides a time-averaged SFR over a ~ 100 Myr time window (e.g. Kennicutt, 1998).

To obtain UV-based SFRs we convert the UV-luminosity measured at 1600\AA from the best fit stellar template into a SFR using the Kennicutt (1998) relation

$$\text{SFR} (M_{\odot} \text{ yr}^{-1}) = 1.4 \times 10^{-28} L_{\text{UV}} (\text{erg s}^{-1} \text{ Hz}^{-1}). \quad (5.1)$$

We estimate the dust attenuation in the UV from the calibration by Meurer et al. (1999) using local starbursting systems

$$A_{1600} = 4.43 + 1.99\beta, \quad (5.2)$$

where we estimate the UV-continuum slope β using a log-linear fit to the z_{850} , J_{125} , JH_{140} and H_{160} fluxes. Our estimated median dust corrected UV-based SFR ($\text{SFR}_{\text{UV}+\beta}$) is equal to $\sim 20 M_{\odot} \text{ yr}^{-1}$ for our spectroscopic sample and $\sim 24 M_{\odot} \text{ yr}^{-1}$ for our photometric sample. We explicitly do not estimate our UV-based SFRs from the SED fitting procedure due to the degeneracy between age and dust that is particularly challenging to solve. However, we will discuss the influence of different calibrations of the dust law on the UV-based SFRs in §5.4.2.4.

To obtain SFRs from the $H\alpha$ line luminosity measurements derived in §5.3.2 we use the Kennicutt (1998) relation

$$\text{SFR} (M_{\odot} \text{ yr}^{-1}) = 7.9 \times 10^{-42} L_{H\alpha} (\text{erg s}^{-1}). \quad (5.3)$$

We estimate the dust attenuation from the Calzetti et al. (2000) dust law and the UV dust attenuation derived using Eq. 5.2. Here, we assume $A_{V,\text{stars}} = 0.44 \cdot A_{V,\text{gas}}$ (e.g. Calzetti et al., 2000). Our estimated median SFR from $H\alpha$ ($\text{SFR}_{H\alpha}$) after dust correction is equal to $\sim 64 M_{\odot} \text{ yr}^{-1}$ for our spectroscopic sample and $\sim 52 M_{\odot} \text{ yr}^{-1}$ for our photometric sample.

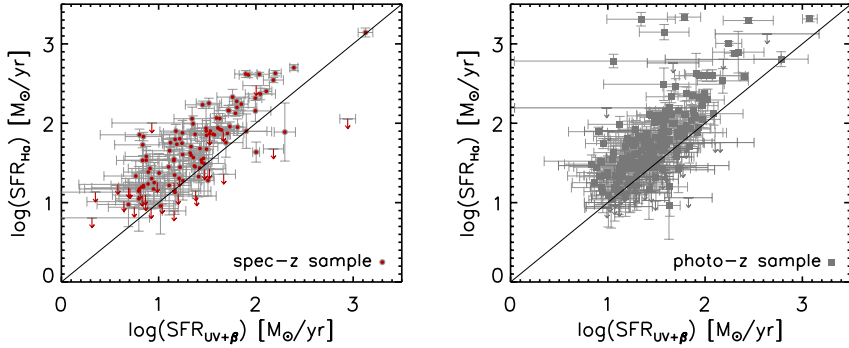


Figure 5.5: Star formation rates from the inferred $H\alpha$ luminosities versus those from the UV-luminosity corrected for dust using the UV slope β and the Meurer et al. (1999) calibration (red points; red arrows indicate the 1σ upper limits). The left panel shows our spectroscopic sample, while the right panel shows our photometric sample. The median SFRs are offset from the one to one relation (black line) by ~ 0.35 dex for the spectroscopic sample and ~ 0.32 dex for the photometric sample.

We compare $SFR_{UV+\beta}$ and $SFR_{H\alpha}$ indicators in Figure 5.5 and we find that the two indicators are strongly correlated in both the spectroscopic and photometric samples. This strong correlation confirms that our method of inferring $H\alpha$ line measurements from the broadband IRAC photometry results in reliable SFR measurements. However, we also find a systematic offset of $0.35^{+0.04}_{-0.06}$ dex for the spectroscopic sample and $0.32^{+0.04}_{-0.06}$ dex for the photometric sample from the one to one relation, indicating that the strength of $H\alpha$ is difficult to predict from the rest-frame UV properties using local calibrations.

This discrepancy was already noted Shim et al. (2011), who find a mean $\langle SFR_{H\alpha}/SFR_{UV} \rangle \sim 6$ (uncorrected for dust extinction), slightly larger (~ 0.13 dex) than the $SFR_{H\alpha}/SFR_{UV}$ we find from our sample before dust correction.

In the §5.4.2.1-5.4.2.4 we will discuss how our assumptions on the SFH, dust extinction or the shape of the ionizing spectrum influence our measurements and whether they can explain the offset apparent in Figure 5.5.

5.4.2 Origin of high $H\alpha$ star formation rates

5.4.2.1 Bursty star formation histories

One possibility explanation for the high $SFR_{H\alpha}/SFR_{UV+\beta}$ ratios we derive in §5.4.1 would be in the star formation histories of the galaxies in our sample, i.e., if the galaxies we examine are all predominantly young. This is the hypothesis that Shim et al. (2011) favour for explaining the high $SFR_{H\alpha}/SFR_{UV}$ in the sample they observe.

In Figure 5.5 we show $SFR_{H\alpha}$ as a function of $SFR_{UV+\beta}$ for both our spectroscopic sample (left) and our photometric sample (right). While the majority of the sources on the left panel are Ly α emitters and therefore this distribution could be biased towards starbursting systems, we find little difference in the median $SFR_{H\alpha}/SFR_{UV+\beta}$ ratio of our spectroscopic and our photometric sample. Moreover, a subsample of sources with stellar masses above our mass completeness limit of $\sim 10^{10} M_{\odot}$ gives a comparable median $SFR_{H\alpha}/SFR_{UV+\beta}$ ratio to that of the entire photometric

sample. These findings argue against the solution of very young (<10 Myr) starburst ages as the origin for the systematic offset in $H\alpha$ and UV SFRs.

To gain further insight we show the *specific* $SFR_{H\alpha}$ as a function of the specific $SFR_{UV+\beta}$ in Figure 5.6. The two sSFR estimates correlate strongly over ~ 2 dex in sSFR and we find a similar constant offset between the $H\alpha$ and UV probes. For a galaxy population with a bursty star formation history we would expect the discrepancy between $sSFR_{H\alpha}$ and $sSFR_{UV+\beta}$ to decrease with decreasing $sSFR_{H\alpha}$. For reference we include a single stellar population (SSP) track (rose line) that demonstrates the rapid evolution of the $sSFR_{H\alpha}/sSFR_{UV+\beta}$ ratio of this stellar population with age. A burst of star formation is expected to show enhanced $H\alpha$ for ~ 5 Myr, but we would expect many sources with ages >10 Myr after the burst below the one to one relation. Comparing this model with our observations, we observe no trend that argues in favor of such bursty histories.

5.4.2.2 Rising star formation histories

In §5.4.2.1 we describe how the systematic offset in $H\alpha$ and UV-based sSFRs disfavors bursty star formation histories. However, based on Figure 5.6 it is difficult to distinguish between constant or smoothly rising star formation histories. A rising history can affect the $SFR_{H\alpha}/SFR_{UV+\beta}$ ratio simply because the UV provides time-averaged SFR over a ~ 100 Myr time window and the instant SFR is lower at earlier times. Reddy et al. (2012) tabulate the values of SFR/L_{1700} as a function of galaxy age for different star formation histories (see their Table 6). An exponentially rising star formation history ($\tau \sim 100$) results in a ~ 0.1 dex higher SFR/L_{1700} ratio for a galaxy of 100 Myr compared to the conversion factor in Eq. 5.1. Assuming $H\alpha$ is a good tracer of the instantaneous SFR we estimate that rising star formation histories can result in a ~ 0.1 dex offset $SFR_{H\alpha}/SFR_{UV+\beta}$ ratio.

5.4.2.3 Sources of ionizing radiation

In §5.4.2.1 and §5.4.2.2 we discussed the influence of star formation history on the offset between $H\alpha$ and UV-based SFR indicators in our $z \sim 4$ galaxy sample. While in particular rising star formation histories can systematically offset the two SFR indicators by ~ 0.1 dex, we argue that the ~ 0.35 dex offset in Figure 5.5 cannot be fully explained by our assumptions on the SFH.

Another effect on the $SFR_{H\alpha}/SFR_{UV+\beta}$ ratio that we must consider is the potential for a changing conversion factor between $L_{H\alpha}$ and SFR (i.e. Eq. 5.3). While the $H\alpha$ flux scales directly with the number of ionizing photons emerging from the HII regions in the galaxy (Kennicutt, 1998), the shape of the ionizing spectrum in low metallicity galaxies is ill-constrained. In particular the influence of massive binaries, rotational mixing (e.g. de Mink et al., 2009) and line blanketing can change with metallicity. For a more elaborate discussion we refer to §3 in Kewley et al. (2013). Furthermore, differences in the high-mass slope of the IMF would also introduce a different ionizing spectrum. However, even without changes in the IMF a metallicity dependent ionizing spectrum could significantly impact the $SFR_{H\alpha}/SFR_{UV+\beta}$ ratio.

We illustrate this in the right panel Figure 5.6, where we show stellar population tracks from Eldridge & Stanway (2012) for a galaxy with a constant SFH and including binary star evolution. The track runs parallel to the one to one relation and it is systematically offset to higher $sSFR_{H\alpha}$ measurements than one would obtain using the local calibration in Eq. 5.3.

Given the current uncertainties in the shape of the ionizing spectrum we estimate the influence

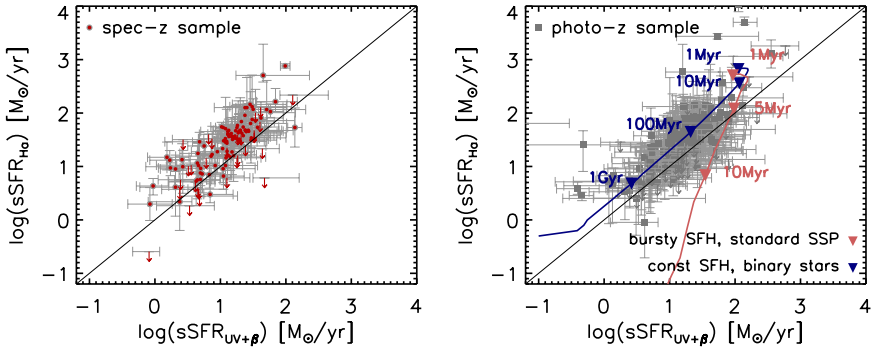


Figure 5.6: The specific star formation rates from the inferred $H\alpha$ luminosities versus those from the UV-luminosity corrected for dust using the UV slope β and the Meurer et al. (1999) calibration (red points; red arrows indicate the 1σ upper limits). The left panel shows our spectroscopic sample, while the right panel shows our photometric sample. The right panel includes two tracks from the BPASS (Eldridge & Stanway, 2009, 2012; Stanway et al., 2014) stellar population synthesis models. The rose color track includes only single star populations and follows a single burst of star formation with an initial mass of $10^6 M_{\odot}$. We indicate the measured sSFRs of this model using the Kennicutt (1998) relations at ages of 1 Myr, 5 Myr and 10 Myr (rose triangles). The dark blue color track includes the effect of massive binaries on a stellar population with a constant star formation history of $1 M_{\odot} \text{yr}^{-1}$. We indicate the measured sSFRs of this model using the Kennicutt (1998) relations at ages of 1 Myr, 10 Myr, 100 Myr and 1 Gyr (dark blue triangles). We find no evidence for bursty star formation histories, given the fact that our specific star formation rates are systematically offset from the one to one relation (black line).

of changing ionizing spectrum from the calibration by Steidel et al. (2014) at $z \sim 2$. These authors use the line ratios of strong optical nebular emission lines to identify changing conditions in the HII regions with respect to the local universe. They model the shape of the spectrum with a blackbody curve (normalized at 912\AA) and find a shift in the effective temperature of the curve from $T_e \sim 42000$ at $z \sim 0$ to $T_e \sim 55000$ at $z \sim 2$. We use this calibration to estimate the number of ionizing photons ($\lambda < 912\text{\AA}$) at $z \sim 0$ and $z \sim 2$ and find a factor of 1.5 increase in the number of such photons. We therefore argue that our $\text{SFR}_{H\alpha}$ determinations could potentially be overestimated by 0.17 dex when taking an evolving ionizing spectrum into account when converting $H\alpha$ to SFR (i.e. Eq. 5.3).

5.4.2.4 Dust law

While the influence of a high effective ionization fields (§5.4.2.3) are important to consider, given the active debate around evolving emission line ratios at high redshift (e.g. Kewley et al., 2013; Steidel et al., 2014; Stanway et al., 2014), a potentially more significant influence on the discrepancy between $H\alpha$ and UV-based SFRs arises from the assumptions we make on the calibrated dust law. We will therefore investigate a different dust correction to the UV luminosities in this section.

Recently, the possibility of a different dust calibration for high redshift sources was discussed by Wilkins et al. (2012, 2013), de Barros et al. (2014) and Castellano et al. (2014). These authors argue that high redshift sources likely have lower metallicities and younger ages than the local starburst galaxies used in the empirical Meurer et al. (1999) calibration. The Meurer et al. (1999) calibration implicitly assumes a dust-free UV slope of the galaxy of $\beta_{\text{dust-free}} = -2.23$,

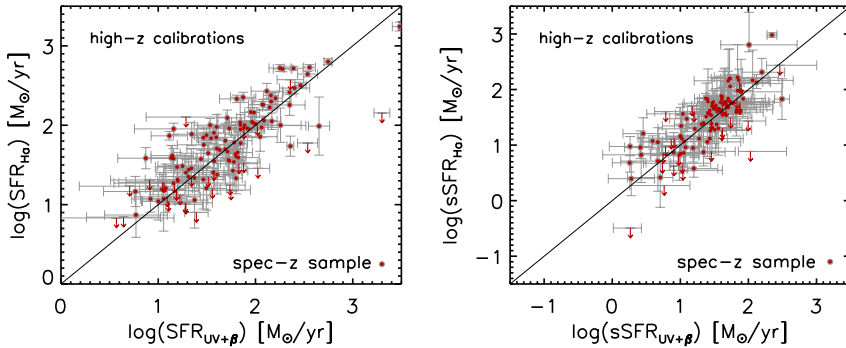


Figure 5.7: The $\text{SFR}_{\text{H}\alpha}$ as a function of $\text{SFR}_{\text{UV}+\beta}$ (left) and $\text{sSFR}_{\text{H}\alpha}$ as a function of $\text{sSFR}_{\text{UV}+\beta}$ (right) for our spectroscopic sample, using high-redshift calibrations such as described in §5.4.2.4. UV-based SFRs are corrected for dust using $A_{1600} = 5.32 + 1.99\beta$ (e.g., Castellano et al., 2014). $\text{H}\alpha$ SFRs are adjusted downwards by 0.17 dex to account for sources of high ionizing radiation (§5.4.2.3), such as calibrated by Steidel et al. (2014). While the direct calibration of different SFRs at $z \sim 4$ will only be possible with the advancement of ALMA and *JWST*, we find that we can resolve the discrepancies in Figures 5.5 and 5.6 using these assumptions.

consistent with solar metallicity and ages of a few hundred Myr. However, our $z \sim 4$ UV selected galaxies likely have ages around ~ 100 Myr or less (see §5.3.1), while their metallicity content is expected to be no higher than $0.1 - 0.5 Z_{\odot}$, measured for $z \sim 3$ UV selected galaxies by e.g., Maiolino et al. (2008), Mannucci et al. (2009) and Troncoso et al. (2014). These physical properties result in bluer $\beta_{\text{dust-free}}$ and therefore the dust reddening of the UV slope could therefore be underestimated when assuming the Meurer et al. (1999) calibration.

Though far-infrared (FIR) constraints on individual sources, needed to calibrate dust corrections at $z \sim 4$, will likely soon emerge from the new generation of sub-mm detectors such as ALMA and IRAM, current FIR constraints can only be obtained through stacking. While stacking analysis of $z \sim 2$ galaxy populations generally find good agreement with the Meurer et al. (1999) relation (e.g. Reddy et al., 2012; Pannella et al., 2014; Oteo, 2014), various recent stacking results at $z \gtrsim 3$ indicate an underestimate of the FIR flux by the Meurer et al. (1999) calibration (e.g. Oteo et al., 2013; Oteo, 2014; Pannella et al., 2014; Coppin et al., 2014).

Alternatively, an estimate of $\beta_{\text{dust-free}}$ can be obtained from SED modeling (e.g. de Barros et al., 2014; Castellano et al., 2014). For example, Castellano et al. (2014) use a sample of $z \sim 3$ Lyman-break galaxies with known metallicities from NIR-spectroscopy to model the dust content of these galaxies. Based on their modeling they propose a dust calibration

$$A_{1600} = 5.32^{+0.41}_{-0.37} + 1.99\beta, \quad (5.4)$$

implying a $\beta_{\text{dust-free}} \sim -2.67$. We explore the effect of this dust calibration, in combination with at 0.17 dex correction on the $\text{H}\alpha$ SFRs (see §5.4.2.3), in Figure 5.7. We find that the Castellano et al. (2014) calibration lowers the median $\text{SFR}_{\text{H}\alpha}/\text{SFR}_{\text{UV}+\beta}$ ratio by 0.23 dex; the UV-based SFRs increase by 0.4 dex, while $\text{H}\alpha$ -based SFRs increase only by 0.17 dex since $\text{H}\alpha$ is less sensitive to dust extinction compared to the rest-frame UV light (following the Calzetti et al. 2000 dust law). In combination with either a rising star formation history or a changing contribution of highly ionizing sources at low metallicities, we can bring $\text{H}\alpha$ and UV-based SFRs into reasonable agreement.

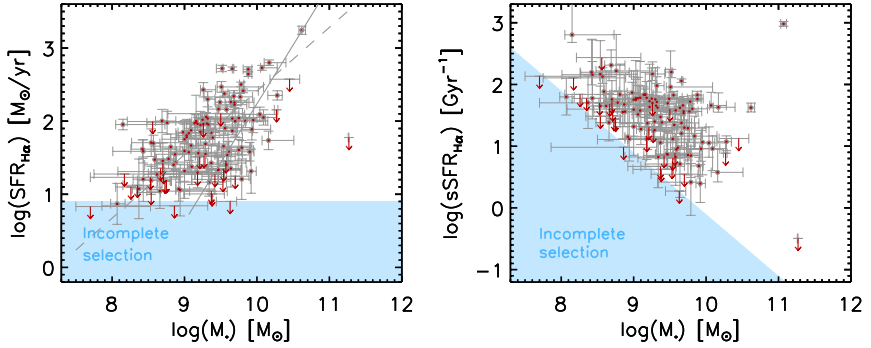


Figure 5.8: The $\text{SFR}_{\text{H}\alpha}$ (left) and $\text{sSFR}_{\text{H}\alpha}$ (right) as a function of stellar mass for our spectroscopic sample. The dashed and solid lines indicate the Bayesian linear regression for all galaxies and those with $M_* > 10^{9.75} M_{\odot}$ respectively. The blue shaded region gives an indication of the incompleteness in our sample due to the UV selection. We find that the slope of the SFR-mass sequence is broadly consistent with unity (e.g. Whitaker et al., 2014) and an intrinsic scatter of $0.2 - 0.3$ dex.

5.5 SFR-mass sequence

One of the most fundamental relations for understanding galaxy build-up is the SFR-stellar mass relation, or the main sequence of star-forming galaxies. Using our derived $\text{H}\alpha$ -based SFRs we are in an excellent position to assess this relation at $z \sim 4$, given the much weaker sensitivity of our $\text{H}\alpha$ -based SFR measurements to many of the classic degeneracies that affect stellar population modelling (e.g. dust vs. age). For this analysis we will make use of the high redshift calibrations described in §5.4.2.3 and 5.4.2.4 (see also Figure 5.7).

In Figure 5.8 we show $\text{SFR}_{\text{H}\alpha}$ and $\text{sSFR}_{\text{H}\alpha}$ as a function of stellar mass for our spectroscopic sample. In order to understand a potential bias in our sample we indicate the $\text{SFR}_{\text{UV}+\beta}$ limit of $\sim 8 M_{\odot} \text{yr}^{-1}$ that roughly corresponds to a UV luminosity of -19.5 , below which our spectroscopic sample is clearly incomplete (see Figure 5.3). While the slope of the main sequence of star forming galaxies appears to be significantly shallower than unity from a fit to all the sources in our sample (dashed line in the left panel of Figure 5.8), we find that a fit using only sources above $10^{9.75} M_{\odot}$ (solid line in the left panel of Figure 5.8) is broadly consistent with the unity low-mass slope found by Whitaker et al. (2014) for star-forming galaxies between $z \sim 0.5 - 2.5$.

Furthermore we estimate the scatter in the main sequence of star-forming galaxies from the Bayesian linear regression (solid line) which gives an intrinsic scatter of $0.2 - 0.3$ dex, indicative of a relatively smooth star formation history. This intrinsic scatter is somewhat higher than the ~ 0.13 dex scatter measured by Speagle et al. (2014) based on the Shim et al. (2011) sample, but in good agreement with the recent determination from Salmon et al. (2014).

While the dynamic range where we have a mass complete sample is limited, we can compare the normalization of our SFR-mass sequence with determinations at lower redshift in more detail. At a fixed mass bin around $10^{10} M_{\odot}$ we find a median $\log_{10} \text{SFR}_{\text{H}\alpha} / M_{\odot} \text{yr}^{-1} = 1.72^{+0.11}_{-0.13}$ and $\log_{10} \text{sSFR}_{\text{H}\alpha} / \text{Gyr}^{-1} = 0.74^{+0.09}_{-0.09}$ (uncertainties obtained through bootstrapping). This is slightly lower than the fit by Speagle et al. (2014), who compare 25 studies between $z \sim 0$ and $z \sim 6$ and predict an SFR of $\log_{10} \text{SFR} / M_{\odot} \text{yr}^{-1} \sim 1.89$ at our median redshift $\langle z_{\text{spec}} \rangle = 4.2$ and stellar mass of $10^{10} M_{\odot}$. Furthermore, extrapolating the relation for $\text{sSFR} \propto (1+z)^{1.9}$ found

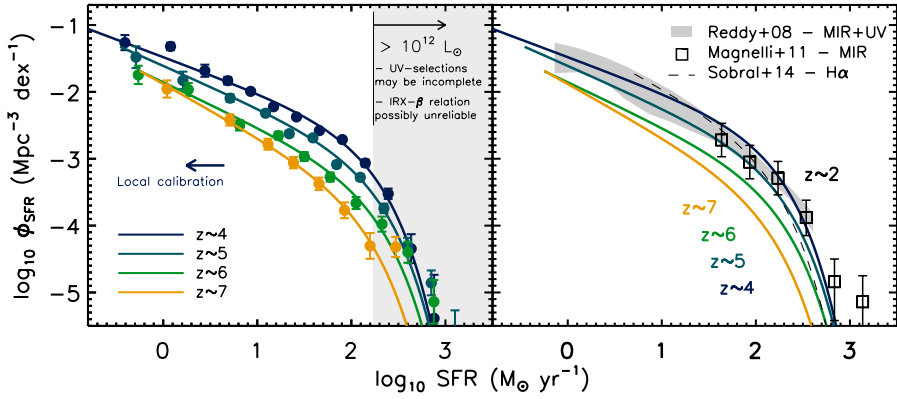


Figure 5.9: Determination of the SFR function between $z \sim 4$ and $z \sim 7$ following the procedure by Smit et al. (2012). The SFR functions are based on the UV luminosity functions by Bouwens et al. (2014b), the color magnitude relations determined by Bouwens et al. (2014a) and the Castellano et al. (2014) dust calibration given in Eq. 5.4. *Left panel:* Stepwise dust-corrected SFR functions with the analytical solutions for the Schechter functions (see Eq. 4, 7 and 8 by Smit et al., 2012). The gray shaded region indicates the SFR range where our UV selection can be incomplete due to dust saturation. The dark blue arrow indicates the 0.4 dex decrease in the knee of the SFR function in the case where we would have assumed the local Meurer et al. (1999) dust calibration. *Right panel:* The Schechter functions with SFR functions at $z \sim 2$ from $H\alpha$ (dashed black line Sobral et al., 2014), MIR (open black squares Magnelli et al., 2011) and UV+MIR (gray shaded region Reddy et al., 2008) SFR probes.

by Whitaker et al. (2014) between $z \sim 0.5 - 2.5$, we would predict $\log_{10} \text{SFR}/M_{\odot}\text{yr}^{-1} \sim 2.05$ at $10^{10} M_{\odot}$ if this relation holds out to $z \sim 4$. Comparing our normalization of the main sequence with recent estimates at the same redshift we find good agreement with Stark et al. (2013) who find $\log_{10} \text{sSFR}_{\text{UV}+\beta}/\text{Gyr}^{-1} \sim 0.79$ at $5 \cdot 10^9 M_{\odot}$. However, our determinations are significantly higher than a number of recent estimates using SFRs from SED fitting; e.g. González et al. (2014) find $\log_{10} \text{sSFR}_{\text{SED}}/\text{Gyr}^{-1} \sim 0.54$ at $5 \cdot 10^9 M_{\odot}$, Duncan et al. (2014) find $\log_{10} \text{sSFR}_{\text{SED}}/\text{Gyr}^{-1} \sim 0.37$ at $5 \cdot 10^9 M_{\odot}$ and Salmon et al. (2014) find a median $\log_{10} \text{SFR}_{\text{SED}}/M_{\odot}\text{yr}^{-1} \sim 1.35$ at $z \sim 4$ and $10^{10} M_{\odot}$.

We summarize our findings on the $\text{SFR}_{H\alpha} - M_*$ sequence in Table 5.3.

5.6 Star formation rate functions

In §5.4.2.4 we adopted a dust calibration (Eq. 5.4) that assumes bluer intrinsic UV slopes, in order to obtain a better match to the $H\alpha$ -based star formation rates in our samples. In order to understand the potential consequences of such a dust correction we construct SFR functions (Smit et al., 2012), using the Castellano et al. (2014) dust calibration. The SFR function is useful since it can be used to compare high redshift UV-luminosity functions with $H\alpha$ and infrared (IR) based SFR functions at $z \sim 2$.

Smit et al. (2012) give a prescription to correct UV-luminosity functions for dust based on a luminosity dependent determination of the UV slope, β (e.g. Bouwens et al., 2012, 2014a), a dust calibration of the form $A_{1600} = C_0 + C_1\beta$ and a fixed scatter around the β -luminosity relation, σ_{β} (see Eq. 4, 7 and 8 by Smit et al., 2012). We convert the dust-corrected UV-luminosity

functions to SFR functions using the Kennicutt (1998) relation, given by Eq. 5.1. Stepwise determinations and Schechter parameters are given in Table 5.1 and 5.2 respectively. We base our SFR functions on the determination of the UV-luminosity functions at $z \sim 4 - 7$ by Bouwens et al. (2014b) and determinations of the color magnitude relations by Bouwens et al. (2014a). The resulting SFR functions are shown in Figure 5.9 in combination with the $H\alpha$ -based SFR function derived by Sobral et al. (2014), the UV+MIR luminosity function derived by Reddy et al. (2008) and the MIR luminosity function measured by Magnelli et al. (2011) converted to SFR using the Kennicutt (1998) relation.

The effect of the Castellano et al. (2014) dust calibration on high redshift SFRs, as seen from Figure 5.9, implies a high-end of SFR function at $z \sim 4$ that is similar to the IR-based SFR function at $z \sim 2$. Furthermore, our determination of the $z \sim 4$ SFR function even exceeds the $H\alpha$ -based SFR function at $z \sim 2$ as determined by (Sobral et al., 2014). On the left panel of Figure 5.9 the SFR range above $\sim 150 M_{\odot} \text{yr}^{-1}$, equivalent to $L_{\text{bol}} > 10^{12} M_{\odot}$, where we might expect dust saturated sources that are missed in an UV-selected sample. Given that the $z \sim 4$ and $z \sim 5$ SFR functions reach beyond $L_{\text{bol}} > 10^{12} M_{\odot}$, we might imagine our SFR functions to be underestimated at the high-end.

Based on the results in Figure 5.9 it seems plausible that the total star formation rate density does not decline after $z \sim 2$, but plateaus out to $z \sim 4$ and starts to decline at $z \gtrsim 5$. The implication is that the peak of the global star formation history of the universe is shifted from $z \sim 2$ towards earlier epochs. Though our dust correction at present is rather uncertain due to the lack of individual FIR detections that enable a direct calibration, our results emphasize the importance of future work with new generation sub-mm facilities such as ALMA for a complete understanding of star formation over cosmic time.

5.7 Summary

In this chapter we make use of a large sample of galaxies with spectroscopic redshifts between $z = 3.8 - 5.0$, where $H\alpha$ can be inferred from the excess in the $3.6 \mu\text{m}$ *Spitzer*/IRAC band, as well as a photometric sample in the same redshift range. As in previous studies (e.g. Shim et al., 2011; Stark et al., 2013) we find a typical rest-frame $H\alpha$ EW of $\sim 500 \text{ \AA}$ for a spectroscopic $z = 3.8 - 5.0$ sample. However, we also conduct a systematic investigation of the $H\alpha$ EWs in pure photometric-redshift-selected $z \sim 3.8 - 5.0$ sample for the first time and find similar results for both samples. While we find no dependence of the $H\alpha$ EWs on UV luminosity, UV slope, half-light radius or Sérsic index; we do however find a clear relation between $\text{EW}_0(H\alpha + [\text{NII}])$ and specific star formation rate or age.

We explore the use of inferred $H\alpha$ fluxes to derive star formation rates for the galaxies in our samples. We compare these $H\alpha$ -based SFRs with UV-based SFRs using the Meurer et al. (1999) relation and find a strong relation between the two estimates, with a ~ 0.3 dex offset in the median $\text{SFR}_{H\alpha} / \text{SFR}_{\text{UV}+\beta}$ ratio.

We discuss the influence of the assumed SFH, shape of the ionizing spectrum and the dust law on the $\text{SFR}_{H\alpha} / \text{SFR}_{\text{UV}+\beta}$ ratio:

- *Bursty SFH*: Bursty star formation histories result in high $H\alpha$ EWs and high $\text{SFR}_{H\alpha} / \text{SFR}_{\text{UV}+\beta}$ ratios for short (~ 5 Myr) time periods. However, we find comparable $\text{SFR}_{H\alpha} / \text{SFR}_{\text{UV}+\beta}$

for our spectroscopic sample, photometric sample and even a mass limited photometric subsample. We therefore argue that bursty star formation histories are unlikely to be the cause for the *systematic* offset in the two SFR indicators (in contrast to earlier suggestions by Shim et al. 2011).

- *Rising SFH*: Rising star formation histories create an offset in the $\text{SFR}_{H\alpha}/\text{SFR}_{UV+\beta}$ ratio, due to the different timescales of star formation probed by $H\alpha$ (~ 10 Myr) and UV (~ 100 Myr) SFR indicators. We estimate this offsets the $\text{SFR}_{H\alpha}/\text{SFR}_{UV+\beta}$ ratio by $\sim 0.1 - 0.2$ dex for the mean source, depending on the slope of the SFH and the mean age of the galaxy distribution.
- *Ionizing spectrum*: The shape of the ionizing radiation field for low metallicity stellar populations is currently ill-constrained, which is unfortunate since this can have a significant influence on the nebular emission of high redshift galaxies (e.g. Kewley et al., 2013). Steidel et al. (2014) argue for a change in the effective temperature of the ionizing radiation from $T_e = 42000$ to $T_e = 55000$, from $z \sim 0$ to $z \sim 2$. Using this calibration we find that our $H\alpha$ -based SFRs can be overestimated by 0.17 dex, if one makes use of the local Kennicutt (1998) relation.
- *Dust law*: The largest uncertainty in our UV-based SFRs is the dust law. While one issue is the reddening law, another issue is a potential evolution in the intrinsic color of galaxies before reddening. In particular, galaxies with low metallicities and young ages can have bluer intrinsic UV slopes than those of the galaxies in the Meurer et al. (1999) calibration, which would result in an underestimate of the dust content in our galaxies. We explore a recent calibration by Castellano et al. (2014) and find that this can systematically change the $\text{SFR}_{H\alpha}/\text{SFR}_{UV+\beta}$ ratio by 0.23 dex.

We propose to bring the $H\alpha$ and UV-based SFRs into agreement by correcting the $H\alpha$ SFRs down by 0.17 dex and adopting the Castellano et al. (2014) dust calibration.

We construct the main sequence of star forming galaxies from our $H\alpha$ -based SFRs and find that, when taking into account the incompleteness limits of our sample, the slope is broadly consistent with the unity low-mass slope found by Whitaker et al. (2014) at $z \sim 0.5 - 2.5$. Furthermore, while we find an intrinsic scatter of $\sigma \sim 0.2 - 0.3$ and a normalization of the main sequence of $\log_{10} \text{sSFR}_{H\alpha}/\text{Gyr}^{-1} = 0.74 \pm 0.09$, which is higher by 0.2 - 0.4 dex than recent determinations from SED fitting (e.g. González et al., 2014; Duncan et al., 2014; Salmon et al., 2014).

We follow the Smit et al. (2012) procedure to infer SFR functions at $z \sim 4 - 7$ from the UV luminosity functions derived by Bouwens et al. (2014b), the UV-continuum slopes derived by Bouwens et al. (2014a) and the Castellano et al. (2014) dust calibration we adopted to match our UV and $H\alpha$ -based SFRs. We find that our derived $z \sim 4$ SFR function predicts similar SFR densities to those derived at $z \sim 2$ from $H\alpha$ and MIR measurements.

We conclude that a potential recalibration of local UV dust corrections, motivated by the high EW $H\alpha$ emission in combination with systematically high $\text{SFR}_{H\alpha}/\text{SFR}_{UV+\beta}$ ratios, can significantly alter our understanding of the star formation history of the Universe by shifting the peak of the global SFR density to earlier cosmic times. Confirmation of these findings can be obtained over the next few years with the advancement of the full ALMA array.

Table 5.1: Stepwise determinations of the SFR function at $z \sim 4$, $z \sim 5$, $z \sim 6$ and $z \sim 7$

$\log_{10} \text{SFR} (M_{\odot} \text{yr}^{-1})$	$\phi_{\text{SFR}} (\text{Mpc}^{-3} \text{dex}^{-1})$
$z \sim 4$	
-0.41 ± 0.05	0.05454 ± 0.01420
0.08 ± 0.05	0.04783 ± 0.00622
0.44 ± 0.06	0.02072 ± 0.00434
0.69 ± 0.06	0.01469 ± 0.00192
0.93 ± 0.06	0.01017 ± 0.00080
1.17 ± 0.06	0.00599 ± 0.00048
1.42 ± 0.06	0.00422 ± 0.00033
1.66 ± 0.06	0.00263 ± 0.00022
1.90 ± 0.06	0.00193 ± 0.00016
2.15 ± 0.06	0.00086 ± 0.00010
2.39 ± 0.06	0.00030 ± 0.00005
2.64 ± 0.06	0.00005 ± 0.00002
2.88 ± 0.06	0.00000 ± 0.00001
$z \sim 5$	
-0.29 ± 0.06	0.03305 ± 0.01242
0.21 ± 0.06	0.01483 ± 0.00448
0.71 ± 0.06	0.00805 ± 0.00108
1.09 ± 0.06	0.00479 ± 0.00042
1.34 ± 0.06	0.00237 ± 0.00023
1.59 ± 0.06	0.00205 ± 0.00015
1.84 ± 0.06	0.00082 ± 0.00009
2.09 ± 0.06	0.00053 ± 0.00006
2.35 ± 0.06	0.00018 ± 0.00003
2.60 ± 0.06	0.00005 ± 0.00001
2.85 ± 0.06	0.00001 ± 0.00001
3.10 ± 0.06	0.00000 ± 0.00000
$z \sim 6$	
-0.27 ± 0.09	0.01793 ± 0.00567
0.27 ± 0.10	0.01084 ± 0.00241
0.81 ± 0.10	0.00314 ± 0.00055
1.22 ± 0.10	0.00222 ± 0.00029
1.50 ± 0.10	0.00108 ± 0.00016
1.77 ± 0.10	0.00053 ± 0.00008
2.05 ± 0.10	0.00022 ± 0.00005
2.33 ± 0.10	0.00011 ± 0.00003
2.60 ± 0.10	0.00004 ± 0.00001
2.88 ± 0.10	0.00001 ± 0.00001
$z \sim 7$	
0.04 ± 0.15	0.01105 ± 0.00327
0.71 ± 0.16	0.00380 ± 0.00075
1.11 ± 0.16	0.00165 ± 0.00031
1.38 ± 0.16	0.00087 ± 0.00017
1.66 ± 0.16	0.00042 ± 0.00009
1.93 ± 0.16	0.00017 ± 0.00005
2.20 ± 0.16	0.00005 ± 0.00002
2.47 ± 0.16	0.00005 ± 0.00002

These SFR functions are obtained following the procedure described Smit et al. (2012). However, we dust correct the stepwise UV LFs by Bouwens et al. (2014b) using the Castellano et al. (2014) IRX- β relationship, as opposed to the Meurer et al. (1999) IRX- β relation (note that assuming a Meurer et al. (1999) calibration would systematically decrease the stepwise SFR determinations by 0.4 dex). We adopt the linear relation between the UV-continuum slope β and UV luminosity found by Bouwens et al. (2014a), see §5.6.

Table 5.2: Schechter parameters of the SFR functions

$\langle z \rangle$	$\log_{10} \frac{\text{SFR}^*}{M_{\odot} \text{yr}^{-1}}$	$\phi_{\text{SFR}}^* (10^{-3} \text{ Mpc}^{-3})$	α_{SFR}
3.8	2.09 ± 0.07	$1.16^{+0.19}_{-0.17}$	-1.53 ± 0.05
4.9	2.13 ± 0.08	$0.51^{+0.11}_{-0.10}$	-1.62 ± 0.07
5.9	2.13 ± 0.14	$0.24^{+0.11}_{-0.07}$	-1.66 ± 0.13
6.8	2.03 ± 0.20	$0.15^{+0.10}_{-0.07}$	-1.78 ± 0.19

These Schechter parameters are obtained following the procedure described Smit et al. (2012). However, we must correct the UV LFs by Bouwens et al. (2014b) using the Castellano et al. (2014) IRX- β relationship, as opposed to the Meurer et al. (1999) IRX- β relation (note that assuming a Meurer et al. (1999) calibration would systematically decrease the knee in the SFR function, SFR^* , by 0.4 dex). We adopt the linear relation between the UV-continuum slope β and UV luminosity found by Bouwens et al. (2014a), see §5.6.

Table 5.3: Parameters of the $\text{SFR}_{H\alpha} - M_*$ sequence

slope	1.06 ± 0.20
$\sigma_{\text{intrinsic}}$	$0.21^{+0.06}_{-0.04}$
$\text{SFR}_{H\alpha}(9.75 < \log_{10} M_*/M_{\odot} < 10.25)$	$1.72^{+0.10}_{-0.14}$
$\text{sSFR}_{H\alpha}(9.75 < \log_{10} M_*/M_{\odot} < 10.25)$	0.74 ± 0.09

Based on the Bayesian linear regression of all sources in our spectroscopic sample with $M_* > 10^{9.75} M_{\odot}$. Our $H\alpha$ -based SFR measurements are corrected down by 0.17 dex after conversion with the Kennicutt (1998) $\text{SFR}-L_{H\alpha}$ calibration, to account for a possibly changing shape of the ionizing radiation field.

References

- Anders, P., & Fritze-v. Alvensleben, U. 2003, *A&A*, 401, 1063
- Ashby, M. L. N., Willner, S. P., Fazio, G. G., et al. 2013, *ApJ*, 769, 80
- Balestra, I., Mainieri, V., Popesso, P., et al. 2010, *A&A*, 512, A12
- Bertin, E., & Arnouts, S. 1996, *A&AS*, 117, 393
- Bouwens, R. J., Illingworth, G. D., Franx, M., et al. 2009, *ApJ*, 705, 936
- Bouwens, R. J., Illingworth, G. D., Oesch, P. A., et al. 2012, *ApJ*, 754, 83
- Bouwens, R. J., Illingworth, G. D., Oesch, P. A., et al. 2014, *ApJ*, 793, 115
- Bouwens, R. J., Illingworth, G. D., Oesch, P. A., et al. 2014, *ApJ*, submitted, arXiv:1403.4295
- Brammer, G. B., van Dokkum, P. G., & Coppi, P. 2008, *ApJ*, 686, 1503
- Buat, V., Noll, S., Burgarella, D., et al. 2012, *A&A*, 545, A141
- Calzetti, D., Armus, L., Bohlin, R. C., et al. 2000, *ApJ*, 533, 682
- Castellano, M., Sommariva, V., Fontana, A., et al. 2014, *A&A*, 566, A19
- Coppin, K. E. K., Geach, J. E., Almaini, O., et al. 2014, submitted, arXiv:1407.6712
- Curtis-Lake, E., McLure, R. J., Dunlop, J. S., et al. 2013, *MNRAS*, 429, 302
- de Barros, S., Schaerer, D., & Stark, D. P. 2014, *A&A*, 563, A81
- de Mink, S. E., Cantiello, M., Langer, N., et al. 2009, *A&A*, 497, 243
- Domínguez, A., Siana, B., Brooks, A. M., et al. 2014, submitted, arXiv:1408.5788
- Duncan, K., Conselice, C. J., Mortlock, A., et al. 2014, *MNRAS*, 444, 2960
- Dunlop, J. S., McLure, R. J., Robertson, B. E., et al. 2012, *MNRAS*, 420, 901
- Dunlop, J. S., Rogers, A. B., McLure, R. J., et al. 2013, *MNRAS*, 432, 3520
- Eldridge, J. J., & Stanway, E. R. 2009, *MNRAS*, 400, 1019
- Eldridge, J. J., & Stanway, E. R. 2012, *MNRAS*, 419, 479
- Erb, D. K., Steidel, C. C., Shapley, A. E., et al. 2006, *ApJ*, 647, 128
- Eyles, L. P., Bunker, A. J., Stanway, E. R., et al. 2005, *MNRAS*, 364, 443
- Finkelstein, S. L., Papovich, C., Salmon, B., et al. 2012, *ApJ*, 756, 164
- Finkelstein, S. L., Papovich, C., Dickinson, M., et al. 2013, *Nature*, 502, 524
- Fontana, A., Dunlop, J. S., Paris, D., et al. 2014, *A&A*, 570, A11
- Fumagalli, M., Patel, S. G., Franx, M., et al. 2012, *ApJ*, 757, L22
- González, V., Labbé, I., Bouwens, R. J., et al. 2010, *ApJ*, 713, 115
- González, V., Bouwens, R. J., Labbé, I., et al. 2012, *ApJ*, 755, 148
- González, V., Bouwens, R., Illingworth, G., et al. 2014, *ApJ*, 781, 34
- Hathi, N. P., Mobasher, B., Capak, P., Wang, W.-H., & Ferguson, H. C. 2012, *ApJ*, 757, 43
- Kajisawa, M., Konishi, M., Suzuki, R., et al. 2006, *PASJ*, 58, 951
- Kennicutt, Jr., R. C. 1998, *ARA&A*, 36, 189
- Kewley, L. J., Dopita, M. A., Leitherer, C., et al. 2013, *ApJ*, 774, 100
- Kriek, M., van Dokkum, P. G., Labbé, I., et al. 2009, *ApJ*, 700, 221
- Labbé, I., Bouwens, R., Illingworth, G. D., & Franx, M. 2006, *ApJ*, 649, L67
- Labbé, I., González, V., Bouwens, R. J., et al. 2010a, *ApJ*, 716, L103
- Labbé, I., González, V., Bouwens, R. J., et al. 2010b, *ApJ*, 708, L26
- Labbé, I., Oesch, P. A., Bouwens, R. J., et al. 2013, *ApJ*, 777, L19
- Maiolino, R., Nagao, T., Grazian, A., et al. 2008, *A&A*, 488, 463
- Mannucci, F., Cresci, G., Maiolino, R., et al. 2009, *MNRAS*, 398, 1915
- Magnelli, B., Elbaz, D., Chary, R. R., et al. 2011, *A&A*, 528, A35
- Meurer, G. R., Heckman, T. M., & Calzetti, D. 1999, *ApJ*, 521, 64
- Oke, J. B., & Gunn, J. E. 1983, *ApJ*, 266, 713

- Oteo, I., Cepa, J., Bongiovanni, Á., et al. 2013, *A&A*, 554, L3
- Oteo, I. 2014, *A&A*, in press, arXiv:1409.2093
- Pannella, M., Elbaz, D., Daddi, E., et al. 2014, submitted, arXiv:1407.5072
- Papovich, C., Finkelstein, S. L., Ferguson, H. C., Lotz, J. M., & Giavalisco, M. 2011, *MNRAS*, 412, 1123
- Reddy, N. A., Steidel, C. C., Fadda, D., et al. 2006, *ApJ*, 644, 792
- Reddy, N. A., Steidel, C. C., Pettini, M., et al. 2008, *ApJS*, 175, 48
- Reddy, N. A., Erb, D. K., Pettini, M., Steidel, C. C., & Shapley, A. E. 2010, *ApJ*, 712, 1070
- Reddy, N., Dickinson, M., Elbaz, D., et al. 2012, *ApJ*, 744, 154
- Retzlaff, J., Rosati, P., Dickinson, M., et al. 2010, *A&A*, 511, A50
- Salpeter, E. E. 1955, *ApJ*, 121, 161
- Shim, H., Chary, R.-R., Dickinson, M., et al. 2011, *ApJ*, 738, 69
- Shirazi, M., Brinchmann, J., & Rahmati, A. 2014, *ApJ*, 787, 120
- Schaerer, D., & de Barros, S. 2009, *A&A*, 502, 423
- Schaerer, D., de Barros, S., & Sklias, P. 2013, *A&A*, 549, A4
- Schenker, M. A., Ellis, R. S., Konidakis, N. P., & Stark, D. P. 2013b, *ApJ*, 777, 67
- Skelton, R. E., Whitaker, K. E., Momcheva, I. G., et al. 2014, *ApJS*, 214, 24
- Sobral, D., Best, P. N., Smail, I., et al. 2014, *MNRAS*, 437, 3516
- Speagle, J. S., Steinhart, C. L., Capak, P. L., & Silverman, J. D. 2014, *ApJS*, 214, 15
- Spitler, L. R., Labbé, I., Glazebrook, K., et al. 2012, *ApJ*, 748, L21
- Salmon, B., Papovich, C., Finkelstein, S. L., et al. 2014, submitted, arXiv:1407.6012
- Smit, R., Bouwens, R. J., Franx, M., et al. 2012, *ApJ*, 756, 14
- Smit, R., Bouwens, R. J., Labbé, I., et al. 2014, *ApJ*, 784, 58
- Stanway, E. R., Eldridge, J. J., Greis, S. M. L., et al. 2014, *MNRAS*, 444, 3466
- Stark, D. P., Ellis, R. S., Bunker, A., et al. 2009, *ApJ*, 697, 1493
- Stark, D. P., Ellis, R. S., Chiu, K., Ouchi, M., & Bunker, A. 2010, *MNRAS*, 408, 1628
- Stark, D. P., Ellis, R. S., & Ouchi, M. 2011, *ApJ*, 728, L2
- Stark, D. P., Schenker, M. A., Ellis, R., et al. 2013, *ApJ*, 763, 129
- Steidel, C. C., Rudie, G. C., Strom, A. L., et al. 2014, *ApJ*, accepted, arXiv:1405.5473
- Troncoso, P., Maiolino, R., Sommariva, V., et al. 2014, *A&A*, 563, A58
- van der Wel, A., Bell, E. F., Häussler, B., et al. 2012, *ApJS*, 203, 24
- van der Wel, A., Franx, M., van Dokkum, P. G., et al. 2014, *ApJ*, 788, 28
- Vanzella, E., Cristiani, S., Dickinson, M., et al. 2005, *A&A*, 434, 53
- Vanzella, E., Cristiani, S., Dickinson, M., et al. 2006, *A&A*, 454, 423
- Vanzella, E., Cristiani, S., Dickinson, M., et al. 2008, *A&A*, 478, 83
- Vanzella, E., Giavalisco, M., Dickinson, M., et al. 2009, *ApJ*, 695, 1163
- Verma, A., Lehnert, M. D., Förster Schreiber, N. M., Bremer, M. N., & Douglas, L. 2007, *MNRAS*, 377, 1024
- Whitaker, K. E., Franx, M., Leja, J., et al. 2014, submitted, arXiv:1407.1843
- Wilkins, S. M., Bunker, A. J., Stanway, E., Lorenzoni, S., & Caruana, J. 2011, *MNRAS*, 417, 717
- Wilkins, S. M., Gonzalez-Perez, V., Lacey, C. G., & Baugh, C. M. 2012, *MNRAS*, 424, 1522
- Wilkins, S. M., Bunker, A., Coulton, W., et al. 2013, *MNRAS*, 430, 2885
- Wiklund, T., Dickinson, M., Ferguson, H. C., et al. 2008, *ApJ*, 676, 781
- Yabe, K., Ohta, K., Iwata, I., et al. 2009, *ApJ*, 693, 507

Nederlandse samenvatting

Het vraagstuk van onze oorsprong fascineert mensen van jong tot oud. Binnen dit vraagstuk specialiseert de extragalactische sterrenkunde zich op het ontstaan van sterrenstelsels en daarmee op de oorsprong van onze Melkweg. Door het installeren van de nieuwste camera op de *Hubble Space Telescope*, tijdens één van de laatste missies van de *Space Shuttle* in 2009, is een hele nieuwe generatie sterrenstelsels gevonden, die we nu kunnen waarnemen slechts een paar honderd miljoen jaar na de oerknal, het kosmische ochtendgloren van de geschiedenis van ons heelal. Dit proefschrift presenteert innovatieve observatieve studies naar de eigenschappen van deze vroege sterrenstelsels, om daarmee inzicht te verkrijgen in de fysische processen achter het ontstaan van de allereerste sterren en sterrenstelsels.

Kosmologie en het vroege universum

Het grondwerk voor het bouwen van sterrenstelsels wordt gelegd bij het allereerste moment van onze kosmische geschiedenis: de oerknal. Bij het exploderen van de oerknal, 13.8 miljard jaar geleden, ligt de huidige verdeling van de verschillende materialen in het heelal meteen vast: 69% is donkere energie, een eigenschap van het heelal die we kunnen meten maar geenszins kunnen verklaren, 27% is donkere materie, deeltjes die waarschijnlijk vergelijkbare eigenschappen hebben als het neutrino maar met een veel grotere massa, en tenslotte is slechts 4% baryonische materie, een verzamelnaam voor alle deeltjes die we kennen en begrijpen zoals bijvoorbeeld waterstof, helium, koolstof en zuurstof, oftewel de bouwstenen van onze planeet.

Gedurende de eerste 400 duizend jaar na de oerknal dijt het universum uit en koelt het af, van bijna oneindig hoge temperaturen tot aan een paar duizend graden Kelvin. Op dat moment kan neutraal waterstof zich vormen en kan tegelijkertijd het allereerste licht uitgezonden worden, wat we vandaag de dag nog steeds kunnen zien in de vorm van de kosmische achtergrondstraling. De achtergrondstraling is een bijna perfect uniforme warmtebron, met slechts hele kleine variaties in de temperatuur op verschillende plekken aan de hemel. Die kleine variaties geven bewijs van de onregelmatigheden in de dichtheidsverdeling van de donkere en baryonische materie in dit vroege stadium van het universum. De periode tussen 400 duizend jaar en 400 miljoen jaar na de oerknal wordt ook wel de *donkere eeuwen* genoemd. In deze periode is er nog (bijna) geen sterrenlicht te zien, maar de gebieden met de hoogste dichtheid trekken steeds meer materie naar zich toe onder de invloed van de zwaartekracht om zo de nestjes te vormen waar de eerste sterren en sterrenstelsels geboren worden.

Uit de polarisatiemetingen van de kosmische achtergrondstraling kunnen we bepalen dat ongeveer 400 miljoen jaar na de oerknal de eerste sterrenstelsels genoeg hoogerenergetische straling produceren om het neutrale waterstofgas dat overal in het universum aanwezig is te ioniseren. Uit de spectra van enkele hele vroege *Quasars* (fel brandende accretieschijven rond supermassieve zwarte gaten) kunnen we opmaken dat dit reïonisatieproces pas voltooid is ongeveer 1 miljard jaar na de oerknal. Deze meetgegevens geven inzicht in de totale hoeveelheid straling die er door de eerste sterren en sterrenstelsels geproduceerd moet worden om het geïoniseerde gas in ons heelal te verklaren.

Het uitkarteren van de kosmische dichtheid van sterformatie als een functie van de tijd heeft

laten zien dat het hoogtepunt van activiteit in ons heelal ongeveer 8 tot 10 miljard geleden plaatsvond, slechts een paar miljard jaar na de oerknal. Als we sterrenstelsels in dat tijdperk bekijken vinden we grote roterende en stervormende schijven, gigantisch zware, dode sterrenstelsels en door stof verduisterde stelsels die een extreme uitbarsting van sterformatie ondergaan. De ontdekkingen van deze ver ontwikkelde stelsels leidden tot de verrassende conclusie dat de eerste generaties van sterrenstelsels een razend snelle ontwikkeling moeten doormaken in de 2 miljard jaar na de reïonisatieperiode.

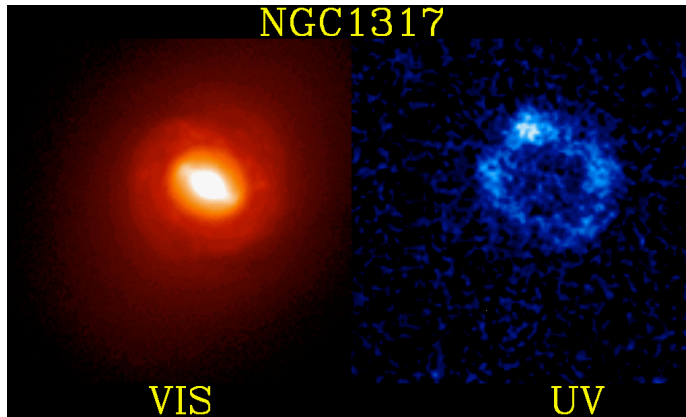
De bovenstaande kennis die in de afgelopen twee decennia is verzameld motiveert de observationele studie van sterrenstelsels in de eerste paar miljard jaar na de oerknal. Ondanks de aanzienlijke technische beperkingen en uitdagingen, proberen we het licht te zien van sterrenstelsels vele miljarden lichtjaren ver weg om een antwoord te krijgen op vragen zoals: Hoe zijn de allereerste sterren ontstaan? Hoe kunnen de eerste generatie sterrenstelsels genoeg straling produceren om al het neutrale waterstof gas in het universum te reïoniseren? Hoe ontwikkelen de eerste generaties van sterrenstelsels zich om uiteindelijk de diverse en geavanceerde sterrenstelsel populatie te vormen die we zien tijdens de piekperiode in de historie van onze kosmos?

Terugkijken in de tijd

Om de geschiedenis van het universum in beeld te brengen, maken we gebruik van het feit dat licht een hele grote maar toch eindige snelheid heeft. Als een gevolg hiervan zien we de objecten aan de hemel altijd in het verleden. Het licht van de zon heeft 8 minuten nodig om de aarde te bereiken en zodoende kijken we 8 minuten terug in de tijd als we naar de zon kijken. De meeste sterren aan de hemel zien we een aantal duizenden jaren terug in het verleden, simpelweg omdat het licht er een paar duizend jaar over doet om de afstand van een ster tot onze aarde af te leggen. Als we buiten onze eigen Melkweg naar andere sterrenstelsels kijken gaan we al snel miljoenen jaren terug in de geschiedenis van deze objecten. In theorie kunnen we diep genoeg het heelal in kijken om 13,8 miljard jaar geleden het begin van van onze tijdlijn te zien. In de praktijk zijn sterrenstelsels die miljarden lichtjaren van ons weg staan echter extreem lichtzwak en kunnen we alleen door vele telescoopnames met hele lange sluitertijden bij elkaar op te tellen het licht van deze objecten onderscheiden van de instrumentruis.

Het waarnemen van verre, lichtzwakke sterrenstelsels vormt een extreme uitdaging voor het ontwerpen en bouwen van onze telescopen, maar daarnaast moet ook nog eens rekening gehouden worden met het uitdijen van het universum. Door het uitdijende heelal bewegen alle sterrenstelsels van ons af en rekt hun licht uit naar langere (rodere) golflengtes. Dit fenomeen noemen we roodverschuiving en is te vergelijken met het welbekende dopplereffect dat verklaart waarom een voorbijrijdende raceauto een hogere frequentie heeft wanneer het naar ons toe komt en een lagere frequentie wanneer het van ons weg rijdt. Hoe verder een sterrenstelsel van ons af staat, hoe sneller het sterrenstelsel van ons weg gaat en hoe roder het licht dat wij bij onze detectoren waarnemen. Door de hoge mate van roodverschuiving van sterrenstelsels die miljarden lichtjaren ver weg staan is het belangrijk om telescopen te gebruiken die niet alleen heel lichtgevoelig zijn voor het visuele licht dat wij met onze ogen zien, maar ook voor het nabije- en middel-infrarode spectrum.

In dit proefschrift maken we gebruik van data van de *Hubble Space Telescope* en de *Spitzer Space Telescope* om eigenschappen van sterrenstelsels in het vroege universum te meten. De installatie van de Wide Field Camera 3 (WFC3) op *Hubble* in 2009 heeft ervoor gezorgd dat we lichtgevoe-



Figuur 5.10: Het nabije sterrenstelsel NGC1317, ook wel Fornax A genoemd, afgebeeld in twee onderdelen van het elektromagnetische spectrum: visueel (links) genomen door *Cerro Tololo Interamerican Observatory* en ultraviolet (rechts) door de *Ultraviolet Imager Telescope*. Langlevende sterren zoals de zon zien we links, ze laten de structuur en de totale massa van het sterrenstelsel zien. Kortlevende sterren zien we rechts, ze laten zien welke delen van het sterrenstelsel nog steeds nieuwe sterren vormen. *Credit: UIT, NASA*

lige en hoge resolutie opnames hebben in het nabije-infrarood. Door de hoge roodverschuiving zien we zelfs met deze camera alleen de sterren die veel ultraviolette (UV) straling uitzenden in sterrenstelsels meer dan 10 miljard lichtjaar ver weg. Sterren met veel UV straling hebben een zeer korte levensduur naar astronomische maatstaven: het duurt slechts 100 miljoen jaar voordat ze exploderen en vervolgens uitdoven. Dit betekent dat UV licht informatie geeft over het aantal kortlevende sterren dat in de laatste 100 miljoen jaar in een sterrenstelsel geboren werden. In de Melkweg zien we dat kortlevende en langlevende sterren altijd met een vaste verhouding geboren worden. Met dit gegeven en met de aanname dat de mate van stervorming in sterrenstelsels geen grote schommelingen ondervindt in de 100 miljoen jaar voorafgaand aan de waarneming, berekenen we met onze *Hubble* metingen van vroege sterrenstelsels het totale aantal sterren dat in deze stelsels per jaar geboren worden.

Om een beeld te vormen van de totale hoeveelheid sterren die een sterrenstelsel omvat is het nodig om naar sterren te kijken met een langere levensduur. Dit zijn bijvoorbeeld sterren zoals de zon, die veel straling uitzenden in het visuele spectrum. Figuur 5.10 geeft een illustratie van een nabij sterrenstelsel NGC1317, waarbij de twee opnames het visuele licht (links) en het uitgezonden UV licht (rechts) laten zien. De visuele opname toont een duidelijke schijf van sterren met de bulk van het sterrenlicht afkomstig uit een platte kern. Het UV licht benadrukt geheel andere gebieden in het sterrenstelsel: daar waar stervorming nog hevig gaande is. Terwijl *Hubble* het UV licht van sterrenstelsels op hoge roodverschuiving nog net kan zien met een nabij-infrarood camera, is het visuele licht verschoven naar het middel-infrarode spectrum, wat alleen maar zichtbaar is met *Spitzer*.

Metingen aan sterrenstelsels in het vroege heelal

Om de fysische processen achter het ontstaan en ontwikkelen van sterrenstelsels bloot te leggen worden zo groot mogelijke steekproeven van sterrenstelsels verzameld. Deze steekproeven kunnen bijvoorbeeld gevonden worden in blanke velden: stukken van de hemel met zo weinig mogelijk Melkweg sterren die uitermate geschikt zijn voor lange sluitertijden. Een alternatieve steekproef kan plaatsvinden in het gezichtsveld van een massief cluster van sterrenstelsels, de meest massieve structuren in ons universum. Door de grote massa van deze clusters buigen inkomende lichtstralen om de structuur heen en daarmee ontstaat een lenseffect, ookwel een zwaartekracht lens genoemd. Het licht van verre sterrenstelsels achter de clusters zien we als onder een vergrootglas: helderder en enigszins uitgerekt. Dit heeft als voordeel dat we een hogere signaal/ruis verhouding krijgen bij metingen van de lichtzwakke achtergrondstelsels, maar ook het nadeel dat de mate van vergroting en daarmee de meting van de intrinsieke lichtintensiteit van het sterrenstelsel erg onzeker is. Hoewel recente metingen vooral gebaseerd zijn op blanke steekproeven, zijn lensstudies in opkomst. Zo deelde *Hubble* in 2013 bijvoorbeeld 840 uur waarnemings tijd toe aan het prestigieuze Frontier Fields programma, dat in de komende jaren extreem diep het heelal in zal kijken in 6 clustervelden.

Eén van de belangrijkste metingen die we met *Hubble* kunnen uitvoeren is de zogeheten UV-lichtkrachtfunctie: een meting van de dichtheid van sterrenstelsels als functie van hun UV lichtintensiteit. Recente studies laten zien dat we na de oerknal voornamelijk voor de helderste stelsels de dichtheid zeer snel zien toenemen. De fysische interpretatie die we hieraan kunnen toebedelen is dat terwijl het heelal ouder wordt opeenvolgende generaties sterrenstelsels steeds grotere bronnen van stervorming worden. Een belangrijke onzekerheid in het kwantificeren van deze meting is de hoeveelheid kosmisch stof in sterrenstelsels. Interstellaire stofwolken bestaan uit vaste deeltjes ter grootte van een paar micrometer die een gedeelte van de straling van sterren absorbeert, vergelijkbaar met een wolk dichte sigarettenuitademing die donker afsteekt tegen een lichtbron. Kosmisch stof heeft de typerende eigenschap dat het meer licht absorbeert op korte dan op langere golflengtes. Een simpele manier om te corrigeren voor de geabsorbeerde straling door stof is dan ook aan de hand van de kleur van een sterrenstelsel. Kleuren worden gemeten door de lichtkracht van sterrenstelsels te bepalen in twee opnames waarbij het spectrum gefilterd is op het licht van aangrenzende golflengtegebieden. Een rode kleur correspondeert met een deficiëntie in lichtintensiteit van de korte golflengtes, een indicatie voor kosmisch stof.

Als we niet alleen de opnames van *Hubble* maar ook de data van *Spitzer* gebruiken kunnen we naast de mate van stervorming bijvoorbeeld ook de sterrenmassa van een sterrenstelsel meten. Daarnaast geeft de verhouding tussen stervorming en sterrenmassa een mate van efficiëntie van de sterformatie. In de huidige fysische modellen over de vorming van sterrenstelsels, correleert de stervormingsefficiëntie sterk met de mate van toevoer van vers gas uit de intergalactische ruimte. Doordat ons universum uitdijt wordt deze toevoer vrijgesteld door de lagere dichtheid van gas in het heelal en we verwachten dus een hoge mate van stervormingsefficiëntie in het vroege heelal en een gestage afname met de tijd. Gedurende de afgelopen 10 jaar hebben meerdere onafhankelijke studies met *Spitzer* metingen verricht aan sterrenstelsels in de eerste paar miljard jaar na de oerknal. Verassend genoeg vonden de meeste studies constante lage stervormingsefficiënties, zelfs bij de vroegste generaties sterrenstelsels. Deze discrepantie tussen modellen en waarnemingen geeft ofwel een gebrek in onze theoretische kennis, ofwel een systematische afwijking in de metingen aan.

De interpretatie van het licht dat we waarnemen met *Spitzer* wordt bemoeilijkt door de emis-

sielijnen die worden geproduceerd in de gasnevels van stervormingsgebieden. Deze emissielijnen worden opgevangen in de *Spitzer* opnames en kunnen de oorzaak zijn van een te hoge meting van de totale lichtintensiteit van hoge roodverschuiving sterrenstelsels, wat tot gevolg heeft dat we een te zware massa en te lage stervormingsefficiëntie meten. In 2018 zal de *James Webb Space Telescope* gelanceerd worden, waarmee we deze emissielijnen direct kunnen meten met mid-infrarood spectroscopie. Tot die tijd echter moeten we ons beperken tot de fotometrie van *Spitzer*.

Dit proefschrift

Dit proefschrift presenteert studies naar de eigenschappen van sterrenstelsels die we waarnemen tussen 800 miljoen en 1.5 miljard jaar na de oerknal. Hoofdstuk 2 en 5 onderzoeken eigenschappen van sterformatie in deze stelsels, terwijl hoofdstuk 3 en 4 zich richten op de invloed van emissielijnen bij het meten van sterrenmassa en efficiëntie van de sterformatie.

Hoofdstuk 2 geeft de eerste bepaling van de stervormingsfunctie in de eerste paar miljard jaar na de oerknal. Met behulp van een steekproef van 2500 sterrenstelsel met gedetailleerde kleurmetingen, corrigeren we de UV-lichtkrachtfunctie van vier generaties sterrenstelsels tussen 800 miljoen en 1.5 miljard jaar na de oerknal voor de effecten van stofabsorptie om zodoende de mate van stervorming te quantificeren. De stervormingsfunctie geeft een gedetailleerde meting van de dichtheid van sterrenstelsels als een functie van hun mate van stervorming en hiermee fungeert het als een belangrijke test voor modellen en simulaties van het vroege universum.

Hoofdstuk 3 introduceert de eerste metingen over de invloed van emissielijnen uit gasnevels op de gemeten *Spitzer* lichtintensiteit van sterrenstelsels slechts 800 miljoen jaar na de oerknal. We maken gebruik van sterrenstelsels gevonden in de CLASH survey, een dataset speciaal gericht op cluster velden, waardoor we gebruik kunnen maken van de vergroting door de zwaartekrachten om voldoende signaal/ruis verhouding te krijgen in de *Spitzer* opnames. We selecteren sterrenstelsels in een specifieke tijdszone waar we weten dat de *Spitzer* meting op 4.5 micrometer geen invloed ondervindt van emissielijnen en we vergelijken dit met een meting op 3.6 micrometer waar deze lijnen wél een rol spelen. We concluderen dat emissielijnen gemiddeld genomen een zeer belangrijke invloed hebben op de gemeten *Spitzer* lichtintensiteit ten opzichte van sterrenlicht. In sommige individuele gevallen wordt de gemeten *Spitzer* lichtintensiteit zelfs compleet gedomineerd door gasnevellijnen. Als gevolg hiervan zijn onze nieuwe metingen van de sterrenmassa veel lager dan voorheen en is de gemiddelde stervormingsefficiëntie in goede overeenkomst met theoretische voorspellingen.

Hoofdstuk 4 beschrijft een nieuwe techniek om met hoge precisie afstandsbevestigingen te verrichten van sterrenstelsels 800 miljoen jaar na de oerknal. Door gebruik te maken van de resultaten in hoofdstuk 3 waar we sterrenstelsels vonden met dominante gasnevellijnen, kunnen we nieuwe sterrenstelsels vinden met deze specifieke eigenschappen. We gebruiken de kleur van sterrenstelsels afgeleid van metingen op 3.6 en 4.5 micrometer. Dominante emissielijnen produceren alleen extreem rode of extreem blauwe kleuren bij een bepaalde roodverschuiving, doordat de afstanden in golflengte tussen de verschillende lijnen en het golflengtegebied waar *Spitzer* gevoelig is een specifieke verhouding tot elkaar hebben. Dit kunnen we dan weer gebruiken om de afstandsbevestiging aanzienlijk te verbeteren. Deze nieuwe afstandsbevestigingen zijn zeer belangrijk om vervolgstudies te kunnen ondernemen met de nieuwe *Atacama Large Millimetre Array* telescoop, waarmee we beter inzicht kunnen krijgen in bijvoorbeeld de gasinhoud van vroege sterrenstelsels.

Hoofdstuk 5 onderzoekt twee indicatoren voor de mate van stervorming in sterrenstelsels ongeveer 1 tot 2 miljard jaar na de oerknal. Tijdens deze periode kunnen we aan de hand van de invloed van gasnevellijnen op de *Spitzer* metingen een schatting maken van de totale mate van stervorming in sterrenstelsels op tijdschalen van ongeveer 10 miljoen jaar. Door deze schattingen uit te zetten tegen de voor stof gecorrigeerde UV lichtkracht metingen, die gevoelig zijn voor de sterren die gevormd zijn over een tijdschaal van 100 miljoen jaar, kunnen we inzicht krijgen in de recente historie van sterformatie. We vinden een uitstekende overeenkomst tussen de twee onafhankelijke bepalingen van de mate van stervorming met een kleine spreiding in de individuele metingen. We concluderen dat er weinig stochastische variatie is in de mate van stervorming op tijdschalen van tientallen miljoenen jaren. Deze metingen zijn van belang voor ons fysisch inzicht in het evenwicht tussen verse toevoer van gas uit de intergalactische ruimte en eventuele tegenwerkende krachten zoals exploderende supernovae.

Curriculum Vitae

I was born on May 11, 1985 in Los Angeles, California (USA), but within a year of my birth my family moved to back Amsterdam (NL), where I spent my entire childhood. I attended the Buikslotermeerschool and the Barlaeus Gymnasium for primary school and high school, respectively. Without doubt, my favorite classes in high school were Physics and Art, which motivated me to pursue a degree in Architecture at Delft University of Technology in 2003. In 9 months time I reached the conclusion that my talents were wasted in Architecture and I missed the challenges that only my classes in Physics used to bring. I finally arrived in Leiden to embark upon a degree in Astronomy in 2004.

During the second year of my Astronomy bachelor course I was lucky enough to join an observing run on the Isaac Newton Telescope on La Palma, my first experience with real Astronomy. Despite my joy in the classes and coursework, I did not envision myself in the role of scientist. Preparing myself for a career in industry, with a particular interest in strategy consultancy, I took leave for a year to sit on the board of the student society *De Leidse Flesch*. Despite the many opportunities that year to talk to industry representatives about their core business and talent recruitment, I started to reconsider my ambition of working for a company with the single aim of profit. I found my love for science during my bachelor thesis, working under the supervision of Dr. Clovis Hopman on the disruption of binary stars by supermassive black holes.

During my Master in Astronomy at the Sterrewacht in Leiden, I had the opportunity to work with Prof. Paul van der Werf on the modeling of the black hole accretion disk in Centaurus A and with Dr. Henk Hoekstra on mass modeling of galaxy clusters. A highlight of my academic education was a 6 month studentship at the University of California, Berkeley, in the fall of 2009. In parallel with my participating in classes on star formation and particle physics I worked full time with astrophysicists Dr. Joanne Cohn and Prof. Martin White on mock observations of galaxy clusters using cosmological dark matter simulations.

After my Masters studies I was given the opportunity to enter the Leiden PhD program under the supervision of Dr. Rychard Bouwens, with Prof. Marijn Franx as my official promotor. My thesis work focused on observations of galaxies in the early Universe. I analyzed observations of the *Hubble Space Telescope* and the *Spitzer Space Telescope* and I observed with the Japanese *Subaru Telescope* on Mauna Kea, Hawaii (USA). I presented my work at conferences and meetings in Aix-en-Provence (France), Baltimore (USA), Bilbao (Spain), Cambridge (UK), Durham (UK), London (UK), Obergurgl (Austra) and Portsmouth (UK) and I attended the 2013 Jerusalem Winter School. I supervised master students Nicholas Rasappu and Mieke Paalvast in their Master thesis research projects. I have given public lectures to audiences from age 8 to 80 and organized the Dutch National Astronomy Olympiad in 2012.

In the next three years I will continue my career in Astronomy as a postdoctoral researcher at the Centre for Extragalactic Astronomy of Durham University (UK), working on integral field spectroscopy of distant galaxies with the European *Very Large Telescope*.

Nawoord

In the last four years I have grown as a person, astronomer and scientist. As I am writing this thesis I am more than ever aware that I could not have gotten here without the support of many people.

First of all, I want to thank the amazing organizational support structure of Leiden Observatory. The secretaries, computer group, educational, financial and scientific directors and all those people that contribute every day to make the Sterrewacht a smoothly-operated institute.

Though I was never truly part of a research group the presence of Marijn, Ivo, Adam, Shannon, Mattia, Jesse, Daniel, Caroline, Allison and Benne created an important intellectual and scientific environment for me in Leiden. From journal club to science discussion over coffee and lunch, to help and advise on thesis writing, proposal writing and the job market, it would not have been possible without your input. It is important to note that the science in this thesis could not have been possible without the software developed by Ivo Labbé and I am very grateful for his in-depth knowledge and technical expertise of the data that he was always willing to share.

I am grateful to have interacted with experienced and talented international collaborators Pascal Oesch, Garth Illingworth, Pieter van Dokkum and Valentino Gonzalez for their input on the writing of my thesis chapters.

I want to thank all members of CLASH and in particular Marc Postman and Dan Coe for their leadership of a collaboration that gave me the opportunity to interact with so many intelligent researchers from all over the world, each with a different science background and research goal.

I want to thank my former office mates Wendy, Koen and Ernst for the company over the years. Most importantly I want to thank the unofficial fourth officemate, who actually occupied the office next door: thank you so much for all the learning experiences, craziness, inspiration, energy, guidance and laughter. Could I have gone back I would not have opted for a different mentor in the world.

The years as a PhD student were for me and many before me a time of ups and downs. It was in many ways a time when I grew up - in a way that didn't quite happen as an undergraduate. I am grateful for so many people that I met during my PhD and for all the people that have had an impact on my life in a major or minor way. I do believe that all the adventures and beautiful memories helped me through the times of doubt and insecurity.

From the last four years I will always remember: a legendary beer bike trip with Shannon, Adam, Suzanne, Remco, Jayne, Edith, Rychard, Daniel, Jesse, Mattia, Rob - a weekend in Riga with Erica and Therese - Observing at Subaru with Larry Bradley - A visit in WWII history with Shannon, Adam, Suzanne, Rob - Copenhagen with Therese and Rachel - all the coffee breaks to complain about work or the lack of ice on the canals with Jesse - An icy road trip past the ancient temples and the deserts of Jordan with Mattia, Monica, Joel - Beautiful and sunny Provence with Mattia, Shannon, Rob - a Jerusalem winter school with Sarah - and the discussions on politics and feminism with Berenice.

Het eind van mijn PhD betekent ook (eindelijk?) een eind aan 10 jaar in Leiden. Ik kijk terug op mijn studententijd in Leiden en denk aan de beste huisgenootjes in de wereld: de hippe Oscar, de sterke Jelle en de leuke Pieter, maar ook bestuurs- en commissiegenootjes zoals Wendy, Marcel,

Eric en Kirsten. Oscar, ik hoop dat het altijd lukt om tijd te maken in onze drukke schema's om bij te praten en te roddelen - wie had ooit gedacht dat wij degenen zouden zijn die een PhD zouden ondernemen?!

Ik ben heel blij met de trouwe jaarclub die ik overhoud uit mijn tijd in Delft; Anne, Arjanna, Francien, Marjoleine, Matthias, Nadia, Rico en Wouter - onofficieel aangevuld door Koen en Maaïke. Arjanna, heel veel dank voor de af en toe zo essentiële zorgverlening die je zo makkelijk op je neemt, de huiskamerlezingen die inspiratie gaven en het organiseren van weekenden buitenkunst die me weghaalden uit mijn academische denkwereld. Francien, wat goed dat je me uiteindelijk toch achter mijn bureau naar het zwembad en de ijsbaan kreeg, na al die jaren zonder enige lichaamsbeweging. Ik houd het zwemmen nog steeds vol en hopelijk kan ik op een dag met je mee naar de Weissensee. Anne (mijn trotse paranimf!), ik denk met zo veel plezier terug aan onze gesprekken op vrijdagavond in Rotterdam wanneer we weer opnieuw een werkweek hadden overleefd en je me emotionele support gaf over de belangrijke zaken in het leven.

Marius, veel dank voor het persoonlijk (ver)bouwen van het huis dat ik jarenlang mijn thuis beschouwde in Rotterdam. Ik heb veel goede herinneringen aan die plek.

Sinds de kleuterschool, basisschool en middelbare school zijn Renee, Belle, Katharina en Suzan altijd mijn vudevriendinnetjes gebleven. Soms zie ik jullie met enige regelmaat, soms lange tijd niet, maar dan kom je elkaar toch weer tegen en dan is het zo fijn dat het net is alsof er geen dag voorbij is gegaan sinds we dagelijks samen naar school gingen.

Lieve mama en papa (of Dr. Bos en Prof. Dr. Smit), ik denk dat ik met zekerheid kan zeggen dat ik nooit wetenschapper in de sterrenkunde was geworden als ik niet een vader had gehad die me de liefde voor de wetenschap met de paplepel ingaf en een moeder die me altijd vertelde 's ik terug zou kunnen gaan zou ik misschien tóch natuurkunde hebben gestudeerd. Jullie zijn altijd een inspirerend en enigszins intimiderend voorbeeld geweest. En toch zijn jullie er dan altijd, zo rotsvast and onveranderd, wanneer het dak boven mijn hoofd er even niet meer is.

Lieve Frouwk, wat ontzettend leuk dat je toch naast me kan staan als paranimf als ik straks mijn proefschrift verdedig! Er is niemand die me zo goed kent. Ik vind het zo fijn dat je altijd weet wat ik denk voordat ik het je echt hoeft te vertellen.

My Rob, I don't think I will ever be able to explain how grateful I am that you picked me up, at a moment when I simply wasn't very happy with my life. Your warmth has made all the difference.

